

MEASUREMENTS OF CHARGED HADRON INCLUSIVE REACTIONS
IN THE PROJECTILE FRAGMENTATION REGION AT 100 AND 175 GEV

by

WILLIAM W. TOY

S.B., Massachusetts Institute of Technology

(1973)

S.M., Massachusetts Institute of Technology

(1973)

E.E., Massachusetts Institute of Technology

(1973)

SUBMITTED IN PARTIAL FULFILLMENT
OF THE REQUIREMENTS FOR THE
DEGREE OF

DOCTOR OF PHILOSOPHY

at the

MASSACHUSETTS INSTITUTE OF TECHNOLOGY

MAY, 1978

Signature of Author..... *William W. Toy*
Department of Physics, May 5, 1978.

Certified by..... *Jerome I. Friedman*
Thesis Supervisor.

Accepted by.....
Chairman, Departmental Committee on Graduate Students.

MEASUREMENTS OF CHARGED HADRON INCLUSIVE REACTIONS
IN THE PROJECTILE FRAGMENTATION REGION AT 100 AND 175 GEV

by

WILLIAM W. TOY

Submitted to the Department of Physics on May 5, 1978 in partial fulfillment of the requirements for the degree of Doctor of Philosophy.

ABSTRACT

Differential cross sections for the inclusive processes $a + p \rightarrow c + X$, where a and c can be any of π^+ , K^+ , p or \bar{p} , were measured at 100 and 175 GeV using the Single Arm Spectrometer Facility of the Fermi National Accelerator Laboratory. The measurements covered a range in x from 0.12 to 1.0 and in p_{\perp} from 0.1 to 1.25 GeV/c. Emphasis was placed in the analysis on the beam fragmentation region. Several models of the fragmentation process were tested and were shown to be in good agreement with the data. These models suggest that the quark-parton picture may play a central role in describing these low p_{\perp} processes.

Thesis Supervisor: Jerome I. Friedman
Title: Professor of Physics

FERMILAB LIBRARY

3

3

3

3

TABLE OF CONTENTS

	<u>Page</u>
ABSTRACT	2
TABLE OF CONTENTS	3
LIST OF FIGURES	5
LIST OF TABLES	7
I. INTRODUCTION	8
A. Background	8
B. Experimental Overview	12
C. Physics Motivation	15
II. EXPERIMENTAL DETAILS	17
A. Accelerator	17
B. M6E Beam Line	19
C. Single Arm Spectrometer	24
D. AVB System	27
E. Target	28
F. Scintillation Counters and Rodoscopes	30
G. Multiwire Proportional Chambers	37
H. Gas Cerenkov Counters and Particle Identification	41
I. TRANSPORT and Decode	45
J. Fast Electronics	48
K. Online Computer System	52
L. Data Taking	55
III. DATA ANALYSIS	58
A. Overview	58
B. PASS1	61

	<u>Page</u>
C. PASS2	65
D. Run Combination	68
E. Corrections and Errors	70
IV. RESULTS AND INTERPRETATION	88
A. Final Cross Sections	88
1. P_T Dependence	89
2. x Dependence	89
3. x Dependence of Cross Sections Integrated over P_T	118
B. Scaling	127
C. Quark Decay Model of Andersson, Gustafson and Peterson	146
D. Quark Recombination Model of Das and Hwa	161
E. Fragmentation Model of Brodsky and Gunion	177
V. DISCUSSION	200
APPENDIX I: Invariant Differential Cross Sections- P_T Dependence	203
APPENDIX II: Invariant Differential Cross Sections- x Dependence	217
APPENDIX III: Radiative Correction Formulae	240
APPENDIX IV: Spectrometer First Order TRANSPORT Coefficients	244
REFERENCES	248
ACKNOWLEDGEMENTS	251
BIOGRAPHICAL NOTE	253

LIST OF FIGURES

<u>Figure Number</u>	<u>Page</u>
1. Beam Fragmentation	10
2. Overview of Experiment	13
3. Accelerator	18
4. M6S Beam Line - Stages 1 and 2	20
5. M6S Beam Line - Stage 3	21
6. Single Arm Spectrometer	25
7. One Third Overlapped Rodoscopes	32
8. Multiplicity Counters	35
9. First Order TRANSPORT Matrix	46
10. Trigger Logic	49
11. Online Computer System	54
12. AVB Angle Averaging	56
13. Overview of Analysis	59
14. Transmission Correction	71
15. SAS Vertical Angle Acceptance	76
16. Radiative Processes	83
17. Invariant Differential Cross Sections - p_{\perp} Dependence	90
18. Invariant Differential Cross Sections - x Dependence	103
19. Invariant Cross Sections - x Dependence	119
20. Scaling Comparisons - p_{\perp} Dependence	128
21. Scaling Comparisons - x Dependence	134
22. Charge Distributions in $\bar{\nu}p$ Interactions	148
23. Quark Fragmentation Model	149

<u>Figure Number</u>	<u>Page</u>
24. Quark Fragmentation Model Predictions, $\nu + \nu$	152
25. Quark Fragmentation Model Predictions, $k + \nu$	155
26. Quark Fragmentation Model Predictions, $\nu + k$	157
27. Quark Fragmentation Model Predictions, For $(x-0.7)$, $k + \nu$	158
28. Quark Recombination Model	162
29. Recombination Model Predictions, Integrated Results	165
30. Recombination Model Predictions, Unintegrated Results	166
31. Particle Ratios	171
32. Fits to Quark Momentum Probability Functions	175
33. Fragmentation Model of Brodsky and Gunion	178
34. $(1-x_{\perp})^B$ Fits	181

LIST OF TABLES

<u>Table Number</u>	<u>Page</u>
I: Rodoscopes	32
VI: Spectrometer Wire Chambers	38
III: Systematic Uncertainties	87
IV: $(1-x_R)^B$ Fits, Reactions Without Charge Exchange	196
V: $(1-x_R)^B$ Fits, Reactions With Charge Exchange	197
VI: $(1-x_R)^B$ Fits, Integrated Cross Sections	198

I. INTRODUCTION

A. Background

The trend in experiments in elementary particle physics has always been to use increasingly more energetic particles for probes. This enables the fine structure of particles to be studied with increasing resolution. In studying hadron-hadron collisions, however, one is faced with an increasing multiplicity of particles which are produced in a single collision. For example, production of over twenty charged particles in a single event is not uncommon at 100 GeV. For the experimentalist it becomes a difficult if not impossible, task to identify and understand the details of these reactions; theorists also encounter difficulty in interpreting these events in detail. It is for this reason that inclusive experiments are performed.

In a single particle inclusive measurement, the rate of production of some particle type c , from a collision involving particle types a and b , is measured without regard to any other particles which may be produced. The reaction is denoted by

$$a + b \rightarrow c + X$$

where X includes everything not observed. The Lorentz invariant cross section is written as

$$E_c \frac{d^3\sigma}{d^3p_c} = f(s, p_c)$$

Integrating the inclusive cross section, then, gives

$$\int \frac{d^3p_c}{p_c} d^3p_c = \langle n_c \rangle \sigma_{\text{TOTAL}}^{ab}(s),$$

where $\langle n_c \rangle$ is the mean multiplicity of c-type particles in all ab collisions.

This merely reflects the fact that reactions which produce more than one c-type particle will be counted more than once when the integral over all c momenta is taken.

In experiments with unpolarized beams, the invariant cross sections do not depend on rotations about the beam axis. There are, therefore, only three independent variables. We used the set s , $|\vec{p}_c|$ and θ .

Thus, inclusive cross sections are a statistical like sampling of all available exclusive processes, i.e. those in which all observables are completely determined and, hence, exclude any other possible final state. Our hope in using this approach was to average over the uninteresting details of a reaction, leaving a distribution which displays the salient regularities of the physics.

The topic of this thesis centers on the inclusive cross sections in the projectile fragmentation region. The process of projectile fragmentation is sketched in Figure 1. The beam particle passes by the target particle. There is an interaction between particles A and B. Particle A may then fragment, producing several particles, including particle C which is detected. Since particle A had, initially, a very high momentum in the laboratory frame of reference, its fragments will

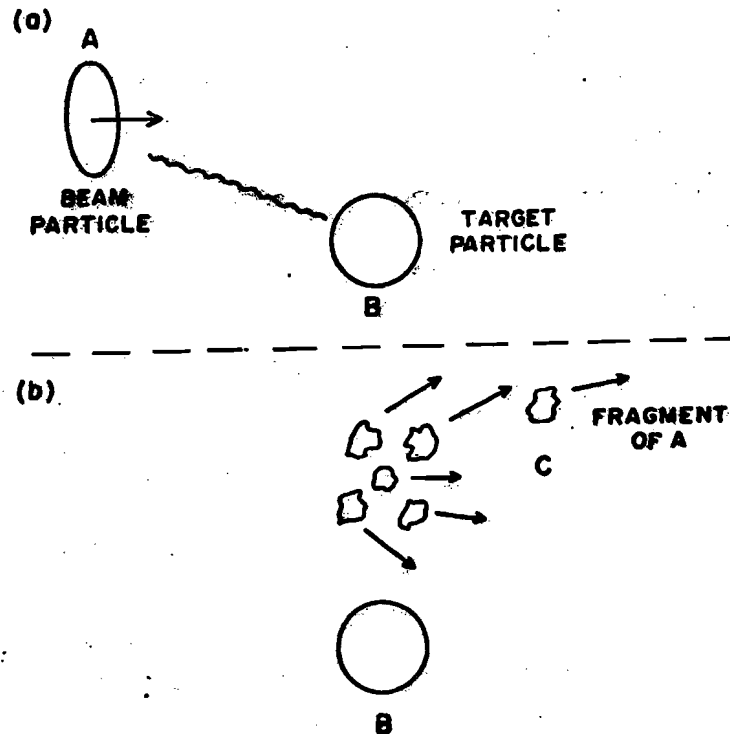


Figure 1
Beam Fragmentation

also tend to have a considerable amount of forward momentum. Particle B, the target, may also fragment in this process. Because the target particle is at rest in the laboratory, its fragments tend to move more slowly. In our experiment, we only looked at high momentum particles in the forward direction, so we would see essentially only fragments of the beam particle. This is roughly in the range of Feynman $x_F \equiv p_{\perp}^{C.M.} / p_{\text{max}}^{C.M.}$ from 0.2 up to 0.8.

Experiments have been performed previously to study the fragmentation region of the proton at high energies. These have included both fixed target experiments at Fermi National Accelerator Laboratory¹ and colliding beam experiments at CERN.² In addition, some bubble chamber measurements with incident pions obtained limited statistics in the pion fragmentation region.³ However, particle identification of the detected fragment in these latter experiments was limited. Our experiment extended the data to include particle beams of π^+ 's, π^- 's, K^+ 's, K^- 's and \bar{p} 's as well as protons. In addition, we achieved reasonable statistical accuracy for most reactions and had excellent particle identification. Thirty-six possible reaction types were measured at energies of 100 and 175 GeV. Some additional data were taken at 70 GeV.

B. Experimental Overview

The overview of our experiment is shown in Figure 2. Charged pions, kaons, and protons with momenta p_A of 100 and 175 GeV/c were selected by the beam line and were focused to a spot on the proton (LH_2) target. The spectrometer was set at an angle θ with respect to the incident beam axis. It accepted particles which were produced at a desired momentum p_C as a result of an interaction at the target. The experiment measured the single particle inclusive cross sections at various p_C and θ or p_{\perp} values. Our kinematic coverage was in the range from $p_C = 20$ GeV/c to $p_C = p_A$ and from $p_{\perp} = 0.1$ GeV/c to $p_{\perp} = 1.25$ GeV/c. At a given time, the beam line could provide identified pions, kaons, and protons of a given energy and charge. Similarly, the spectrometer could simultaneously measure yields of pions, kaons, and protons of a given momentum and charge. Spectrometer measurements were made for charge polarities which were the same and opposite to those of the beam. In addition to measuring the cross sections, the target area was instrumented with a variety of detectors which allowed the measurement of the charge multiplicity and pseudo-rapidity of the interaction that produced the particle detected in the spectrometer. Since this charge multiplicity information constituted information over and above that obtained in a purely inclusive treatment, this type of experiment is sometimes termed semi-inclusive.

$A + B \rightarrow C + \text{ANYTHING}$

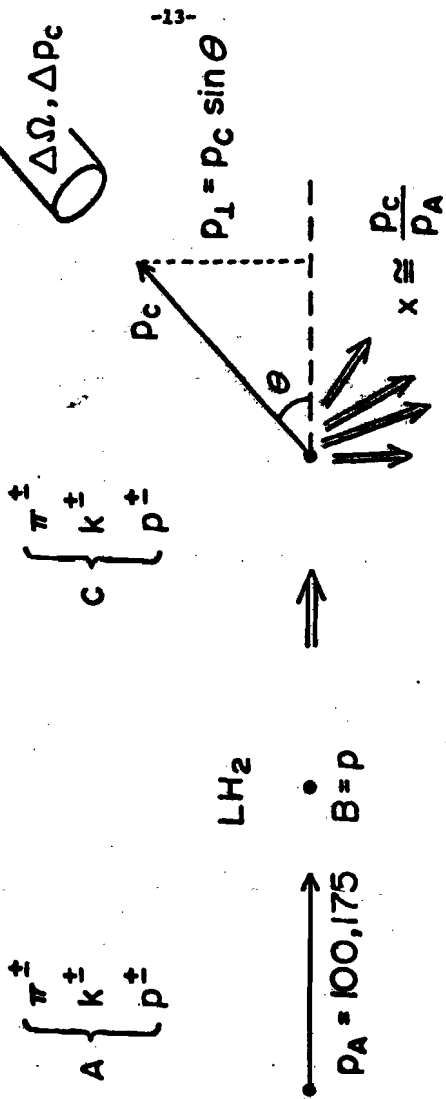


Figure 2
Overview of the Experiment

This experiment was undertaken as a joint effort by members of five institutions: Brown University, CERN, Fermi National Accelerator Laboratory, Istituto di Fisica and Istituto Nazionale di Fisica Nucleare in Bari, Italy, and M.I.T. The experiment ran in a two-year period from the Fall of 1975 to the Summer of 1977 and used over 2500 beam hours for data taking.

The data analysis being performed at M.I.T. for this experiment has been broken up into three parts. Information concerning the associated charge multiplicity will be analyzed by L. Votts.⁴ Cross sections with x_T above 0.7 will be the subject of a Regge pole analysis by W. Aitkenhead.⁵ The cross sections with x_T below 0.8 are the topic of this thesis.

C. Physics Motivation

The idea that hadrons are composed of quarks has had amazing success in explaining many of the static properties of the hadrons. Predictions concerning internal quantum numbers, mass differences, and magnetic moments agree well with experiments.

In deep inelastic electron-nucleon scattering, Bjorken scaling arises out of a model where the nucleons are composed of pointlike, quasi-free constituents called partons.⁶ Inelastic electron- and neutrino-hadron experiments have shown that these partons can have the quantum numbers of quarks. Thus the quark idea conceivably can play a role in explaining the underlying dynamics of lepton-hadron processes.

In hadron-hadron interactions, the quark hypothesis has had a more limited role in the models of the dynamics. Most of the work has been directed at the high transverse momentum regime.^{7,8} The reasoning is that these hadronic processes can come about only through the hard, large angle scattering involving the hadron's pointlike constituents.

Recently there have been several models developed which concern themselves with low transverse momentum processes. Three of these models will be examined and their predictions compared with our data. These models are based on (1) a quark fragmentation ordering scheme, (2) a quark recombination picture, and (3) a quark counting and phase space idea. All three

of these theories rely on the quark content of the hadrons involved in order to predict the beam fragmentation distributions. These models are attractive in that they may lead to a unified picture in which to understand the static properties of hadrons, lepton-hadron interactions and hadron-hadron interactions.

II. EXPERIMENTAL DETAILS

A. Accelerator

The experiment was performed at Fermi National Accelerator Laboratory in Batavia, Illinois. The accelerator, a proton synchrotron, is shown schematically in Figure 3. The accelerator delivered 400 GeV protons for an average of one second every cycle. Each cycle lasted an average of 12 seconds.

Protons were produced by ionizing hydrogen gas. These protons were successively accelerated to 750 keV by the Cockcroft Walton, to 200 MeV by a linear accelerator, and then to 8 GeV by a booster synchrotron. The protons entered the main ring where they coasted while the preacceleration cycle was repeated 12 more times to bring the total number of protons to over 2×10^{13} .

The protons in the main ring were grouped into 1113 bunches which were spread uniformly throughout the ring's 6.28 km circumference. This bunching of the particles had the effect of forcing the extracted protons to appear in charge buckets separated by 19 ns. The protons were then accelerated to 400 GeV by the main ring and extracted over a period of about a second. The extracted protons were shared between the Meson Laboratory, Proton Laboratory, and the Neutrino Laboratory so that several experiments could run simultaneously. Our experiment was located in the M6E beam line of the Meson Laboratory.

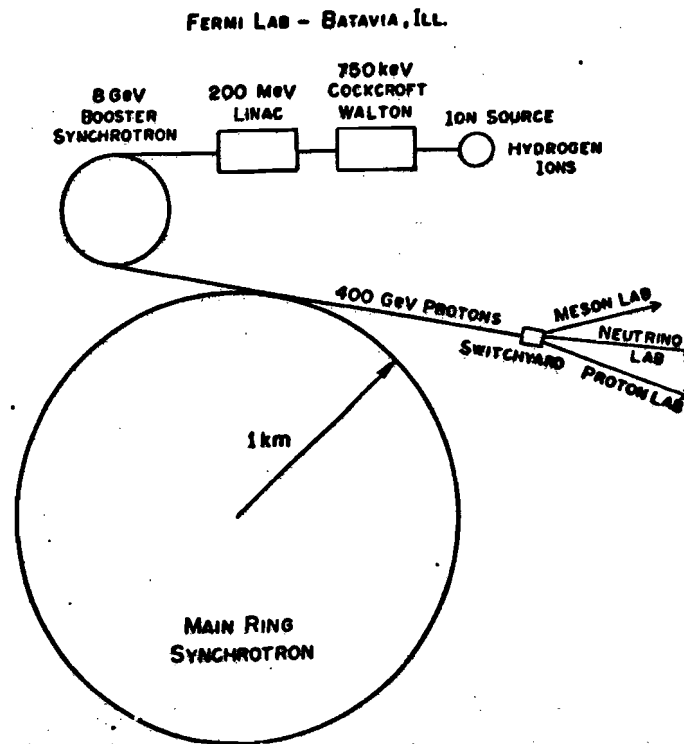


Figure 3
Accelerator

B. M6E Beam Line

The basic configuration of the beam line and spectrometer elements has been described previously and the details may be found in reference 9. Only a brief description, with the emphasis on changes and additions to the basic configuration, will be described here.

The M6 beam line was one of six beam lines in the Meson Laboratory and was situated at an angle of 2.7 mr with respect to the extracted proton beam. The beam line limited the angular and momentum acceptance of the beam and determined the momentum, trajectory, and identity of each particle that entered it. It did this with the aid of a system of dipole and quadrupole magnets, adjustable collimators, scintillation counter hodoscopes and gas Cerenkov counters.

A sketch of the M6 beam line is shown in Figures 4 and 5. The 400 GeV protons from the accelerator impinged on a beryllium wire, which acted as the meson production target. The interactions at the production target produced a spray of particles of various types and momenta. The magnetic quadrupole elements acted as lenses to form a point to parallel to point imaging system in the first stage. This imaging system collected the particles which passed through the aperture stops and imaged them at the first focus. These aperture stops were adjustable collimators which limited the vertical and horizontal angular acceptance of the beam. The septa and main bend magnets (mag-

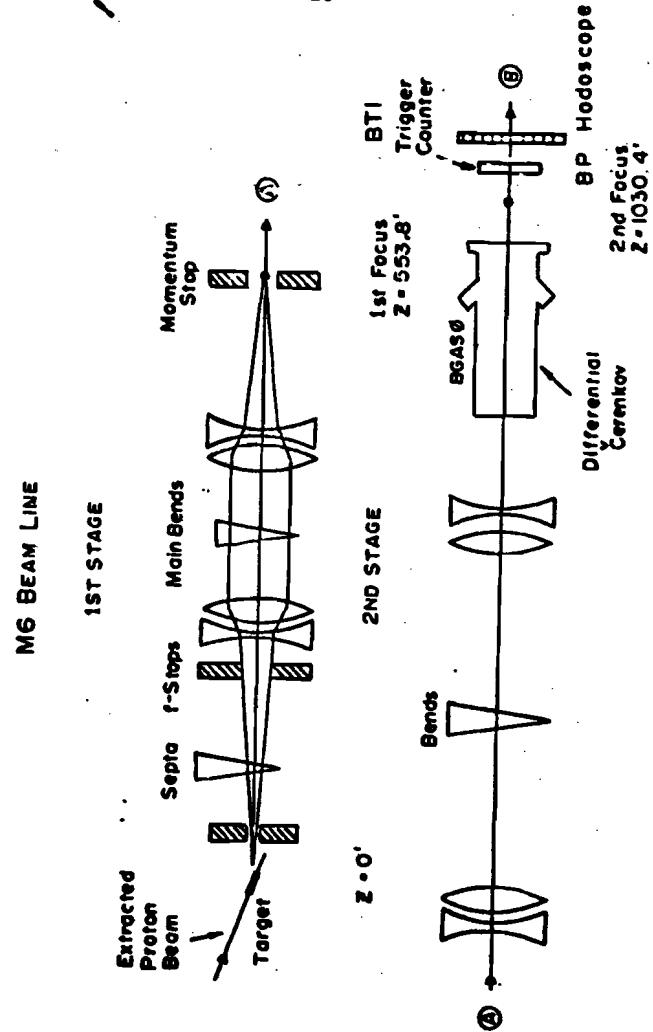


Figure 4

3RD STAGE

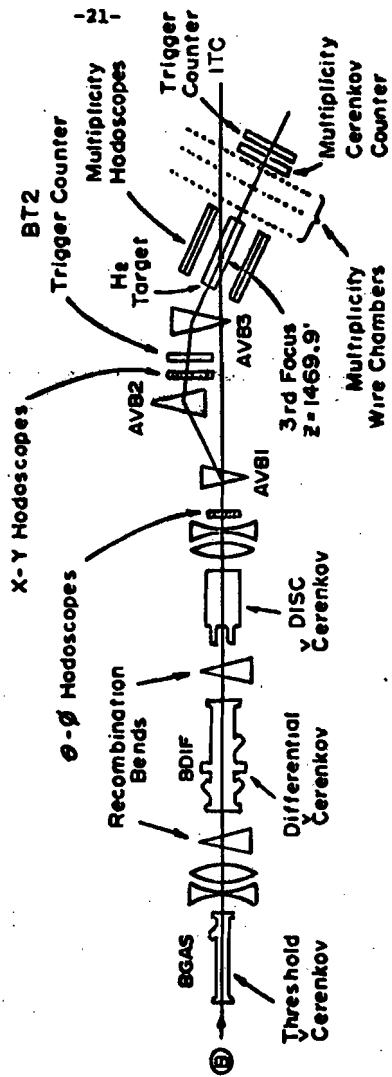


Figure 3
M62 Beam Line - Stage 3

netic dipole elements) were set to allow only particles with the desired charge polarity and momentum to pass through the system. Specifically, these magnets dispersed the beam horizontally at the first focus according to the momentum of the particles in the beam. The momentum stop collimator was adjusted to transmit only particles with a momentum deviation of less than $\pm 0.4\%$ from the nominal setting.

The second stage was also a point-to-parallel to point imaging system and acted mainly as a clean up stage to filter out stray particles. Additional momentum dispersion was introduced by a bend magnet. Also in this stage was a gas Cerenkov counter, BGAS, used for particle identification. At the focus of this second stage was a trigger counter BT1 and the momentum hodoscope, BP, which tagged the momentum of the particle.

The third and final stage was again a point to parallel to point imaging system and was the most heavily instrumented of the three stages. Particles leaving the second focus first passed through BGAS, another gas Cerenkov counter. They were then focussed into a parallel beam by the first set of quadrupole lenses. In this section there were two differential gas Cerenkov counters which required a parallel beam to operate satisfactorily. Also in the parallel region were bend magnets, which recombined the momentum-dispersed beam so that the final focus would be achromatic. The last set of lenses focussed the parallel beam onto the liquid hydrogen target. En route to

this third focus, the particles passed through the θ - ϕ and X-Y hodoscopes, and also through the second trigger counter, BT2. The θ - ϕ and X-Y hodoscopes allowed the angle and position of each particle at the target to be determined. The AVB magnets allowed the scattering angle to be varied and will be described in section D. The other counters, wire chambers and hodoscopes surrounding the target area were used to measure the charge multiplicities associated with an interaction and will be described in sections F and G.

In addition to the major magnetic components described above, there were a number of small trim magnets which are not shown in the figures. These trim magnets could make minor changes in the steering of the beam. These adjustments were necessary both in the initial alignment of the beam and also in the course of running when the extracted proton beam shifted slightly in position.

C. Single Arm Spectrometer

The spectrometer functions were similar to those of the beam line. Any scattered particle entering the acceptance of the spectrometer had its momentum, trajectory and identity determined. The spectrometer is sketched in Figure 6.

Particles were collected from the hydrogen target by the first set of quadrupole lenses. They were then focussed into a parallel beam in order to allow their proper identification in the differential gas Cerenkov counter, SDIF. A small bend magnet preceding this counter swept low energy particles out of the acceptance of the counter. In addition the particle's vertical angle was mapped into vertical displacement in the parallel region and was tagged by the vertical angle hodoscope (VAL). The second set of lenses brought this parallel beam to a focus. Between the lenses and the focus was the string of four bend magnets, which were used to analyze the momentum of the scattered particle. One set of wire chambers before the bend magnets and three sets after them were used to track the horizontal and vertical trajectories of the particles across the magnets. The particles also were required to pass through the two trigger counters ST1 and ST2 before they were accepted.

The particle identification in the spectrometer was provided by the three gas Cerenkov counters SGAS1, SGAS2, and SGAS3, in addition to SDIF. Also, a pair of electron shower

SINGLE ARM SPECTROMETER

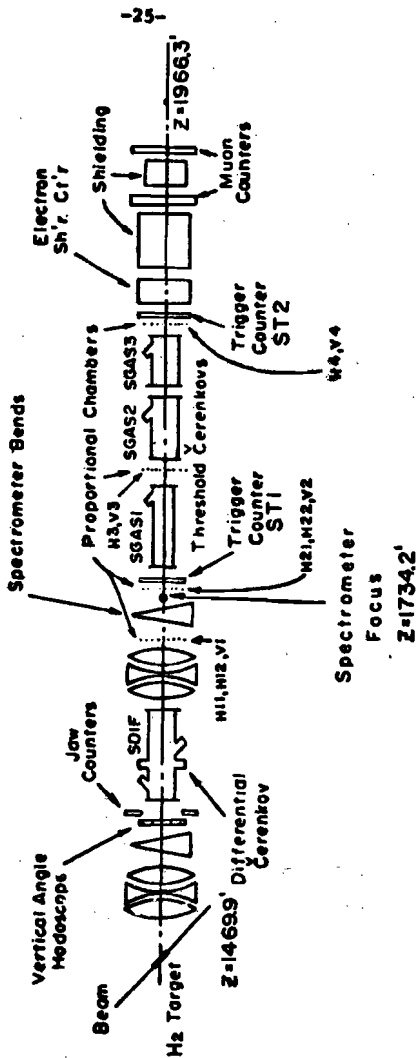


Figure 6

counters and a muon calorimeter were used to detect leptons.

Unlike the beam line, the spectrometer had no adjustable collimators. The total acceptance was limited only by the apertures of the magnets themselves. In our analysis, however, we have chosen to use a smaller acceptance defined by software cuts on the coordinates.

All the magnets in the beam line and spectrometer were controlled by a computer system. Magnets could be set to specific values by simply typing on a computer console. In addition the current and voltage readings of the magnet power supplies could be monitored and displayed.

For the bend magnets, more accurate monitoring was desired. These magnets had small dummy magnets, of identical construction to the full sized magnets, placed in series with their power supplies. These dummy magnets then had their magnetic fields monitored with both an NMR probe and a rotating coil device, known as a Rawson probe.

D. AVB System

Because the spectrometer was 500 feet long it was impractical to move it in order to measure the cross sections at different scattering angles. Instead, the beam was steered vertically, through different angles, onto the target by a system of three bend magnets known as the angle varying bends (AVB). Since the scattering angle was varied in the vertical plane and the momentum analysis was performed in the horizontal plane, measurements on one variable were decoupled, to first order, from measurements on the other.

These bends could either steer the beam down onto the target to make a positive angle with respect to the spectrometer axis, or steer it up onto the target to make a negative angle. The system was set so that the beam crossed the 0° axis at the center of the target cells.

To allow the beam to thread through the center of the apertures of these magnets, the last two magnets were mounted on hydraulic jacks, which could be operated remotely in the counting house. The jacking system imposed a limit of approximately 100 μ r on the positive angle. In addition, in order to keep the incident beam centered on the Y hodoscope and the BT2 trigger counter, a separate jack stand was used to support these counters. This jack stand was raised and lowered along with the AVB magnets.

E. Target Assembly

The target assembly held six different targets:

<u>Cell No.</u>	<u>Contents</u>	<u>Length</u>
1	Liquid hydrogen	10"
2	Liquid hydrogen	20"
3	Liquid deuterium	10"
4	No target	
5	Dummy or replica (empty)	10"
6	Dummy or replica (empty)	20"

Each target was placed in an insulated and evacuated chamber. The liquid hydrogen and liquid deuterium were produced by liquefying gas inside the target assembly via two closed-loop refrigeration systems attached to the assembly. These refrigeration systems produced very cold helium gas, through the throttling process, which entered a heat exchanger. The hydrogen (or deuterium) gas condensed on the exchanger and flowed into the target cell. Dummy targets were constructed to be identical to the liquid targets but remained empty. The target assembly was motorized so that the desired target could be positioned either locally or, remotely, at the counting house.

The target assembly was mounted on a motorized tilt stand. This tilt stand could be moved so that the targets always remained parallel to the incident beam when the AVB system changed the scattering angle. The tilt system pivoted about

the midpoint of the target cells. In addition to the target assembly, all of the counters, hodoscopes and wire chambers used to measure charge multiplicity were mounted on this tilt frame.

F. Scintillation Counters and Hodoscopes

The scintillation counters used in the beam line include the two trigger counters, BT1 and BT2, the momentum hodoscope, BP, the θ - ϕ and X-Y hodoscopes and two sets of hole counters, BT ϕ and BJAWS. The two trigger counters defined the acceptable aperture of the beam line. A particle was required to pass through both counters before signals from any other counters could be considered valid. In addition, signals from the two sets of hole or jaw counters, each with four movable jaws, were used in the third stage of the beam line to veto the signals from the trigger counters. In this way, we could define an acceptable aperture smaller than the physical sizes of the trigger counters. These jaw counters, which are not shown in the figures, effectively eliminated any stray particles or beam halo from triggering our system. Signals from another counter, dE/dx , not shown in the figures, and signals from BT1 were used to provide pulse height information. This pulse height information was used to monitor the double bucket rate: i.e. the rate at which two or more particles came down our beam line but were not resolvable in time by our counters.

The momentum hodoscope, BP, consisted of thirty scintillation counters, each 2.5 mm wide and placed laterally, in the horizontal direction, across the beam. This hodoscope was placed at a location with a momentum dispersion of 4.44 cm for each percent deviation from the central or nominal momentum.

From a knowledge of which element was struck, we could determine the incident particle's momentum to within .06% by the formula

$$\phi_{\text{incident}} = \frac{X(\text{BP})}{4.44} \theta$$

where $X(\text{BP})$ is the horizontal displacement at the BP hodoscope in centimeters.

The θ - ϕ and X-Y hodoscopes were fabricated according to a new design employing fiber optic light guides and were able to achieve a 1 mm resolution. Each hodoscope contained two rows of scintillators each 3 mm wide except for the end pieces which were only 2 mm wide. These two rows were arranged to overlap by 1 mm to provide a 1 mm wide logical bin as shown in Figure 7. The number of elements in each hodoscope is listed in Table I. The θ and X hodoscopes were used to determine the horizontal position and angle of an incident particle at the midplane of the target. Similarly the ϕ and Y hodoscopes were used to derive the vertical angle and position. The quantities were calculated by assuming that the entire distance between the θ - ϕ hodoscopes and the hydrogen target acted as a drift space: i.e. that there were no effects due to the presence of magnetic elements and that simply straight line projections of particle trajectories were valid. This assumption was a slight fiction in the region of the AVB magnets, but this was ignored, since the effect was small. The calculation, then, for the incident horizontal angle was

Figure 7
ONE THIRD OVERLAPPED HODOSCOPES

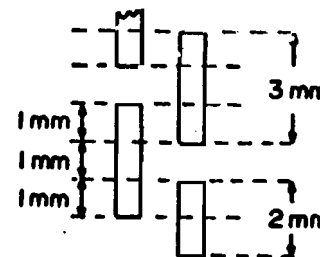


Table I: Hodoscopes

Name	Distance From Target Midplane	No. of Elements	Element size	1/3 Overlapping	Decode Sense Horiz.
BP	133.23 m	30	2.5 mm	No	Horiz.
B θ	22.20 m	8	3 mm	Yes	Horiz.
B ϕ	21.78 m	8	3 mm	Yes	Vert.
Bx	5.99 m	11	3 mm	Yes	Horiz.
By	5.95 m	8	3 mm	Yes	Vert.
VAL	25.80 m	10	6.5 mm	Yes	Vert.

* For hodoscopes with one third overlapping, the end elements are 2/3 the size of the central elements.

$$\theta_{\text{incident}} = \frac{X(B\theta) - X(BX)}{Z(B\theta) - Z(BX)}$$

where $X(B\theta)$ and $X(BX)$ are the horizontal displacements of the particle from the central trajectory at the θ hodoscope and the X hodoscope, respectively, and $Z(B\theta)$ and $Z(BX)$ are the distances of the hodoscopes from the hydrogen target midplane.

The position at the target midplane is simply:

$$X_{\text{midplane}} = X(BX) + \theta_{\text{incident}} Z(BX)$$

Similarly for the vertical coordinates, we have

$$\phi_{\text{incident}} = \frac{Y(B\phi) - Y(BY)}{Z(B\phi) - Z(BY)}$$

$$Y_{\text{incident}} = Y(BY) + \phi_{\text{incident}} Z(BY)$$

In the spectrometer our most important counters were the two trigger counters ST1 and ST2, through which scattered particles had to pass to be considered valid events. Additional trigger counters, SPS and ST3, were used as triggers for special studies. The hole counter SJAWS, with four movable jaws, provided signals which were used on occasion as a veto of the trigger counter signals in order to define a smaller triggering acceptance. However, this counter was not used in our analysis.

The vertical angle hodoscope (VAL) is a one-third overlapped hodoscope with ten 6.55 mm elements. This hodoscope was placed in the parallel region of the spectrometer. In this region production angles are translated into displacements from the central axis. This hodoscope, therefore, told us the ver-

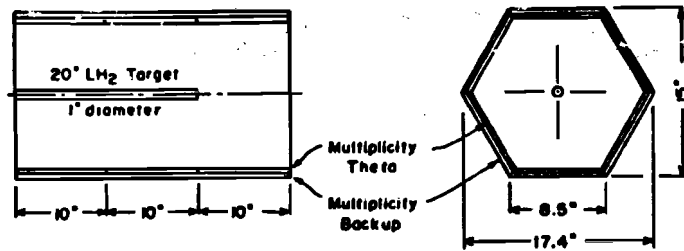
tical angle coordinate of an event directly.

In addition to measuring particle trajectories, scintillation counters placed around the target were used to measure the charge multiplicity of an interaction. A small trigger counter, ITC, with a hole in the middle, and placed 1.7 meters downstream of the target midplane and at 0° with respect to the beam axis, was used to signal the presence of an interaction but would not fire if the beam particle went straight through the hole.

The multiplicity hodoscope is illustrated in Figure 8. It was made with six slabs of scintillator arranged in the shape of a hexagon. Each slab had two layers. The inner layer was segmented into three separate counters. Both discriminated and pulse height information were available for these counters. The outer layer was a single piece of scintillator viewed with two phototubes. A signal from an inner layer counter required the presence of a signal from the outer layer counter in order to be valid. This reduced our sensitivity to contamination from delta rays. The multiplicity information in this region amounted to essentially counting the number of valid signals.

Another element of the multiplicity counter array was the multiplicity Cerenkov array which was placed directly in front of the ITC counter. This was not a scintillation counter, but was a hexagonal piece of plastic, segmented into six counters as shown in Figure 8. The amount of Cerenkov light produced

MULTIPLICITY TARGET HODOSCOPIES



in a piece of plastic is proportional to the number of charged particles traversing it. Pulse height information thus gave us the charge multiplicity in this region. Further information on the multiplicity system will be found in the Ph.D. thesis of L. Votta.⁴

MULTIPLICITY CERENKOV COUNTERS

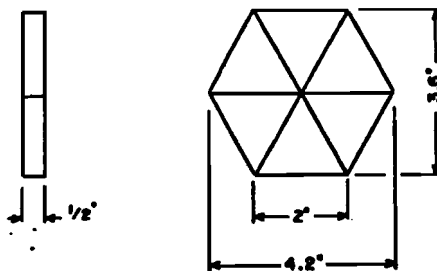


Figure 8

G. Multiwire Proportional Chamber System

Our experiment had two logically independent multiwire proportional chamber systems. One system was in the spectrometer and was used to measure the trajectories of the detected particle. The other system was situated just downstream of the target. This system was used to measure the charge multiplicity of hadronic interactions.

There were a total of ten chambers in the spectrometer system, as indicated in Figure 6. Their locations with respect to the middle of the hydrogen target and their number of wires are listed in Table 2. The "H" preceding the name indicates that this chamber made measurements of horizontal position. The "V" chambers made measurements of vertical position. They are not indicative of the direction in which the wires are strung. Each chamber had wires which were spaced 2 mm apart. The pair of wire planes H11 and H12, and also the pair H21 and H22, were located at approximately the same distance from the target but were shifted 1 mm laterally with respect to each other. This allowed us to have two horizontal position measurements with effectively a 1 mm resolution.

When a charged particle passed near a wire in a proportional chamber, a pulse was induced on the wire. This pulse was reshaped and delayed for approximately 1.3 μ sec. If the particle which went through the chamber generated a valid event trigger, the fast electronics sent a strobe pulse back to all

Table II: Spectrometer Wire Chambers

<u>Name</u>	<u>No. of Wires</u>	<u>Distance from Target Midplane (ft.)</u>
H11	64	169.73
V1	32	170.40
H12	64	171.06
V2	32	262.44
H21	64	263.64
H22	64	264.34
H3	160	375.04
V3	64	275.72
H4	160	455.53
V4	64	456.40

the chambers. This strobe gated the pulses from the wires into the data registers. When the computer began an event read-in cycle the wire chamber interface interrogated the chambers for struck wire information and transferred it to the computer. Further information on the spectrometer wire system can be found elsewhere.¹⁰

Essentially five raw coordinates were required from the spectrometer wire information. They were the projections in angle and position of the particle trajectory in the vertical plane, ϕ_f and y_f at the focus of the spectrometer; a similar pair of projections in the horizontal plane, θ_f and x_f ; and finally the horizontal position, x_1 , of the particle before it entered the bend magnets. These raw coordinates allowed us to determine the coordinates of the particle at the hydrogen target.

The coordinate x_1 could be determined just from the wire numbers of struck wires at H11 and H12. Since there were no magnetic elements in the space between the chambers H21, H22, H3 and H4, a particle was assumed to follow a straight line trajectory. A straight line least squares fit gave us the required projections. V1 was located before the bend magnets. However, to first order, the bend magnets had no effect on the vertical projection of the trajectory. So a linear first line fit involving all four vertical chambers gave us the coordinates ϕ_f and y_f .

The multiplicity wire system shown in Figure 5 consisted of nine chambers, each with 288 wires spaced at 2 mm intervals. They were grouped into three separate packages of three chambers, which were rotated 60° with respect to each other. Their construction, electronics and operation were similar to that of the spectrometer wire chamber and, in fact, shared some systems components. These chambers, however, had mylar plugs which deadened their response in the central portion of the chamber. These were used to eliminate some confusion arising out of the multiplicity information.

H. Gas Cerenkov Counters and Particle Identification

One of the strongest points of this experiment was the particle identification power provided by our gas Cerenkov counter system. We were required to identify pions, kaons and protons in the beam line and also in the spectrometer. For this purpose in the beam line we had one threshold Cerenkov counter, BGAS, two differential Cerenkov counters, BDIF and BDISC, and a differential counter used in the threshold mode, BGAS β . In the spectrometer, we had a differential counter, SDIF, and three threshold Cerenkov counters, SGAS1, SGAS2, and SGAS3.

Cerenkov light is emitted when the velocity of a charged particle exceeds the velocity of light in that medium. This condition is expressed as:

$$v > c/n \text{ or } \beta > \frac{1}{n}.$$

The light can be detected with photomultipliers. The threshold Cerenkov counters used this principle. By varying the pressure of the gas in the counter, and hence the index of refraction in the gas, we could change the minimum value of β to which we were sensitive. The index of refraction is related to the pressure approximately by

$$n-1 \approx \kappa P \text{ (PSI)}$$

where $\kappa = 2.1$ for He gas and $\kappa = 19.2$ for N_2 gas. So a typical strategy at a particular energy was to set the threshold so that pions would be counted. Because the velocity of the pions sa-

tisfies $\beta_\pi > \beta_K > \beta_p$, kaons and protons would not emit Cerenkov light. Note, however, that electrons and muons would count in this counter.

The number of photons incident on the photomultiplier is

$$N_\gamma = N_0 L \sin^2 \theta_c$$

where N_0 is some quality factor determined experimentally and which includes the efficiency of the optics, L is the length of the radiator, and θ_c , the angle of the Cerenkov cone of light, is given by

$$\cos \theta_c = \frac{1}{n\beta}$$

We would usually operate these counters just below the threshold for the next heavier particle in order to achieve the maximum detection efficiency. Note, however, that the index of refraction is a function of the wavelength of light, so that the wavelengths to which the photomultiplier is sensitive played a role in the settings for these counters.

The differential counters used the principle that the Cerenkov light is emitted in a cone with angle θ_c about the trajectory of the particle. By placing a slit system to pass light emitted at one angle, the counter can be sensitive to a single particle type. These types of counters offer greater rejection capabilities than do the threshold counters. However, they require the use of a parallel beam. Three of these differential counters, BDIF, SDIF, and BGAS β , also had phototubes which detected the Cerenkov light which did not pass through the

slit. In BGAS ϕ we "OR"ed the signals together to operate it as a threshold counter. In BDIF (and SDIF) we retained the two separate signals, called RING and ANTI signals, and used them in our particle identification strategy.

Before taking data, a variety of checks were made to ensure that the Cerenkov system was working properly. The efficiency of the threshold counters was determined by measuring the quality factor or, more precisely, N_0 times some average quantum efficiency of the photomultiplier tube. The different counters had movable mirrors to direct the ring of Cerenkov light through the slit system. These mirror settings had to be optimized. Furthermore, pressure scans were taken to determine the settings for maximum response.

The logic for particle identification was designed to be flexible so that different strategies could be used without incurring very much overhead. For the beam identification, however, it remained essentially unchanged. We used the following definitions:

- v = (BGAS or BGAS ϕ or BGAS·BDIFANTI or BGAS ϕ ·BDIFANTI)
vetoed by BDISC or BDIFRING.
- k = (BDISC or BDISC·BDIFANTI)
vetoed by BGAS or BGAS ϕ or BDIFRING
- p = (BDIFRING) vetoed by BGAS or BGAS ϕ or BDISC or
BDIFANTI.

The use of these strict definitions with the cross vetoing was an attempt to give the lowest amount of contamination while incurring only a slight loss in efficiency.

In the spectrometer, various strategies were employed. One strategy which was used for spectrometer energies below 100 GeV is listed below.

- v = Any set of counters along with SGAS1 or SGAS2·SGAS3.
- k = SGAS2 or SGAS2·SDIFANTI.
- p = Default.

As will be discussed later, all possible combinations of Cerenkov counter firings must be accounted for in the spectrometer.

I. Transport and Decode

The settings for the magnets in the beam line and the spectrometer were determined by the use of a beam optics program called TRANSPORT.¹¹ The basic idea of the program is that the coordinates, angles, and momentum of a particle after it has traversed an element of the beam line (magnetic dipole, magnetic quadrupole, drift space, etc.) are related by a transfer matrix to the coordinates, angles, and momentum of the particle as it entered the element, as indicated in Figure 9. This transfer matrix completely characterizes the element, up to second order in the power series expansion of the magnetic field about the central axis. The cumulative effect of all the beam elements, therefore, is simply the product of transfer matrices for every element in the beam line. By specifying constraints on the optics (e.g., magnification at a certain point, resolution, distance between magnets, etc.) one can have the program find values for the magnets which give the best fits.

The settings for the beam line did not differ from those used in reference 9. However, the spectrometer settings were changed to increase the vertical height acceptance at the hydrogen target. These parameters are listed in the appendix.

These parameters determined not only the required field values in the magnets, but also enabled us to decode the coordinates of a particle at the target from measurements of its coordinates after it had traversed several magnetic elements.

FIRST ORDER TRANSPORT MATRIX
FOR A MIDPLANE SYMMETRIC SYSTEM

$$\begin{array}{c}
 \left[\begin{array}{c} X \\ \theta \\ y \\ \phi \\ \delta \end{array} \right]_{\text{FINAL}} \\
 = \\
 \left[\begin{array}{cccccc}
 R_{11} & R_{12} & 0 & 0 & R_{16} & 0 \\
 R_{21} & R_{22} & 0 & 0 & 0 & R_{26} \\
 0 & 0 & R_{33} & R_{34} & 0 & 0 \\
 0 & 0 & R_{43} & R_{44} & 0 & 0 \\
 0 & 0 & 0 & 0 & 0 & R_{66}
 \end{array} \right] \\
 \left[\begin{array}{c} X \\ \theta \\ y \\ \phi \\ \delta \end{array} \right]_{\text{INITIAL}}
 \end{array}$$

Figure 9

The coordinates required were ϕ_f , Y_f , θ_f , X_f , and X_1 where these were determined from the spectrometer wire chamber information as described previously.

The required coefficients were determined, to first order, by inverting the matrix which described the transport from some initial location to some final location. For our decode, we required the matrix (and its inverse) for the transport from the target to the spectrometer focus, denoted by R_1 and R_1^{-1} , and the transport matrix from the wire plane V1 to the focus, denoted by R_2 and R_2^{-2} . Our decode then is given by:

$$\delta_p = \frac{x_1 - (R_2^{-1})_{11} x_f - (R_2^{-1})_{12} \theta_f}{(R_2^{-1})_{16}}$$

$$x_p = (R_1^{-1})_{11} x_f + (R_1^{-1})_{12} \theta_f + (R_1^{-1})_{16} \delta_p$$

$$\theta_p = (R_1^{-1})_{21} x_f + (R_1^{-1})_{22} \theta_f + (R_1^{-1})_{26} \delta_p$$

$$Y_p = (R_1^{-1})_{33} Y_f + (R_1^{-1})_{34} \phi_f$$

$$\phi_p = (R_1^{-1})_{43} Y_f + (R_1^{-1})_{44} \phi_f$$

These coefficients may be found in the appendix. In our analysis, all calculations were carried out to second order. However, the higher order terms are small.

J. Fast Electronics

The fast electronics is described in more detail in the Ph.D. thesis of W. Aitkenhead⁵, who had primary responsibility for maintaining the system and it will only be outlined here. There were basically two types of event: beam events and spectrometer events. The logic equations used for the event triggers are shown in Figure 10. The beam trigger, BT, is defined to be a coincidence between two trigger counter signals, BT1 and BT2, with vetoes by two sets of jaw counter signals, BTJ and BJAWS. These jaw counters ensured that a particle which went through both trigger counters but would miss the target would not trigger the system. Three other logic signals which were combinations of beam Cerenkov counter signals indicated whether the particle in the beam was a pion, kaon, or a proton. These latter signals were mutually exclusive. Furthermore, none of these signals would appear if the combination of Cerenkov signals indicated an ambiguous identification. Finally a BTC signal was defined to indicate the presence of any good particle identification in the beam. However, both the beam pion and beam proton signals could be counted down or sampled: i.e., we could ignore $2^{Ni} - 1$ pion or proton signals and only let the 2^{Ni} th signal appear in the BTC signal. The spectrometer trigger, ST, was simply the coincidence between signals from the trigger counters ST1 and ST2.

A beam event (BEV) was just a sampling of the beam trigger.

EVENT TRIGGER LOGIC

$$\begin{aligned}
 \text{BT} &= \text{BT1} \cdot \text{BT2} \cdot \overline{\text{BT}\emptyset} \cdot \overline{\text{BJAWS}} \\
 \text{BPION} &= \text{BT} \cdot (\text{BGAS} + \text{BGAS}\emptyset) \cdot \overline{(\text{BDISC} + \text{BDIFR})} \\
 \text{BKAON} &= \text{BT} \cdot \text{BDISC} \cdot (\text{BGAS} + \text{BGAS}\emptyset + \text{BDIFR}) \\
 \text{BPROTON} &= \text{BT} \cdot \text{BDIFR} \cdot (\text{BGAS} + \text{BGAS}\emptyset + \text{BDISC}) \\
 \text{BTC} &= \text{EPION} / 2^{N_1} + \text{BKAON} + \text{BPROTON} / 2^{N_2}
 \end{aligned}$$

$$\text{ST} = \text{ST1} \cdot \text{ST2}$$

$$\text{BEV} = \text{BT} / 2^{N_3}$$

$$\text{SEV} = \text{BT} \cdot \text{ST}$$

OR

$$\text{BT} \cdot \text{ST} \cdot \text{BTC}$$

Figure 10

BT. The rate of sampling, N_3 , was set according to the particular running conditions which were encountered. The beam events were an unbiased sampling of the beam conditions. These BEV's were essential to our analysis. The spectrometer event (SEV) was defined in two ways. One was simply as a coincidence between the beam trigger and spectrometer trigger. The other was to require, in addition, the presence of a BTC signal to ensure good particle identification. In particular we used this scheme when either beam pions or protons greatly outnumbered the beam kaons and it was necessary to use the countdown facility. By requiring BTC along with the countdown facility we could have approximately equal numbers of triggers from pion-, kaon- and proton-induced events.

The occurrence of an event, either a BEV or an SEV, caused several things to happen. First a signal, called "fast kill" was generated to freeze the electronics and ensure that the integrity of the stored information from the first event was not destroyed by the occurrence of a second event. The computer was then given an interrupt. Simultaneously, a gate signal was sent to the CAMAC¹² modules to latch all the logic signals, scintillation counter bit patterns and Cerenkov counter bit patterns associated with this event. In addition, this gate started the A/D converters which gave us information on the pulse height of various signals. Also the flux scalars were gated off. These flux scalars accumulated all the occurrences

of the signals BT, BPION, BKAON, and BPROTON from event to event. Finally, if the event was an SEV, a signal was sent to the multiwire proportional chambers to latch the wire number pattern in each chamber and prepare for computer readout. The use of this "fast kill" method obviated the need to make any dead time corrections.

K. Online Computer System

The online computer used for data taking was a PDP 11/45 operating under a real time executive called SPEX.¹³ The computer and its peripheral configuration is shown in Figure 11. Tasks running under SPEX could either be resident in memory or loaded into memory when requested. This allowed high priority tasks to respond quickly but let many lower priority tasks share the same area of memory.

The computer received interrupt signals from the event trigger logic. The interrupt handler would then initiate a direct memory access (DMA) transfer, through the BDØ11, of the information in the CAMAC crates into memory. If the event was an SEV, the computer would also start a DMA transfer, through the wire chamber interface, for the wire chamber information. At the completion of the DMA transfers, the computer then cleared the event information from the CAMAC crates and released the "fast kill", thereby allowing the electronics to accept another event. When enough events had been taken to fill up a buffer, the computer wrote the block onto nine track magnetic tape. Also, at the beginning and at the end of a run, status and scaler information was read by the computer and written onto magnetic tape.

In addition to the event logging duties, the computer produced histograms of incident beam particle distributions, spectrometer particle distributions, and associated multiplicity

information. These histograms could be displayed on storage scopes or on the electrostatic plotter as desired. This information was necessary to ensure that the experimental apparatus was performing satisfactorily. Finally, approximate cross sections were computed at the end of each run by the computer. Any wild fluctuations in these cross sections would alert us to the possibility of equipment failure or misadjustment.

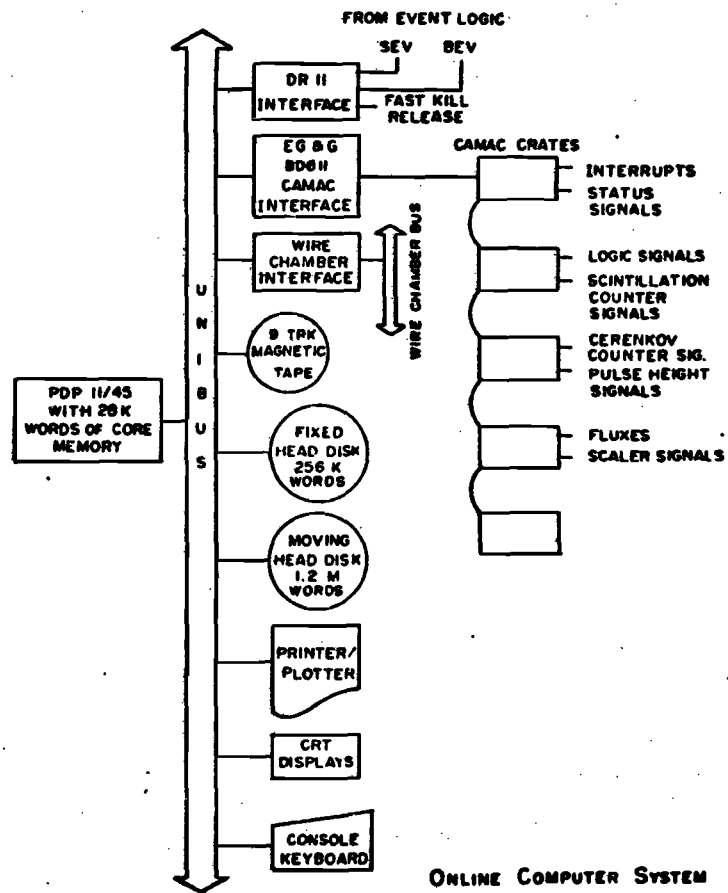


Figure 11

L. Data Taking

Prior to the actual taking of data, several setup tasks requiring the use of the beam needed to be completed. These included the timing and the checking of the efficiencies of all the counters and wire chambers in the system. Then extensive online studies were undertaken to ensure the proper operation of all elements of the system. In addition, the online studies provided us with the operating parameters of the experiment, such as the momentum calibration of the bend magnets and the final settings of the trim magnets.

The normal sequence of runs for a given kinematic point was

<u>Target</u>	<u>Multiplicity Cerenkov Counter</u>	<u>Sign of AVB Angle</u>
20° H ₂	IN	+
20° empty	IN	+
20° empty	IN	-
20° H ₂	IN	-

Both signs of the AVB angle were used to eliminate small offsets between the true spectrometer axis and the beam axis. This is illustrated in Figure 12. Our cross sections were averaged together with equal weightings for the two AVB signs. Thus, to first order, the final cross sections are independent of the offset, Δ .

Additional data were occasionally taken with the 10° H₂

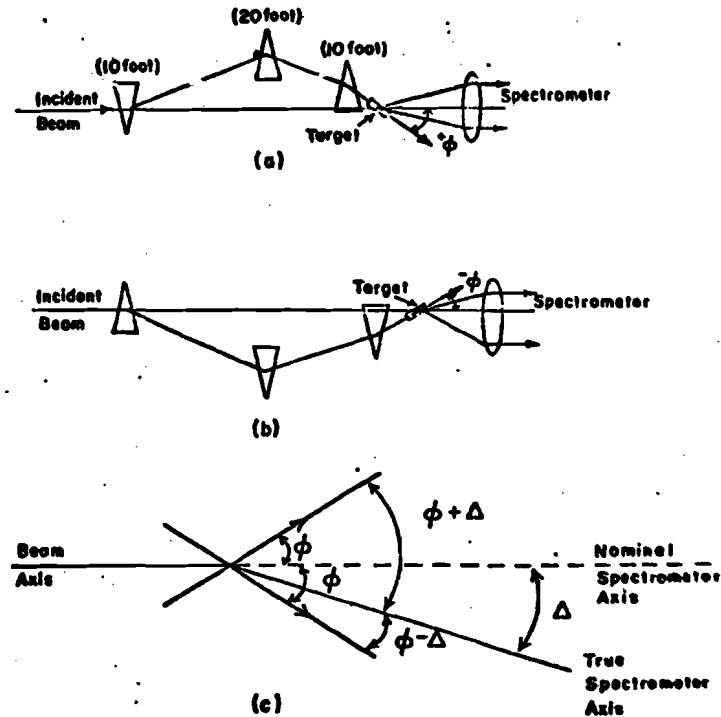


Figure 12
AVB Angle Averaging

and 10" empty targets in the same sequence as that with the 20" targets. These runs were used to check for any target length dependences in our data. Also the same sequence of runs was repeated with the multiplicity Cerenkov counter removed, but usually only at the smallest angle setting. This was done to check that the extra background, due to interactions in this counter, was being removed in the empty target subtractions.

Other special runs were taken in the course of the experiment. They included transmission runs, to measure our detection efficiency in the spectrometer; interaction trigger runs, to obtain charge multiplicity data; and "straight through" runs, to verify our settings of the magnets and the steering of the beam.

III. ANALYSIS

A. Overview

The data analysis was divided into three phases. In the first phase, a program called PASS 1 operated on the raw data tapes on a run-by-run basis and wrote a disk data set containing yields and fluxes. In the second phase, a program called PASS 2 used this data set to compute the actual cross sections for each reaction and wrote this into another disk data set. A program in the third phase combined the cross sections, subtracted the background, put in correction factors, and folded in systematic errors. This last program wrote these final cross sections onto yet another disk data set. The data flow is illustrated in Figure 13.

The raw data tapes were also used for studies to determine correction factors for the data and also to detect erroneous data. As an example, every run on every raw data tape was run through the computer in order to punch out selected information. This allowed us to calculate approximate cross sections by using the scaler information.

The data analysis at M.I.T. was performed on the Laboratory for Nuclear Science's IBM 360/65 computer system. This system had two IBM 2314 disks available for public storage and four IBM 2311 disk drives on which private disk packs could be mounted. The yields and fluxes from several hundred runs were

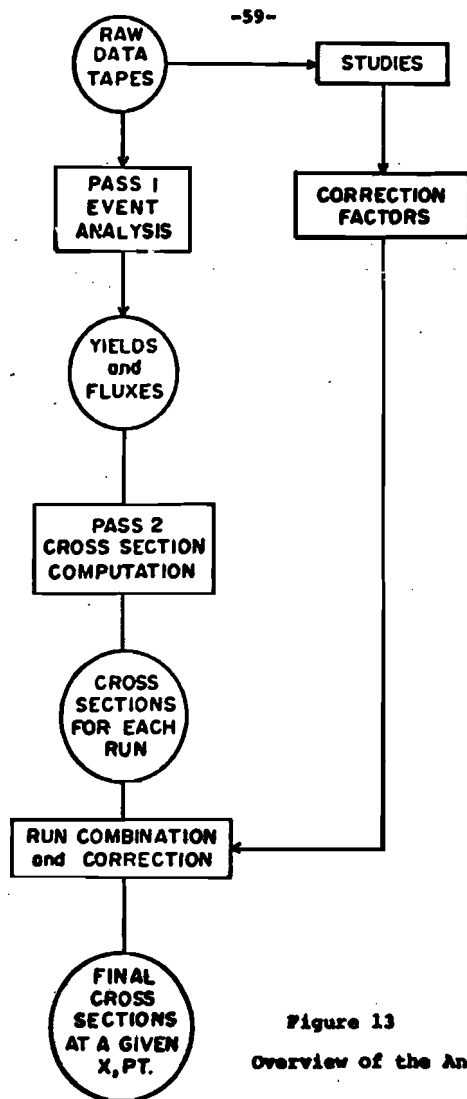


Figure 13
Overview of the Analysis

written by the PASS 1 program onto a single 2311 disk. The PASS 2 program reduced this information and used only a small dataset on the public disks to hold the resulting cross sections from all the runs. The last phase compressed the data even further and was able to write all the final cross sections into a dataset with only 100 kilobytes onto a public disk which was readily accessible by our fitting programs.

This thesis will describe the analysis of single bin cross sections; i.e., the whole aperture of the spectrometer at a particular kinematic setting was used to determine one cross section for a given reaction type. Information utilizing the associated multiplicity information will be the subject of a separate analysis.

The next sections describe each of the three parts of the analysis program. The last section describes the correction factors and their estimated errors.

B. PASS 1

The Pass 1 program performed an event by event analysis for each specified run. The raw data tapes were read in and each event had its bit patterns decoded. From these bit patterns, both the incident and production coordinates were calculated, if possible, for an SEV. In addition, the incident particle type and detected particle type were determined by a look-up procedure in a table specified as input for this run. This allowed the use of different Cerenkov counter strategies on a run by run basis. Finally, if the particle types were acceptable and the coordinates were within the acceptance cuts, the event was entered into the yield planes. Thus PASS 1 was the only event selection mechanism for the rest of the analysis.

For a beam event, only the incident particle types and coordinates were calculated. The moments of these beam coordinates and the statistics for each particle type were written out to the disk for PASS 2 processing.

For either type of event, the fluxes associated with the event were accumulated. These accumulated fluxes along with the "end of run" scalars were also written onto disk.

The SEV's used in our analysis were binned in production coordinates; i.e., production θ , production ϕ , and production θ . For this reason we did not need a decodable incident track. We required only that a particle have a non-ambiguous momentum hodoscope pattern; that is, having at least one and at most two

adjacent elements firing. The beam particle identification criteria were fairly tight, however. By this we mean that we only accepted Cerenkov patterns which we were fairly confident represented the desired particle type and rejected all other patterns which could have been made by two or more particle types. This gave us an unbiased selection as long as the fluxes used in the cross sections corresponded to these same criteria.

The events in the spectrometer were more complicated. Here we had to account for every particle produced that entered our acceptance. First we required good tracking in the spectrometer. This tracking was done by the spectrometer wire chambers. A good chamber was one which had at most three adjacent wires and a minimum of one wire which fired. The vertical tracking algorithm allowed the loss of any two chambers except the simultaneous loss of the first two chambers in order to still give a good vertical track. In the horizontal plane, there were two H1 chambers and two H2 chambers. At least one of each was required in addition to either H3 or H4 to give a horizontal track. The statistics on the number of tracking failures were written onto the disk and were used for an upward correction of the cross sections as described later.

Our particle identification criteria were determined by studies on the Cerenkov patterns which were the most likely to occur for the various particle types. All possible Cerenkov

patterns had to be identified. By a fitting procedure described later, we attempted to correct any possible misidentification using these criteria.

Finally, events were kept only if the decoded coordinates were within our acceptance. The acceptance we used for ϕ_p was

$$-1.8 \text{ mr} < \phi_p < 1.8 \text{ mr}$$

The acceptance plotted in the $\delta_p - \phi_p$ plane described a parallelogram. It had intercepts at values of

$$\phi_p^{\text{coupled}} = \pm 1.3 \text{ mr}$$

and

$$\delta_p^{\text{coupled}} = \pm 3.25 \text{ mr}$$

with sides whose slopes were

$$\frac{\delta \phi_p}{\delta \delta_p} = -0.015 \text{ mr/}\delta$$

and

$$\frac{\delta \delta_p}{\delta \phi_p} = +5.5 \text{ } \delta/\text{mr}.$$

The total acceptance we used was 25 microsteradian percent.

These acceptances were determined by TRANSPORT predictions.

In addition studies were done to estimate the effect of smeared resolutions on these acceptances.

The final fraction of events which survived all the above criteria was about 30 to 35%. The largest loss occurred in the acceptance test which eliminated 50 to 55% of the events.

In addition to calculating yields and accumulating flux

on statistics, PASS 1 had a number of run diagnostic features. Histograms of coordinates, hodoscopes and wire chambers could be printed out. Various beam optics checks could be made on the data. Also efficiencies of all the hodoscope elements, wire chambers and Cerenkov counters were calculated and displayed. For this reason PASS 1 was used on selected runs to study and establish correction factors for the rest of the data.

C. PASS 2

The program PASS 2 was used to take the data from the disk file produced by PASS 1 and produce single bin invariant cross sections and errors for all the reaction types in a given run. The cross section can be written as

$$\frac{E_c}{p_c^2} \frac{d^3 \sigma^{ab \rightarrow cX}}{dp_c d\Omega} = \frac{YIELD}{FLUX} \frac{E_c}{p_c^2} \frac{1}{\Delta\Omega \Delta p_c N_0 \rho_{target} l_{target}/A} \frac{1}{CORRECTION FACTORS}$$

where ρ , l , and A are the target density, length and atomic number, respectively, and N_0 is Avogadro's number. $\Delta\Omega \Delta p_c$ is the acceptance of our spectrometer.

The yields put out by PASS 1 were not single bin yields, but were binned in finer units. Since we wanted single bin cross sections PASS 2 had to sum over the finer bins. However, to be more accurate, PASS 2 corrected each of the bins according to its expected variation over the acceptance.

The flux used was normally the accumulated flux, for that incident particle type, from all events. It was necessary in some cases to override this choice and use either the scaler information from the "end of run" scalers or a percentage of the BT flux determined by the fraction of the BEV's which were identified as the desired particle type. In any case, it was necessary to determine the fraction of the flux which could have produced an event in the yield planes. Recall, that to make an unbiased cut on the SEV's we must restrict the

flux to the same incident criteria that we placed on the SEV's. To do this we used the BEV events which should have represented an unbiased sample of events. We found the fraction of BEV's which passed the identical hodoscope and particle identification requirements and multiplied the PASS 1 flux number by this fraction. This was the number which had to be used for the flux in the cross section.

A number of correction factors were applied at this point. Some of these are called resolution corrections. One of these came from the angle offset. If there was mis-steering of the beam, the average angle of the incident beam would not be zero. Since the cross sections fall rapidly with increasing angle, it was necessary to correct for this offset by using the moments of the beam distributions determined from the BEV's. A second correction arose from the straight line approximation for the variation of the cross section across the bin. This correction is proportional to the second derivative of the cross section with respect to the scattering angle.

Another correction was needed because not all of the incident beam phase space could scatter with equal probability into the acceptance of the spectrometer. PASS 2 took the incident beam distributions and calculated an average acceptance function for a given set of acceptance cuts. This acted as an effective correction to the flux.

Additional corrections applied were for transmission and

decay of particles in the spectrometer. Also the tracking loss fraction, described in the PASS 1 section, was used in PASS 2. These are described in more detail in section E.

PASS 2 then wrote the single bin cross sections and their errors out on the disk. They were, however, put out in a form in which the corrected yields and corrected fluxes (weights) were recoverable for the purpose of combining runs.

D. Run Combination

This last phase searched the disk file produced by PASS 2 for all runs at a given kinematic point. A distinction was made between the two AVB angles which occurred at that point. For a given AVB angle and for each reaction and target type, the corrected yields and fluxes were recovered and summed over all runs of the same type. The background was then subtracted to give the cross section.

$$\frac{E_c}{p_c^2} \frac{d^3\sigma^{ab \rightarrow cX}}{dp_c d\Omega}(\pm) = \frac{E_c}{p_c^2} \frac{1}{\Delta\Omega \Delta p_c N_o \rho \ell / A} \times \left[\frac{\sum YIELD'_{FULL}(\pm)}{\sum FLUX'_{FULL}(\pm)} - \frac{\sum YIELD'_{EMPTY}(\pm)}{\sum FLUX'_{EMPTY}(\pm)} \right]$$

$$\Delta \left[\frac{E_c}{p_c^2} \frac{d^3\sigma}{dp_c d\Omega}(\pm) \right] = \left(\Delta_{FULL}^2 + \Delta_{EMPTY}^2 \right)^{1/2}$$

where the Δ_{full} and Δ_{empty} are the total errors coming from all runs in the sum of full or empty targets, respectively. The cross sections are then averaged, with equal weighting for the positive AVB angle and the negative AVB angle.

In addition, a number of corrections were applied to these data at this point. These will be described in the next section and include multiple scattering-acceptance corrections, the particle misidentification corrections, the double scattering corrections and the radiative corrections. The cross

sections were written onto the disk and were ready for plotting or fitting.

E. Corrections and Errors

This section is a summary of the various corrections applied, the means by which they were determined, and their estimated errors.

1. Transmission, Decay, and Absorption

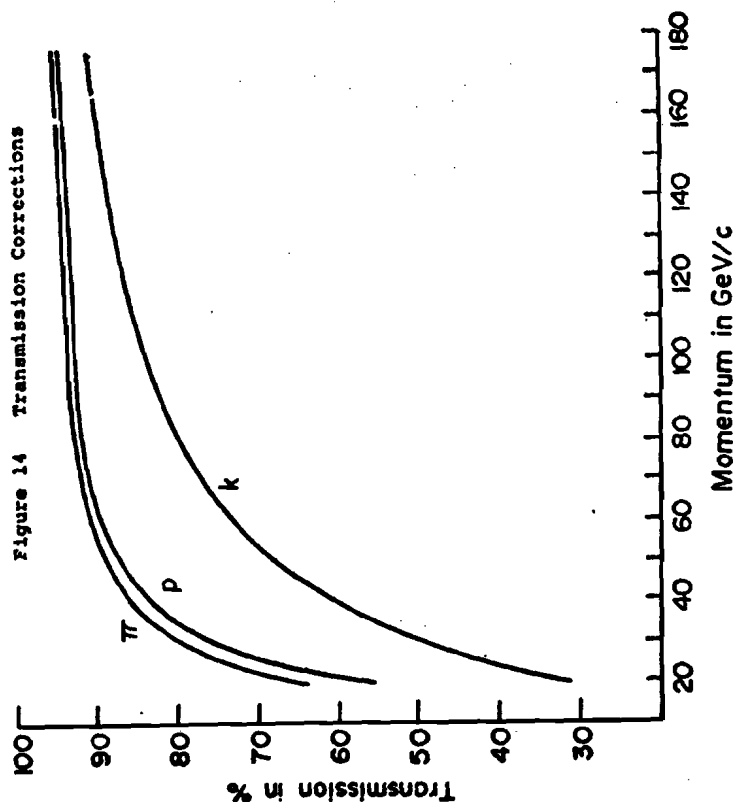
Events which fell within our acceptance but did not trigger the system were the result of several effects. (i) inefficiency in the trigger counters; (ii) absorption in the material of the spectrometer; (iii) decays which depleted particles from the spectrometer acceptance. These effects were studied by special "straight through" runs at 20, 30, 50, 100, and 175 GeV.

The transmission for a particle type α is defined as

$$t_{\alpha} = BT \cdot Ba \cdot ST1 \cdot ST2 / BT \cdot Ba$$

The transmission numbers were taken with both full targets and empty targets and with the multiplicity Cerenkov both in the acceptance and out of it. This gave us absorption numbers for the targets and the multiplicity counter. Interpolations were made for other energies. The increase in transmission with energy was attributed to the decrease in the total cross section, a decrease in the amount of gas used in the spectrometer Cerenkov counters and an increase in the number of secondaries from interactions which could still trigger the system due to the increased shrinkage of their production angles.

For pions and kaons, there was also the possibility of loss by decay. It was difficult to separate the different



effects. The assumption was made that the absorption loss scaled as the ratio of the cross sections. The transmission is given by

$$t_k = (1 - \text{absorption}) \times (1 - \text{decay loss})$$

A model was devised by W. Aitkenhead which predicted the loss from decays. Note that just as a secondary from an interaction with the material in the spectrometer could cause a trigger, a secondary from a decay process could also stay in the acceptance. This model predicted the probability of a decay which caused no triggers. Further details on this model and the transmission studies will be found in the thesis of W. Aitkenhead.⁵

The final total transmission numbers are plotted in Figure 14. The estimated errors on the transmission corrections are .03%, 0.3%, and 1% for pions, protons and kaons respectively. The errors on the absorption corrections are about 0.5%. The decay corrections are accurate to 0.1% for pions and 1% for kaons.

2. Particle Misidentification

Every spectrometer Cerenkov bit pattern in PASS 1 had to have a particle type associated with it. This introduced some error for the ambiguous definitions. By this we mean a definition in which more than one particle type could give rise to that Cerenkov pattern. For example, the pattern where no Cer-

enkov counter fired could be the result of inefficiencies in one or more of the counters and hence pions, kaons, and protons could give this pattern.

To calculate the correction to the particle identifications, a program was devised by R. Verdier of M.I.T. to fit the efficiencies of the Cerenkov counters and branching ratios for a run. For each of the five spectrometer Cerenkov signals, SGAS1, SGAS2, SGAS3, SDIFR and SDIFA, we defined the efficiencies for pion, kaon, and proton detection, e.g. $\epsilon_{1\pi}$, ϵ_{1k} , ϵ_{1p} etc. This gave us fifteen variables. In addition, we defined the branching ratios B_{ab} to be the fraction of beam events of type a which went into spectrometer type b. This gave nine variables, but we had the constraints that

$$\sum_b B_{ab} = 1$$

which reduced the number of variables to six. We were left with 21 independent variables. We also had, for a given beam particle type, 32 numbers which were the number of times each of the $32 = 2^5$ possible Cerenkov patterns occurred in a given run. There were three beam particle types, so we were really trying to fit 21 variables to 96 numbers.

The initial assumption was that the signals were uncorrelated. This meant the Cerenkov pattern for a beam pion of

SGAS1 · SGAS2 · SGAS3 · SDIFR · SDIFA
would have had a probability to occur given by

$$B_{\pi\pi} \epsilon_{1\pi} (1 - \epsilon_{2\pi}) \epsilon_{3\pi} (1 - \epsilon_{R\pi}) (1 - \epsilon_{A\pi}) +$$

$$B_{\pi k} \epsilon_{1k} (1 - \epsilon_{2k}) \epsilon_{3k} (1 - \epsilon_{Rk}) (1 - \epsilon_{Ak}) +$$

$$B_{\pi p} \epsilon_{1p} (1 - \epsilon_{2p}) \epsilon_{3p} (1 - \epsilon_{Rp}) (1 - \epsilon_{Ap})$$

The program then searched for the minimum χ^2 and provided estimates for the errors of the parameters. The assignment of Cerenkov patterns to particle types gave us the misidentification numbers M_{ab} , which were the fraction of the events where particle type b was assigned to particle type a. Since every particle received some assignment, we had

$$\sum_a M_{ab} = 1$$

There were some physical processes which could not be fitted by the simple model. A process such as k's decaying into pions would give false efficiencies. However, by introducing an extra variable in the fit, which was related to the probability of this decay, good results could be obtained. The fits could then give slightly wrong efficiencies, but it was only the set of numbers M_{ab} which was relevant. These corrections were generally less than 2% but they occasionally were as large as 8%.

Although this procedure could be used on every run, it was too time consuming. Therefore only a few sets of runs, representing all Cerenkov strategies which were actually employed,

were fit and interpolated values were used to correct the cross sections. The error in the cross sections associated with this procedure is estimated at about 0.6%.

Since the beam particle identification was based on very stringent requirements, no correction was made. We estimate the error in the cross sections to be less than 0.1%.

3. Multiple Scattering and Acceptance

A particle originally within our acceptance could scatter out of it by multiple scattering and be lost. A particle could similarly scatter into our acceptance even if it was originally outside of the acceptance. However, since our acceptance was limited by steel apertures, this was unlikely. This net loss of yield had to be corrected. This effect was not taken into account by the transmission studies since only the central portion of the spectrometer was used in those studies.

A similar effect occurred when our acceptance cuts included part of an aperture stop. Again there would be a loss of particles which had to be counted in the yield.

A series of studies were undertaken to estimate these effects. The study consisted of taking ever smaller definitions of our acceptance in all three variables, θ_p , ϕ_p , δ_p . A typical plot is shown in Figure 15. The hope was that for a small enough acceptance, the cross section would be removed of these effects and stay constant. These studies were run at 20, 30, 50, and 100 GeV. At the high energy end, we expected only the

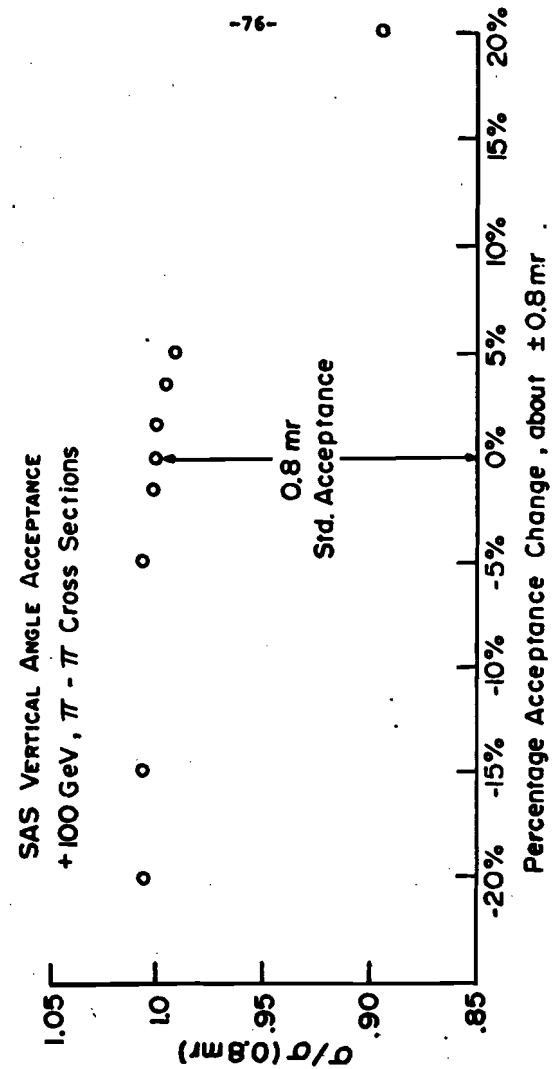


Figure 15

aperture stop effect to occur. We saw that we might have made a 1/2% error by using our normal acceptance. At lower energies the effect was not so clearly observed. However, we estimated the multiple scattering losses to the cross section to be $11 \pm 4\%$ at 20 GeV, $5 \pm 1.5\%$ at 30 GeV, $1 \pm 0.5\%$ at 50 GeV, and $0.5 \pm 0.5\%$ at higher energies.

4. Particle Tracking Loss

As mentioned previously, the percentage of tracks in the spectrometer which could not be decoded was recorded for every run. However, this number could not be used directly to correct the cross sections because some of the events which fell outside of our acceptance would also fail to track. In fact we expected a higher percentage of these events to be reflected in our total number of track failures.

By using straight through runs, which we knew gave events in our good acceptance, it was determined that the actual percentage of track failures due to electronic causes (i.e., noise or inefficiency of the wires) was rather constant at about 2%. In addition the number of ambiguous tracks (tracks of four or more adjacent struck wires or two or more non-adjacent struck wires) increased from near zero at 20 GeV to about 1% at 175 GeV. This was attributed to the increased multiplicity in interactions of the particle with material in the spectrometer and to increased production of delta rays. These numbers were used as our tracking corrections. The error in the cross sec-

tion from this determination was about 0.5% at 20 GeV, increasing to 0.75% at 175 GeV.

The tracking loss numbers recorded by PASS 1 were not used except for the runs where we had a complete chamber failure. These runs would have a larger number of tracking losses. For these runs, the increases in the recorded tracking loss numbers over the global average were used to boost the correction factors described above.

5. Double Scattering

A particle which was produced in an interaction at the target could interact again, producing more particles and increasing the apparent cross section. A procedure was devised to approximately correct for this effect. This method is an extension of the one used by Butler as originally suggested by L. Rosenon.⁹

We take the probability for a single scattering of particle type a, in a region dz in a hydrogen target, which produces a particle c in the solid angle dΩ with momentum p_c to be

$$P_1^{ac}(\theta_1, \phi_1, p_c) d\Omega dp_c dz = N_0 \rho_{LH_2} \frac{d^2\sigma}{d\Omega dp_c}(\theta_1, \phi_1, p_c) dz d\Omega dp_c$$

The probability of a double scatter occurring which produces a particle c in the solid angle dΩ₂ with momentum p_c is the integral of the probability for a single scattering, times the probability of surviving to the first scattering location, times

the probability for a single scattering, times the probability of surviving from the first location to the second and from the second to the end of the target. This must be summed over all possible intermediate particles:

$$P_2^{ac}(\theta_s, \phi_s, p_s) = \sum_b \int_0^l e^{-w_0 z} P_1^{ab}(\theta_1, \phi_1, p_1) \int_{z_1}^l dz_2 e^{-w_0(z_2 - z_1)} \times P_1^{bc}(\theta_s - \theta_1, \phi_s - \phi_1, p_s - p_1) e^{-w_0(l - z_2)} dz_1 dp_1 d\theta_1 d\phi_1$$

The z integrations are independent of the others and produce a term $\frac{l^2 e^{-w_0 l}}{2}$ where $w_0 = N_0 \rho_{LH_2} \sigma_{total}$. For the case $a = c$

we will assume only the terms $a = b = c$ contribute significantly.

For the case $a \neq c$ we will only keep the terms $a \rightarrow a + c$ and $a \rightarrow c + c$.

Writing this out we get for the case $a = c$:

$$P_2(\theta_s, \phi_s, p_s) d\Omega_s dp_s = N_0^2 \rho_{LH_2}^2 l^2 e^{-w_0 l} \times \int \frac{d^3\sigma}{d\Omega dp}(\theta_1, \phi_1, p_1) \frac{d^3\sigma}{d\Omega dp}(\theta_s - \theta_1, \phi_s - \phi_1, p_s - p_1) dp_1 d\theta_1 d\phi_1 d\Omega_1 dp_1$$

where $d\Omega_s dp_s$ is the acceptance of the spectrometer. Each of the cross section terms $\frac{d^3\sigma}{d\Omega dp}$ must contain δ function terms which correspond to the elastic scattering contribution. Thus we have three integrals: (1) a term corresponding to double inelastic scattering; (2) a term corresponding to an elastic scatter followed by inelastic scattering, and (3) a term corresponding to an inelastic scattering followed by an elastic scatter.

$$P_2 d\Omega_s dp_s = \int F_1^{INEL-INEL}(p_1, \theta_1, \phi_1) dp_1 d\theta_1 d\phi_1 + \int F_2^{INEL-ELASTIC}(p_s, \theta_1, \phi_1) d\theta_1 d\phi_1 + \int F_3^{ELASTIC-INEL}(p_{INC}, \theta_1, \phi_1) d\theta_1 d\phi_1$$

where the cross sections were multiplied by the correction term

$$\frac{P_1}{P_1 + P_2}$$

The procedure, then, was to fit our cross sections to a general form which was then integrated via a Monte-Carlo routine using the importance sampling technique. This technique gives better accuracy for integrals of functions with a Gaussian behavior. It can be written as

$$\int F(x) dx \approx \sigma \sqrt{2\pi} \sum_{i=1}^N F(\sigma x_i) e^{-x_i^2/2}$$

where x_i are distributed as $e^{-x^2/2}$ and σ is the approximation to the width of the function F .

For the inelastic-inelastic term the integrals had to correctly account for the diffractive behavior of leading particle reactions. For this reason we normalized our high mo-

mentum behavior of the fits to integrals of diffractive scattering cross sections published by Ayres et al.¹⁴

This whole procedure was very costly in terms of computer time. Furthermore, integrable fits were not always obtainable. We therefore computed corrections for only 15 of the 36 possible reaction types. Each of the remaining reaction types had a kinematic behavior similar to one of these 15. Scaling by the ratios of the cross sections then allowed us to obtain the remaining corrections.

These corrections averaged around 1-2% with a few kinematic points having a correction as large as 5-6%. For these worst cases the error was estimated to be less than 1.75%.

6. Radiative Corrections

Our raw cross sections included the effects of photon radiation during the scattering process. Corrections for single photon internal bremsstrahlung have been made to our data using a method based on the equivalent radiator approach, due to J.I. Friedman.¹⁵ Higher order terms were included in an approximate way.

The radiative correction formula can be summarized by:

$$\left. \frac{d^2\sigma}{d\Omega dE'} \right|_{\text{TRUE}}(E_0, E', \theta) = C \left[\left. \frac{d\sigma}{d\Omega dE'} \right|_{\text{MEASURED}} - I_1^A - I_1^B - I_2^A - I_2^B \right]$$

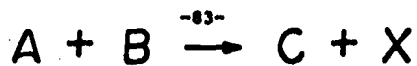
where E_0 is the energy of the incoming particle in the lab, E' is the energy of the detected particle c and θ is the angle at

which c is detected.

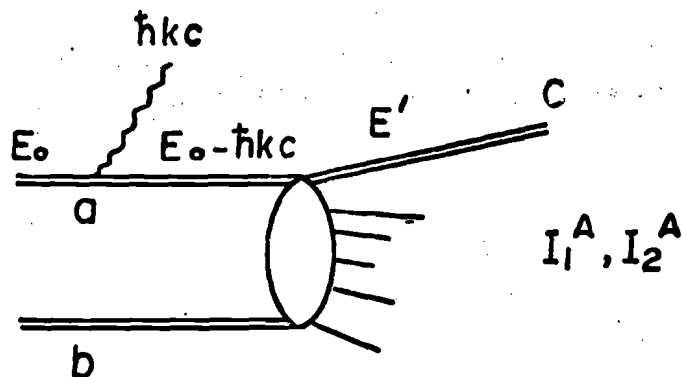
There were only two cases which were considered to be important. These are illustrated in Figure 16. Case A is where the incoming particle emitted a photon of energy $k\epsilon c$ and then scattered from b with an incident energy of only $E_0 - k\epsilon c$. Case B is where the detected particle c , which was created with energy E' , emitted a photon of energy $k\epsilon c$ and was then detected with an energy $E' - k\epsilon c$. The emission of the photon is assumed not to change the direction of the particle, and, hence, all calculations were performed at the scattering angle θ . In either case, the assumed value of $x = \frac{P_C}{P_A}$ is smaller than the actual value.

I_1^A and I_1^B , then, represent the contribution from the elastic scattering process for the two cases. This contribution is non-zero only for the case $a = c$. I_2^A and I_2^B are the sum of the contributions from inelastic scattering at energies from E' to E_0 for the two cases. These four terms represent processes which occurred at higher values of x but were detected in our acceptance. Hence they should be removed from our measured cross sections. However, a fraction of our cross section at this value of x could have also radiated out of our acceptance and the term C corrects for this depletion.

The exact formulas used are listed in the appendix. However, it should be noticed that the integrals in the I_2^A and I_2^B terms involve knowledge of $\left. \frac{d^2\sigma}{d\Omega dE'} \right|_{\text{TRUE}}$. This, then, is an inte-



Case A



Case B

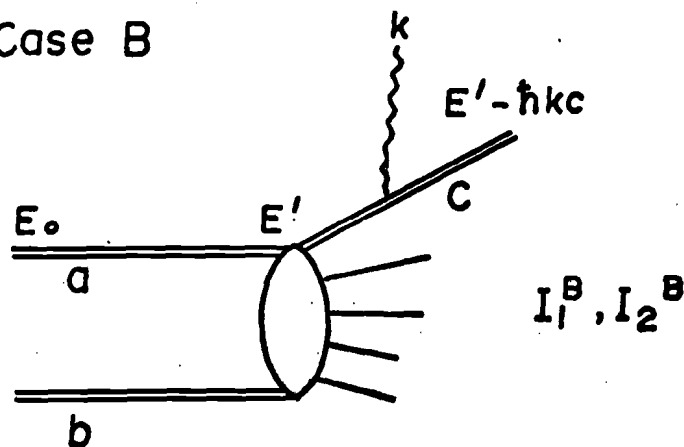


Figure 16 Radiative Processes

-84-

gral equation. The integrals were solved by iteration. The first iteration used the fits determined for the double scattering corrections. The elastic cross sections were taken from fits in Ayres et al.¹⁴ Because the corrections averaged only about 2% with a maximum of 6%, a second iteration was not performed.

As mentioned previously only 15 out of the 36 possible reactions were parameterized by an integral fit function. The other reactions were similar enough in their kinematic dependences to one of these 15, that they could be suitably approximated. However, to reduce our sensitivity to the error introduced by the fit, we set the correction to the ratio:

$$\frac{d^2\sigma}{d\Omega dE'} \Big|_{\text{TRUE}} = \left[\frac{d^2\sigma}{d\Omega dE'} \Big|_{\text{MEASURED}} - I_1^A - I_2^A \right] \times C \times \left[\frac{1 - \frac{I_1^A + I_1^B + I_2^A + I_2^B}{\frac{d^2\sigma}{d\Omega dE'}(E_0, E', \theta) \Big|_{\text{FIT}}}}{1 - \frac{I_1^A + I_1^B}{\frac{d^2\sigma}{d\Omega dE'}(E_0, E', \theta) \Big|_{\text{FIT}}}} \right]$$

This reduced to the first equation when $\frac{d^2\sigma}{d\Omega dE'} \Big|_{\text{FIT}}$

$= \frac{d^2\sigma}{d\Omega dE'} \Big|_{\text{MEASURED}}$. We estimate the error in this procedure to

be a maximum of 1.25% in the cross section.

7. Other Systematic Uncertainties

In addition to the corrections discussed a number of other sources of error were possible. The beam occasionally delivered more than one particle with a 1 to 2 nanosecond time difference. The trigger counters were not able to resolve the second and succeeding particles. Thus, we would underestimate the flux. However, assuming the momenta of these particles were uncorrelated, the event would likely be rejected because of an ambiguous track in the momentum hodoscope. Furthermore, the tight beam particle identification requirements would reject the two particles if they were of different types. For an estimated worst case of 7% doubles rate in the beam, the worst contamination of the cross sections would be 1.2% for pions at negative beam energies (where pions comprised 92% of the beam). The contamination would be smaller, by the fraction of the beam population, for other particle types.

Electrons and muons were present in the beam and would give a pion signal in the Cerenkov counters. Since they do not interact strongly, they would cause an overestimate of the flux. Estimates of the contamination of the pion-induced cross sections from online studies, were on the order of 0.5%. One should note that slow leptons would be swept out of the beam by the AVB magnets before making a trigger.

Various electronic inefficiencies and other small effects were estimated to add 0.5% to the systematic uncertainty. Table

III lists the errors and their sources for a given point.

There was in addition an overall normalization uncertainty. The values used for the solid angle and momentum acceptance were those predicted by the program TRANSPORT. The values of the coefficients which described the transport of particles from the hydrogen target to the parallel region in the spectrometer were checked online. The measured values differed from the predictions by 6.3%. The coefficients which determined the acceptance included not only these measured values, but also the values which described the transport of particles from the parallel region to the spectrometer focus. We were unable to check these values. These acceptance numbers determined the normalization of the cross sections. We have, therefore, conservatively assigned a normalization uncertainty, for the cross sections, of 7%.

Table III: Systematic Uncertainties

		Error on Cross Section (%)
1. Transmission	x	0.3
	k	1.0
	P	0.3
2. Absorption		0.5
3. Decay	π	0.1
	k	1.0
4. Particle Identification Spectrometer		0.6
	Beam	0.1
5. Multiple Scattering- Function of Spectrometer Momentum		4.0 - 0.5
6. Tracking Loss- Function of Spectrometer Momentum		0.5 - 0.75
7. Double Scattering		1.8
8. Radiative Corrections		1.3
9. Electron and Muon Contamination		0.5
10. Double Buckets- Function of Beam Energy	π	.3 - 1.2
	k	.1 - .5
	p	.1 - .9
11. Miscellaneous Sources		0.5
12. Normalization - Acceptance		7.0

IV. RESULTS AND INTERPRETATION

A. Final Cross Section

Our final cross sections were available on the disk as both p_T sweeps or as $x = p_C/p_A$ sweeps. We have plotted the data in both variables as discussed below. Because of the enormous quantity of data, only a subset of our data will be presented. However all our data will be published in a future journal article.

A number of checks were applied to our data to check for internal consistency. First, data with the 10" hydrogen target were compared to those with the 20" hydrogen target. The agreement was within statistical errors. This assured us that there were no target length effects present. Only the 20" data will be considered further. Next, runs which taken with the multiplicity Cerenkov counter removed, were compared with those in which it was present. There was a danger that the dummy target subtraction would not fully remove the excess events originating in the counter. The agreement was generally within our errors.

A number of data points in our proton cross sections were then compared with the data of Johnson, *et al.*¹, and our $p + p + \pi^+ + X$ data were compared to the data of Capiluppi, *et al.*² Our data agree with these results within the 7% normalization uncertainties.

1. p_T Dependence

A subset of our cross sections have been plotted in Figure 17 as a function of the transverse momentum, p_T , for $x = p_C^{lab}/p_A^{lab} = 0.3$ and 0.6 . Additional plots may be found in the appendix of this thesis. The cross sections are generally fit well with an exponential p_T dependence at $x = 0.6$ and with a Gaussian form at $x = 0.3$. These functions were used to integrate the cross sections as described later.

The crossover from a Gaussian behavior to an exponential occurs at an x value which seems to depend on the particular reaction. However, there are very few x values with extensive p_T coverage, which makes these crossover points difficult to determine accurately.

2. x Dependence

A subset of our cross sections has been plotted in Figure 18, as a function of the radial scaling variable, x_R , for fixed values of p_T . This scaling variable is defined as

$$x_R = \frac{E_C^{CM}}{E_{MAX}^{CM}}$$

and has been shown by Taylor, et al.¹⁶ to produce scaling over a wider range of energies than the usual Feynman x_F .

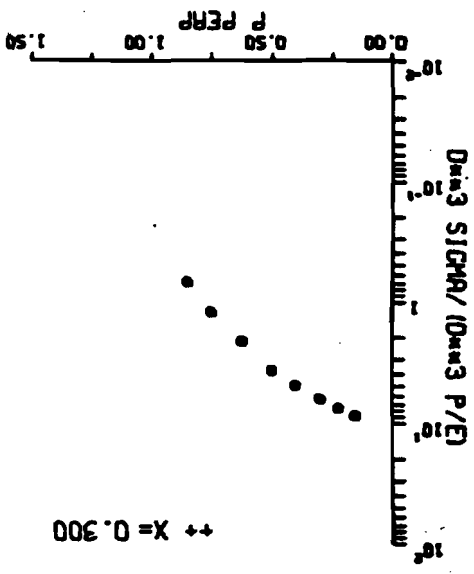
$$x_F = \frac{p_{C\parallel}^{CM}}{p_{MAX}^{CM}} \approx \frac{2p_{C\parallel}^{CM}}{\sqrt{s}}$$

Scaling is discussed in section B. Over our kinematic range the values of $x = p_C^{lab}/p_A^{lab}$, x_F and x_R are all approximately

Figure 17. This figure contains plots of invariant differential cross sections as a function of p_T for values of $x=0.3$ and 0.6 . The symbols denote

- * unaveraged cross sections (data taken at only one sign of the AVB angle)
- o averaged cross sections (data taken at both signs of the AVB angle)

The units are nb/GeV^2 .



P1.P1 PBARM=175

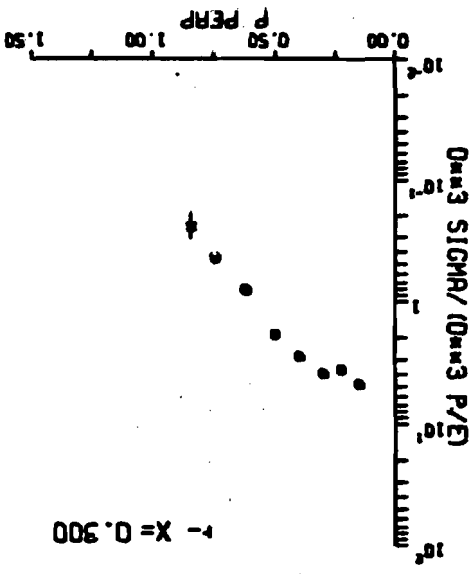
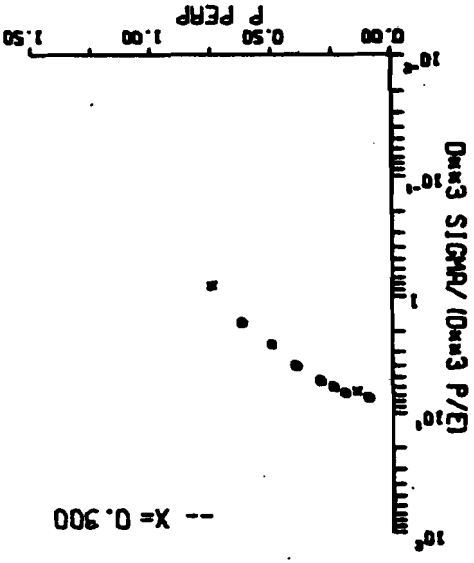


Figure 17b

-22-



P1.P1 PBARM=-100

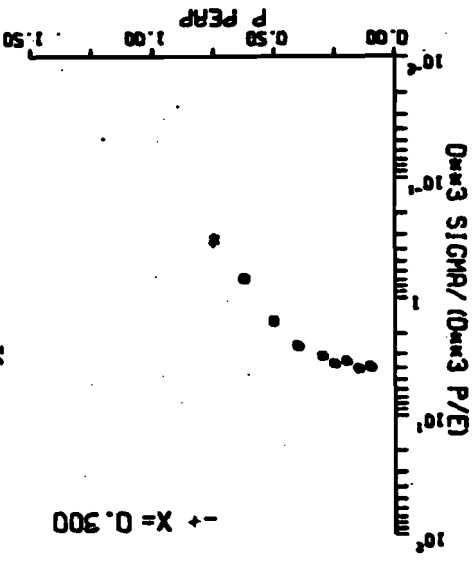
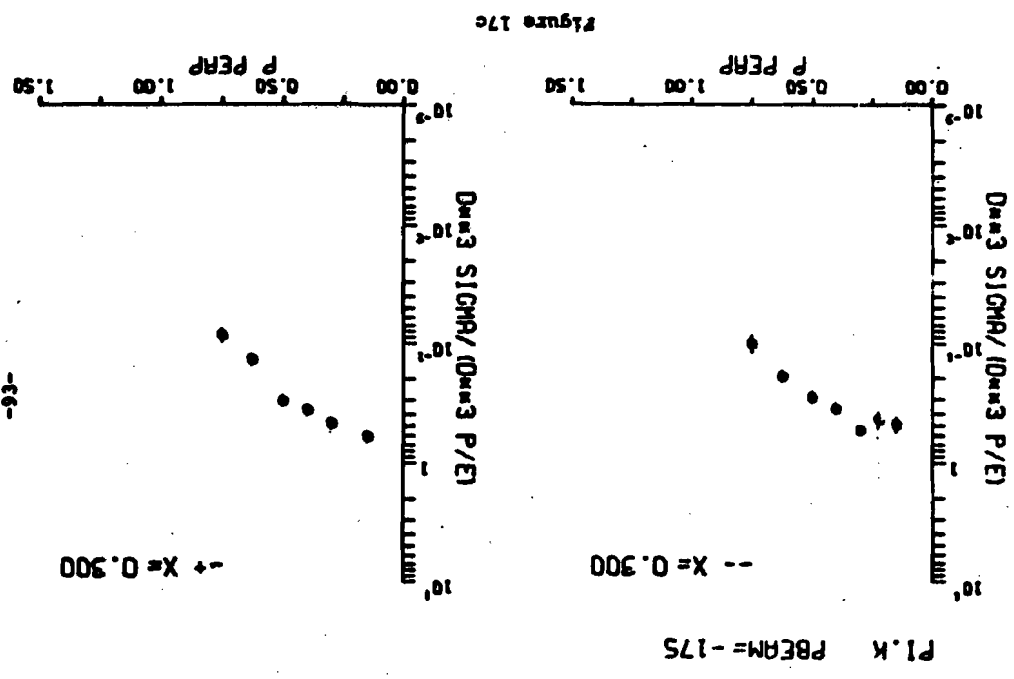
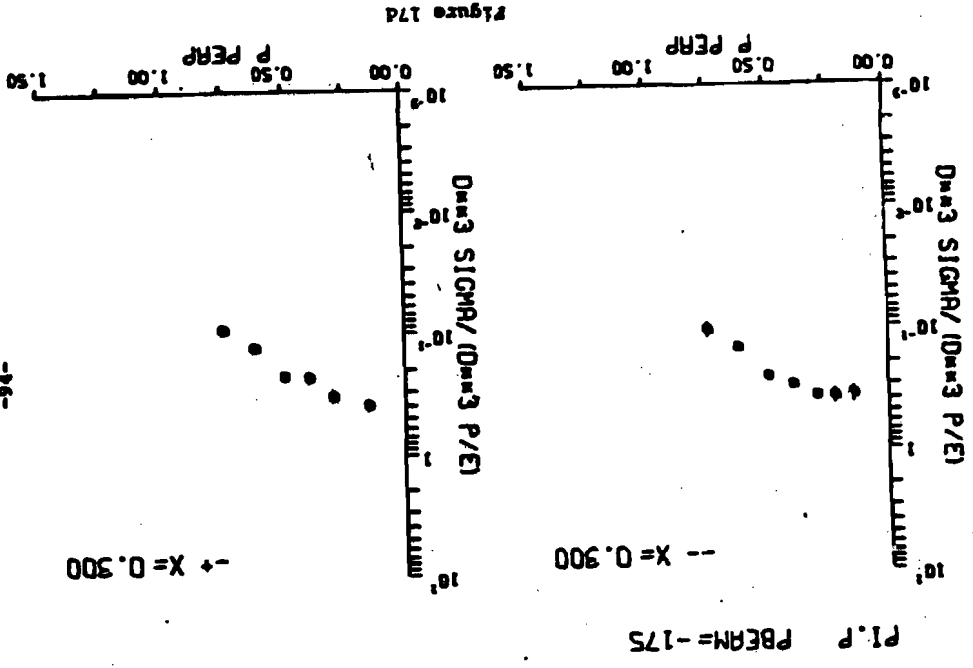
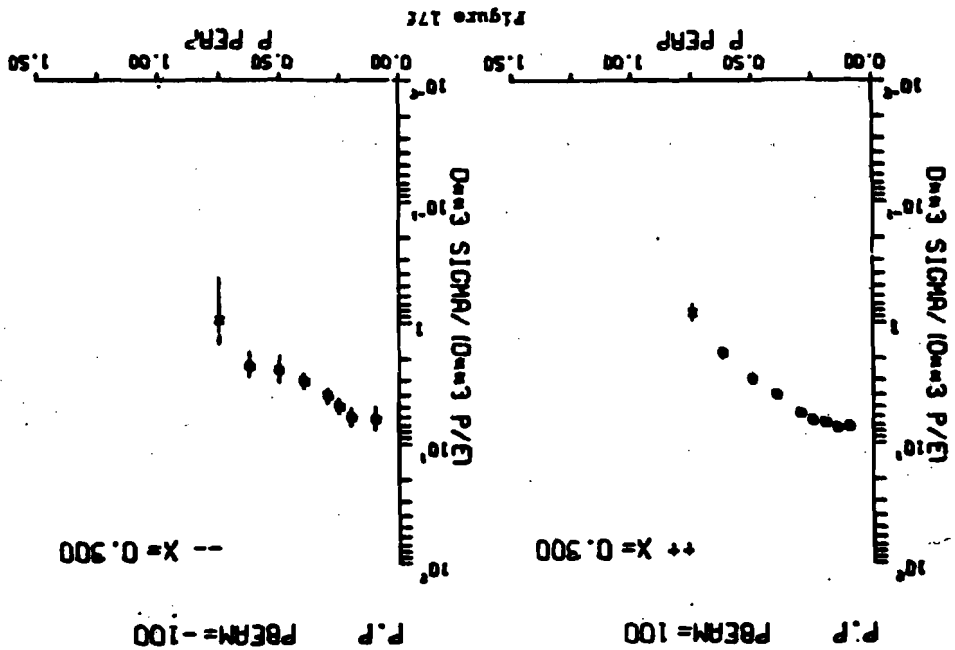


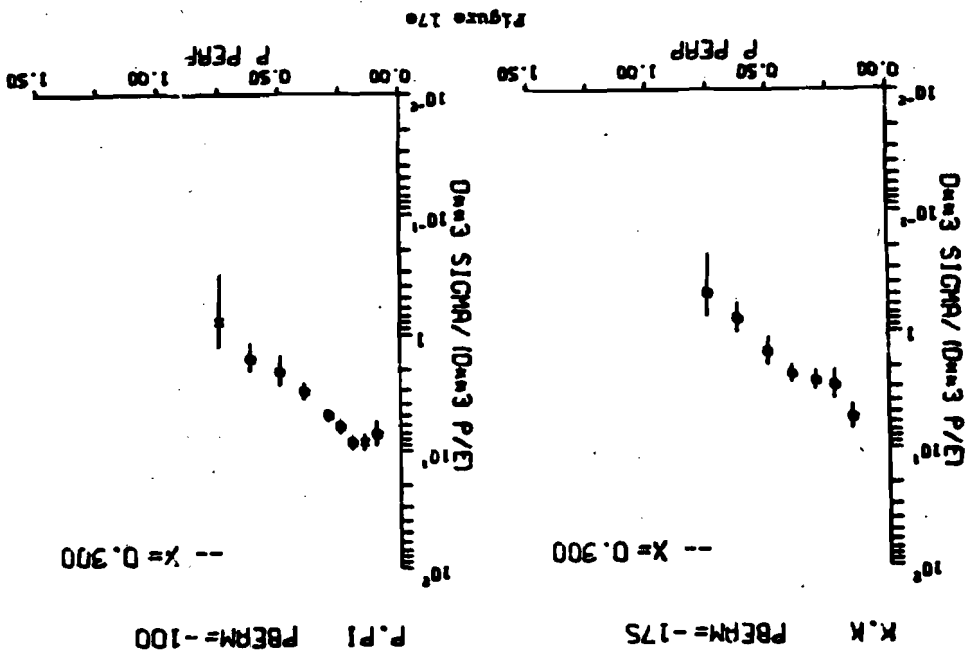
Figure 17a

-16-

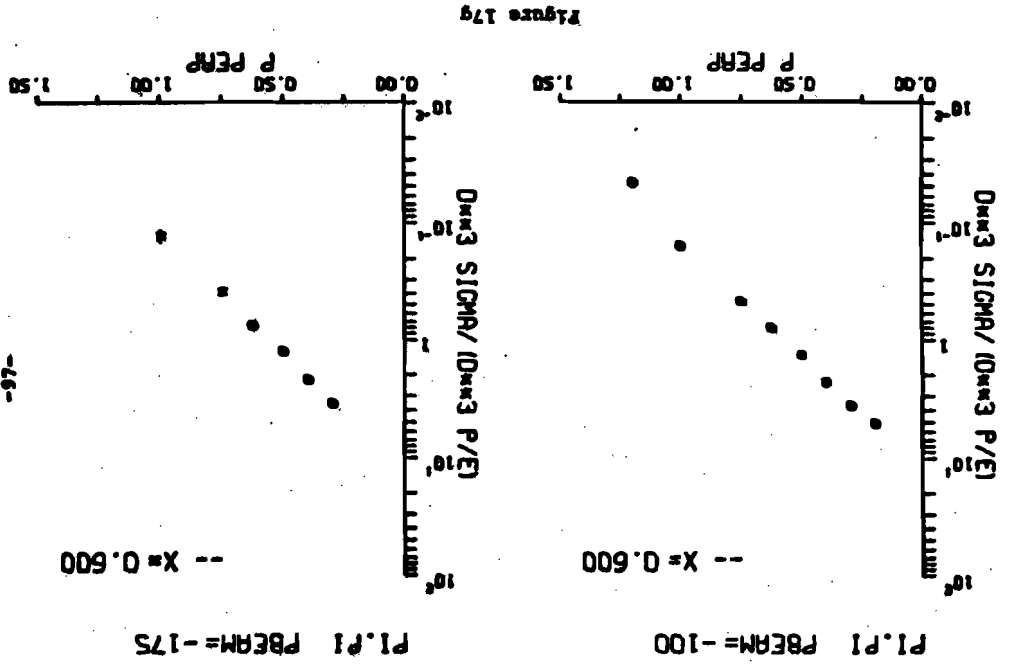
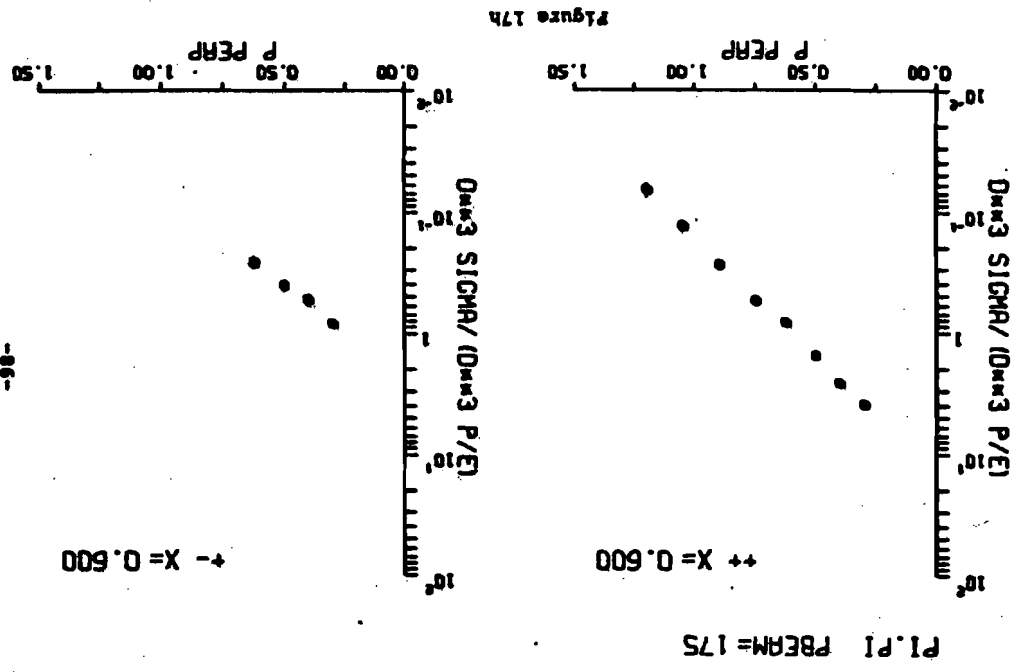


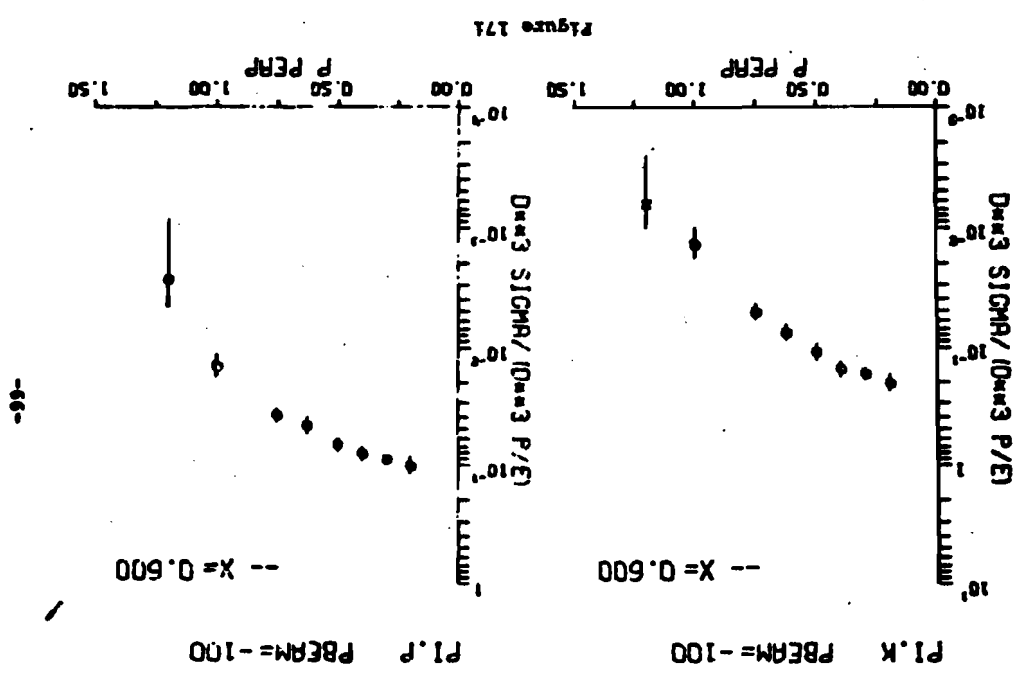
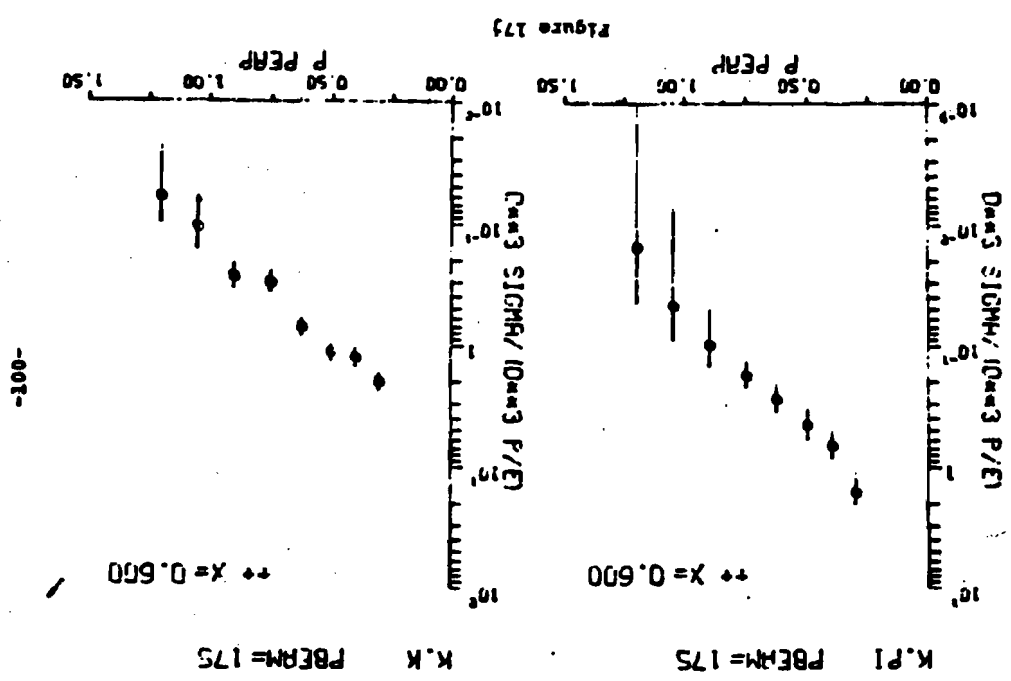


-96-



-56-





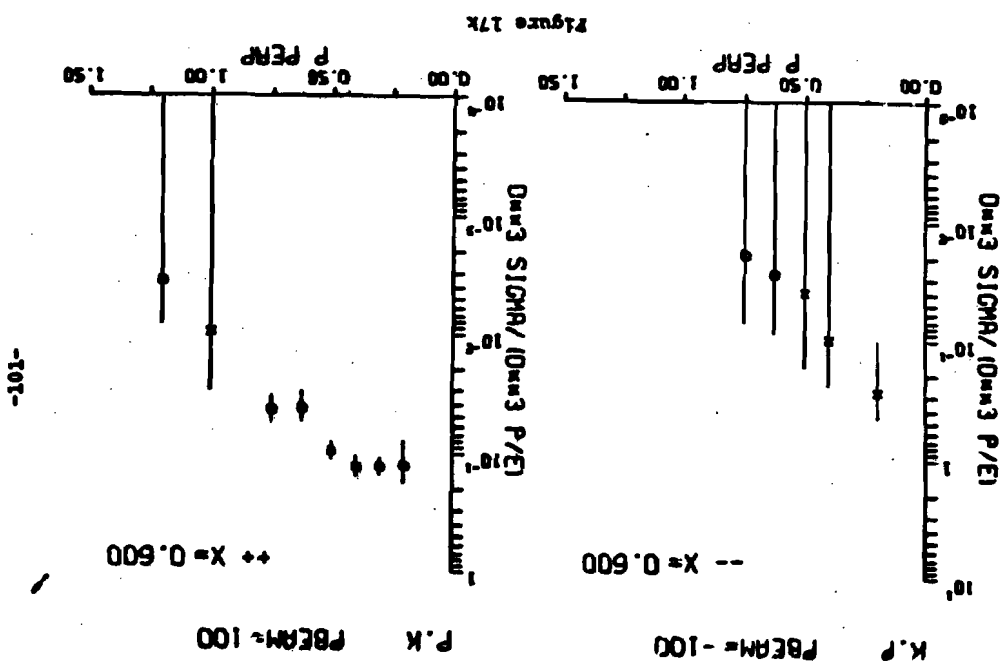
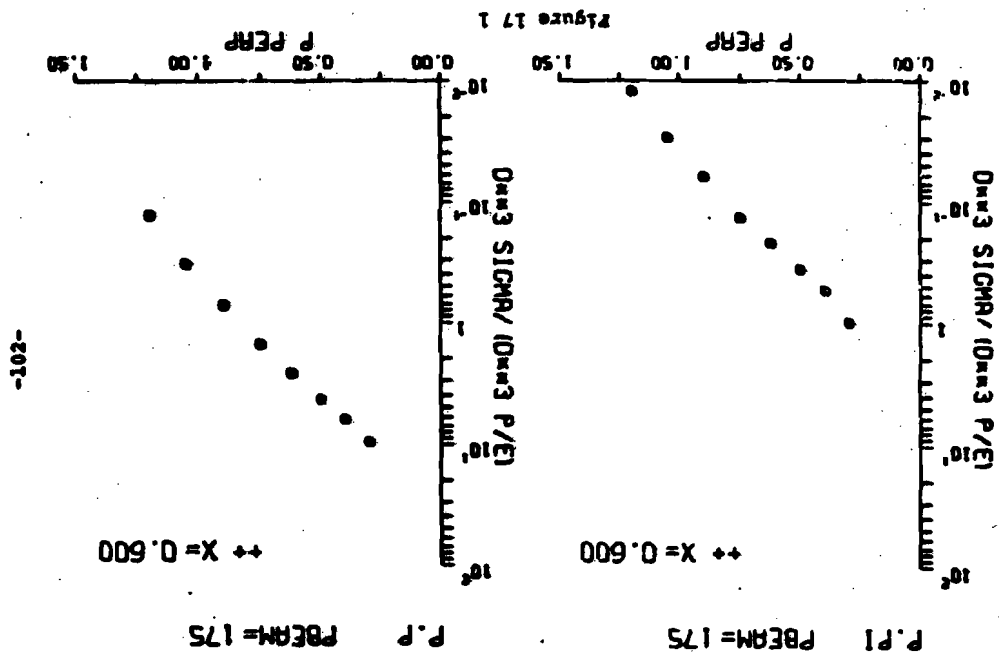


Figure 18. This figure contains plots of invariant differential cross sections as a function of x_p for values of $p_T = 0.3$ and 0.5 GeV/c. The symbols denote

- x unaveraged cross sections (data taken at only one sign of the AVB angle)
- o averaged cross sections (data taken at both signs of the AVB angle)

The units are mb/GeV².

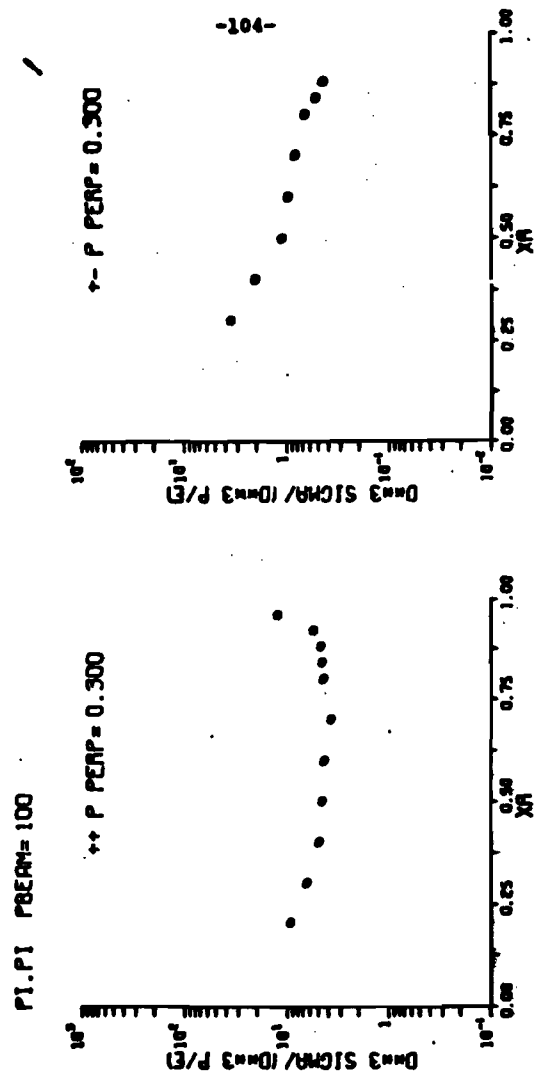
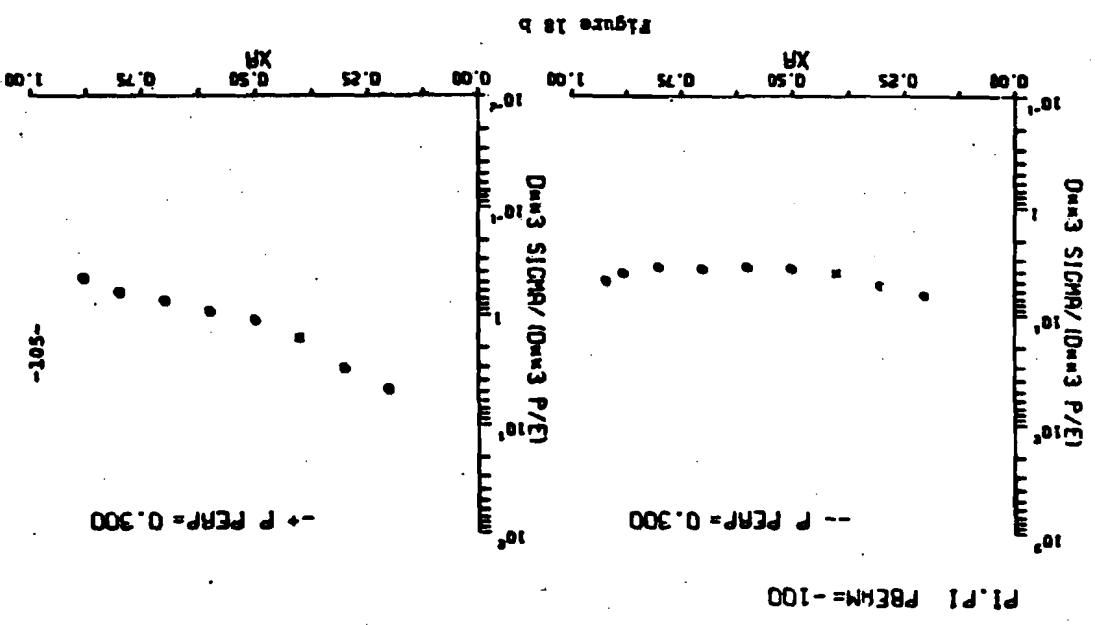
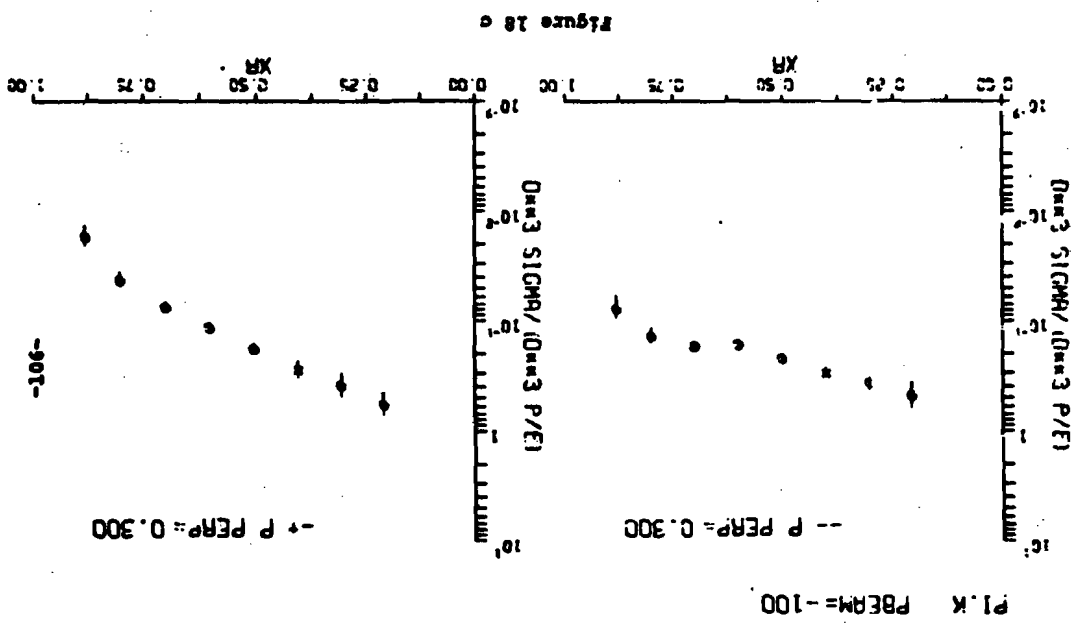
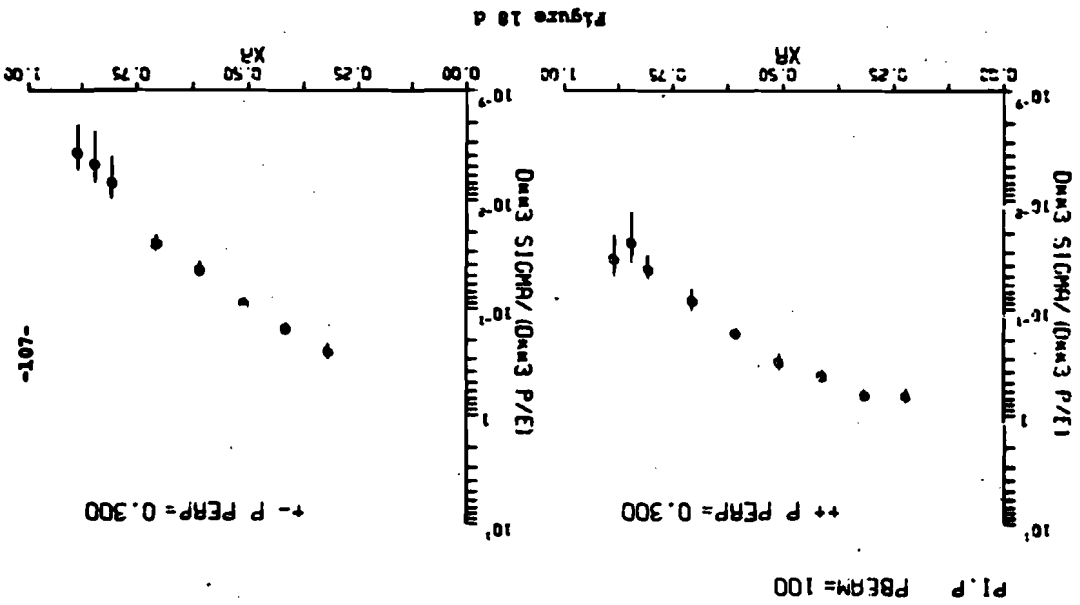
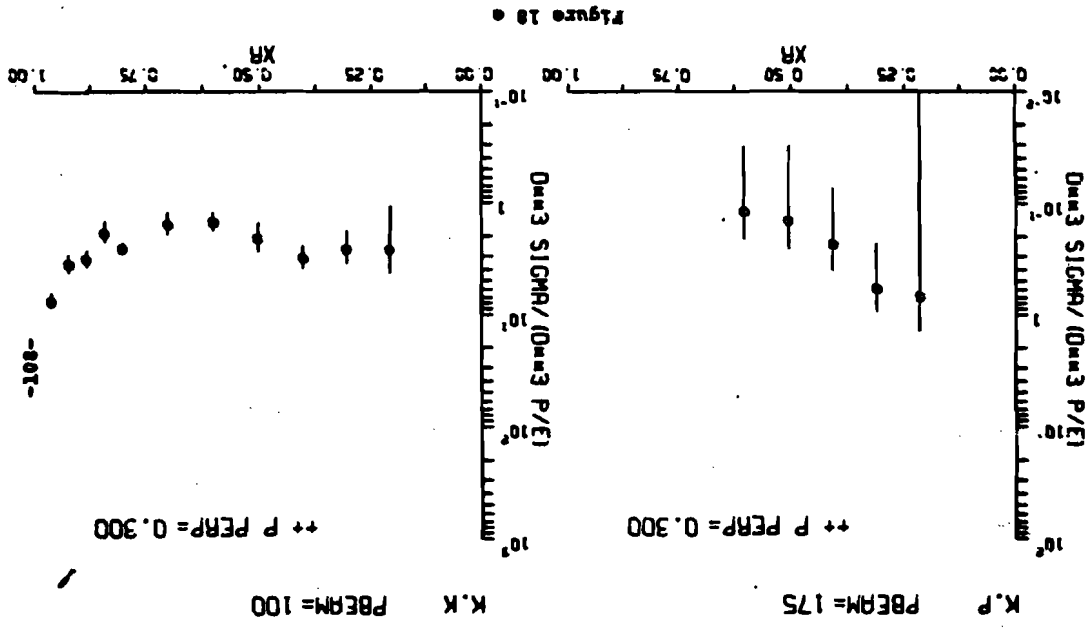
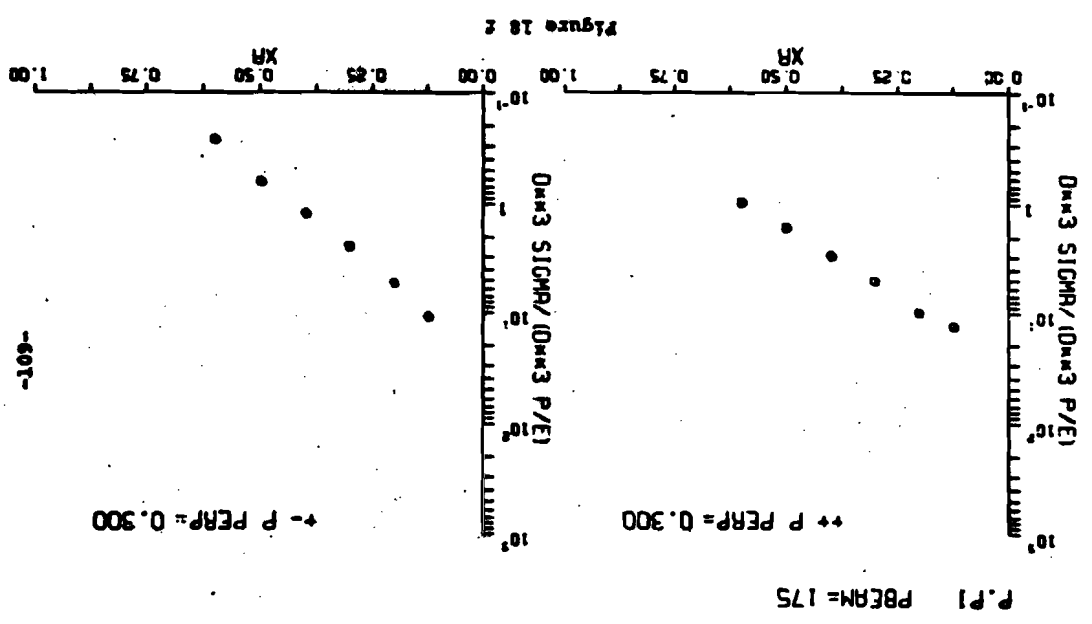
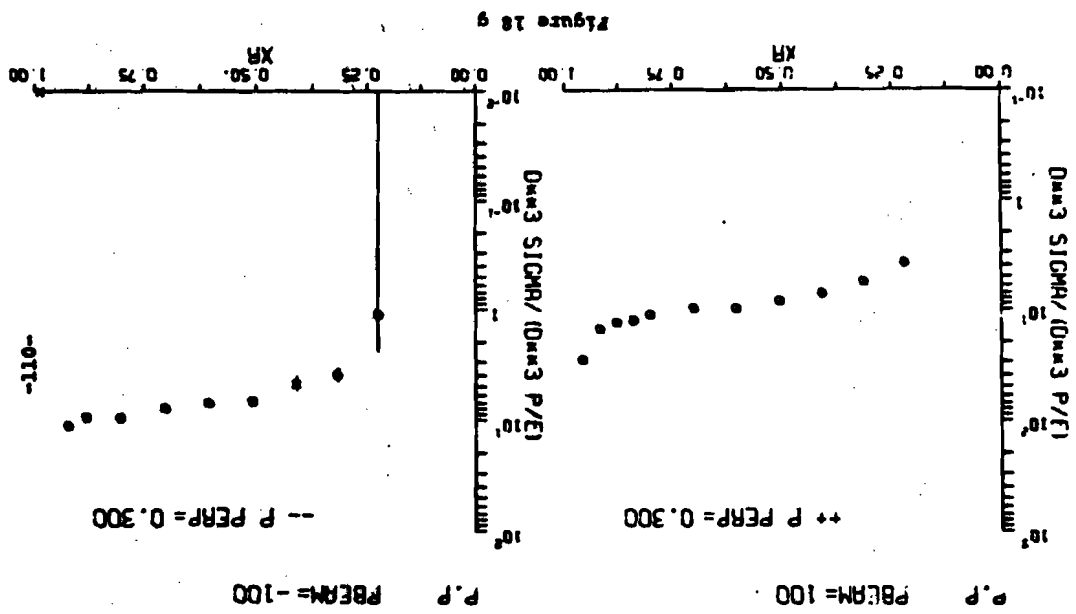
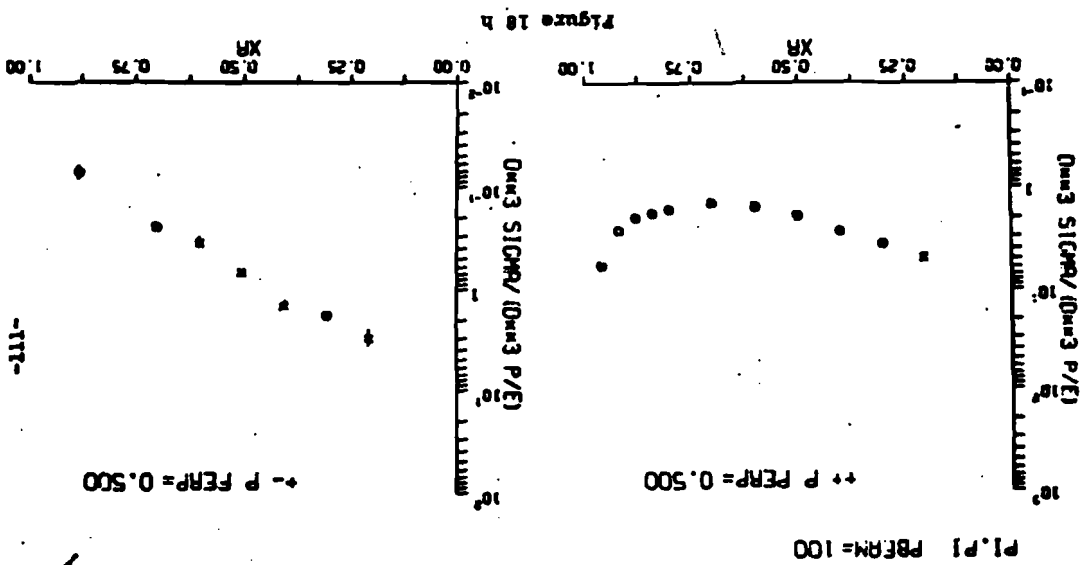
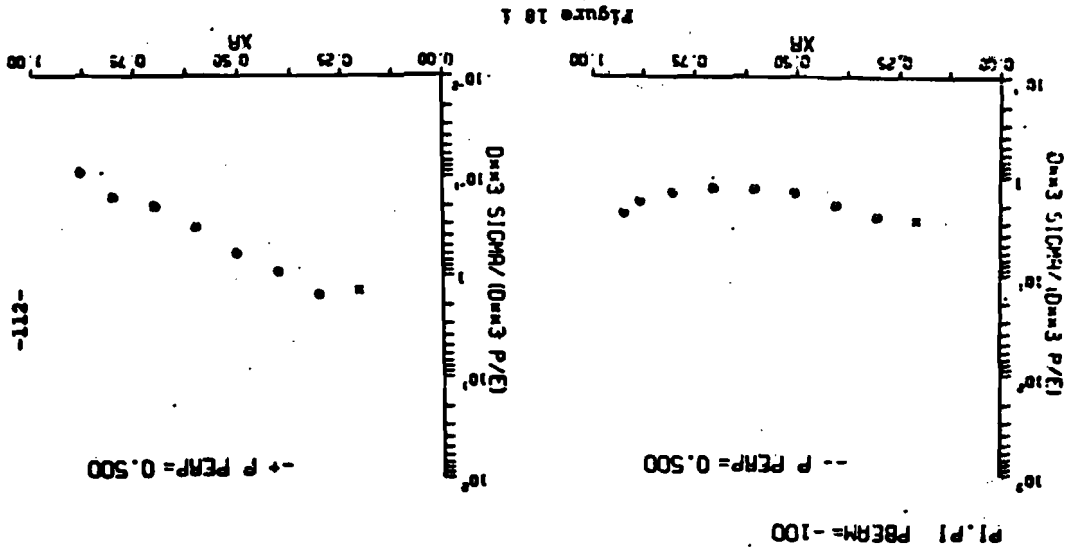


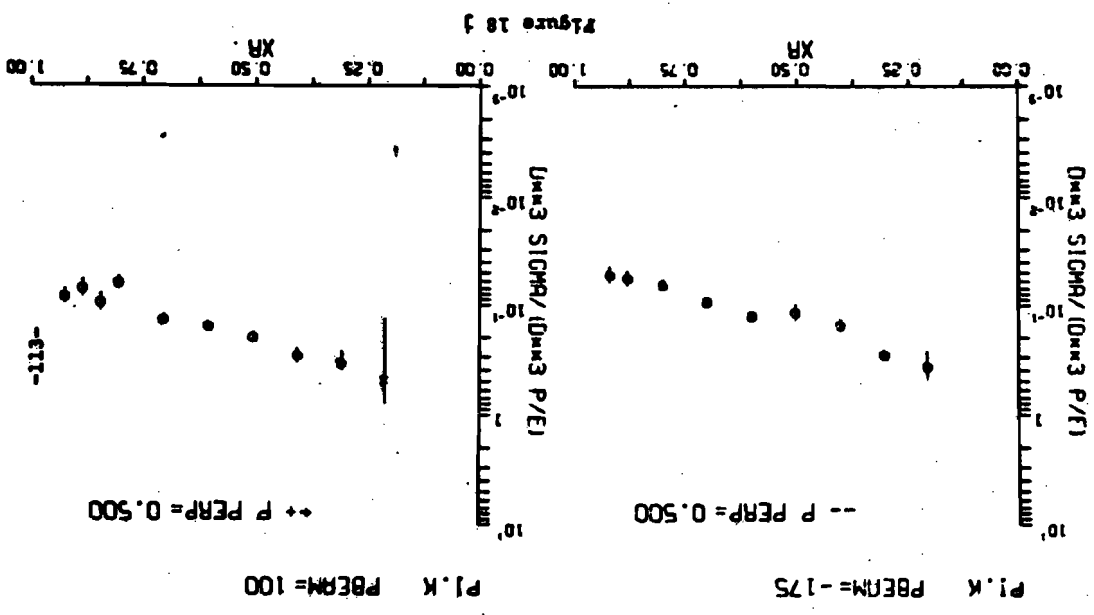
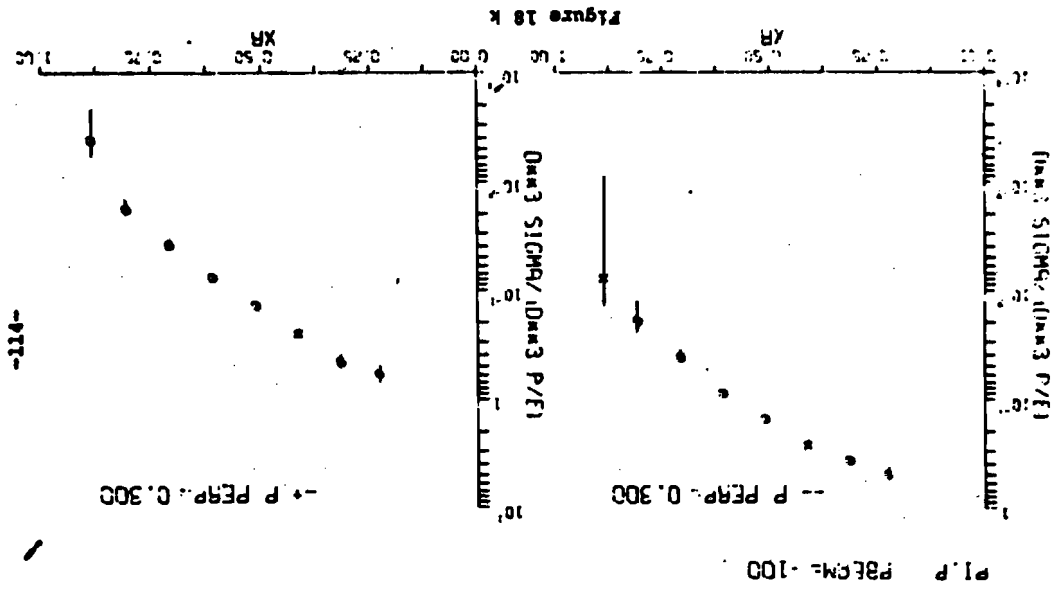
Figure 18 a

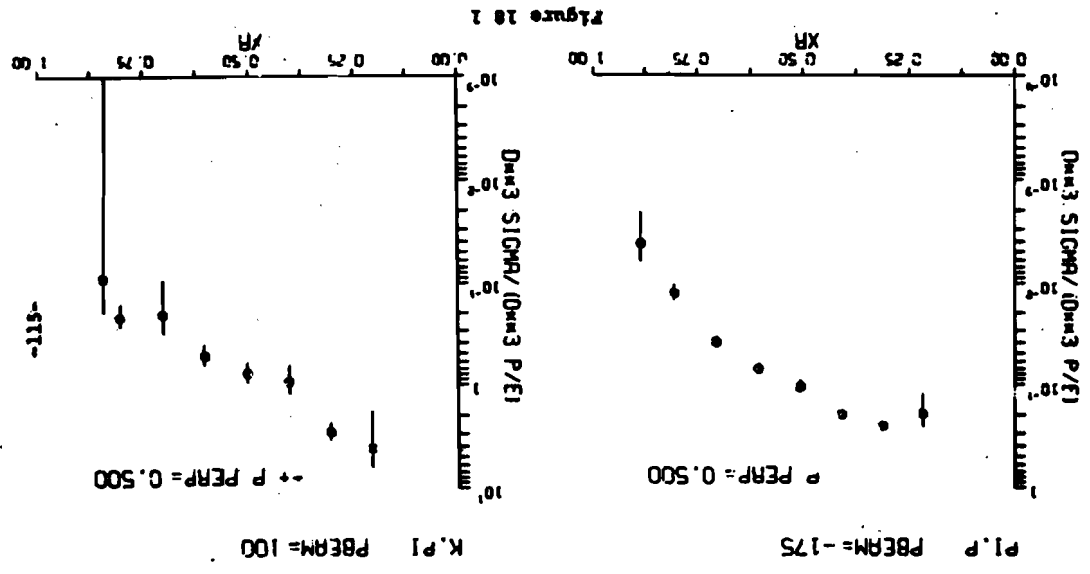
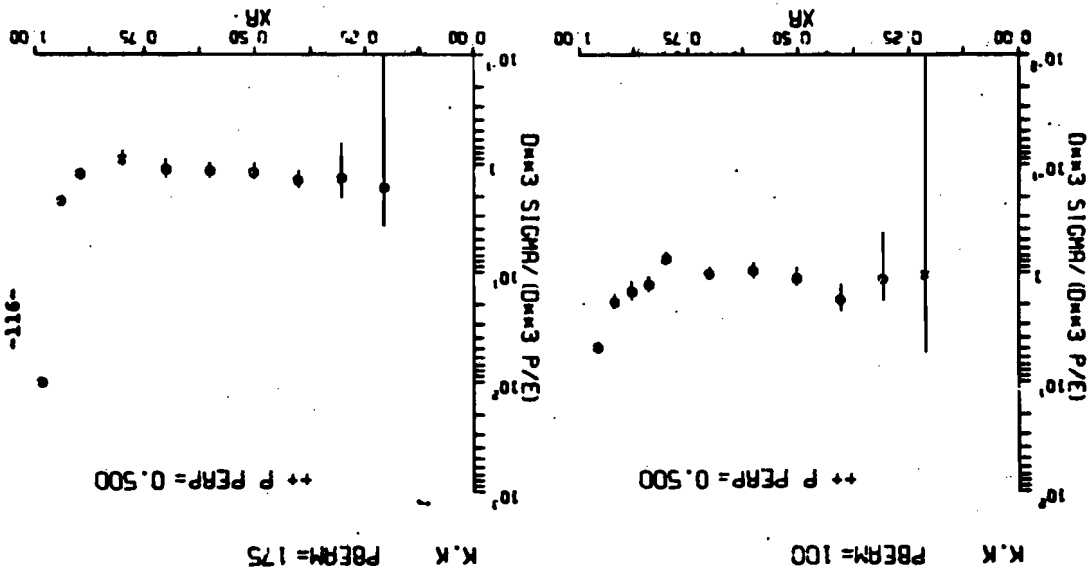


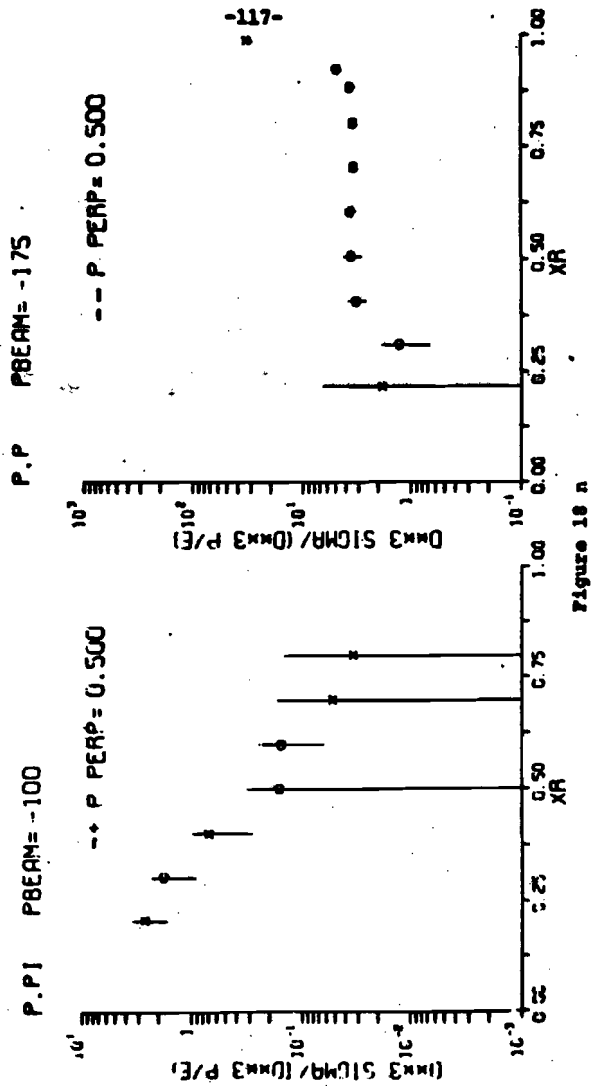












equal. Additional plots of the x_R dependences will be found in the appendix.

The x_R behavior remains essentially unchanged over the p_T range in which we have data. This is discussed further in a later section. The exceptions are cases in which we see resonance production, as in the reactions $\pi^+ + p \rightarrow \pi^- + X$. Here the p_T dependence of the resonance falls faster than the fragmentation part of the cross section. An analysis of this particular resonance behavior is found in Cutts, *et al.*¹⁷

3. x Dependence of Cross Sections Integrated Over p_T

Some of the models we tested made predictions for cross sections integrated over p_T . To obtain these cross sections we fitted the p_T dependence of our data to both an exponential and a Gaussian form in p_T . The form we actually integrated was chosen generally on the basis of the minimum χ^2 per degree of freedom. The integrals were performed analytically.

These integrated forms have x dependences similar to the unintegrated, p_T constant, cross sections. Some of these are plotted in Figure 19. These x dependences will be discussed further in the following sections. Because of the lack of sufficient x values with sufficient coverage of p_T to do an integration, we have used the unintegrated data for testing models in a number of cases where the absolute normalization was unimportant.

These cross sections have larger error bars than the un-

Figure 19. The invariant cross section, $\int \frac{E_c^{c.m.}}{\pi p_{T,c.m.}^2} \frac{d^3\sigma}{dp_T^2 dx} dp_T^2$, in units of mb and denoted by "s" is plotted as a function of x. In plots i through i, comparison is made with the invariant differential cross section, $E_c \frac{d^2\sigma}{dp_T^2 dx}$, in units of mb/GeV², measured at +100 GeV, p_T=0.5 GeV/c and denoted by "x".

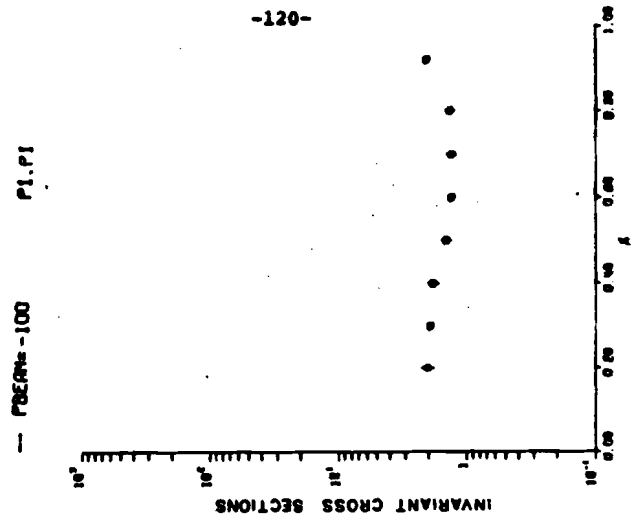


Figure 19 b

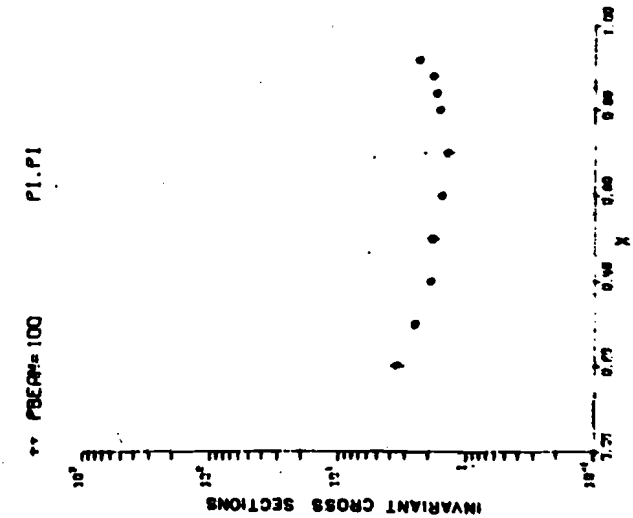
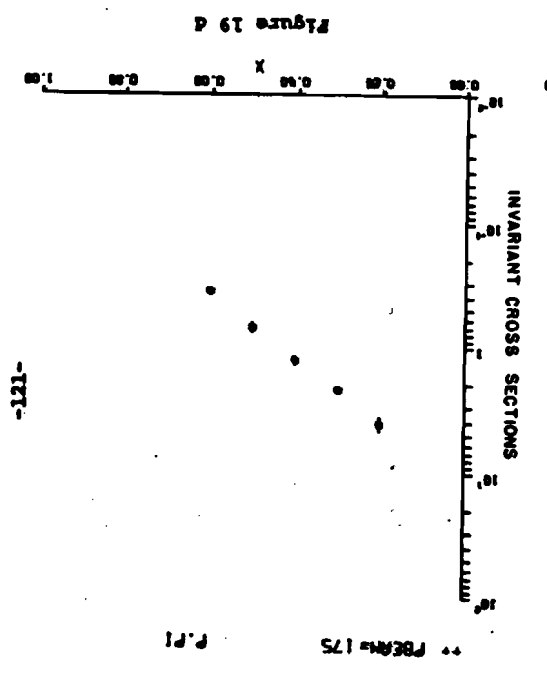
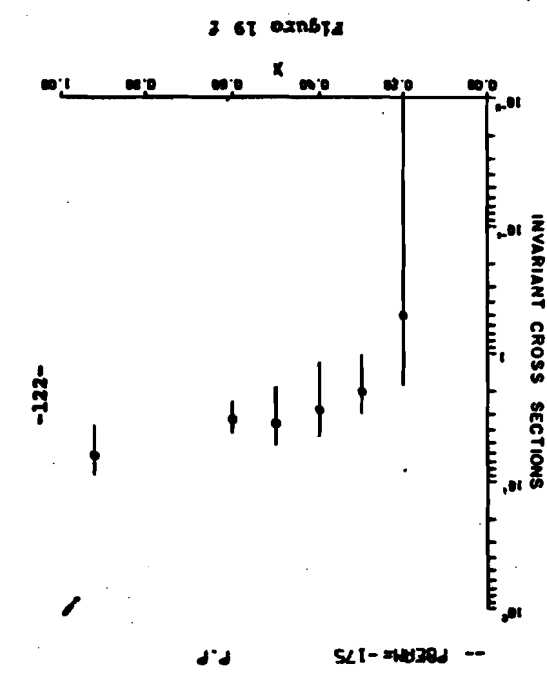
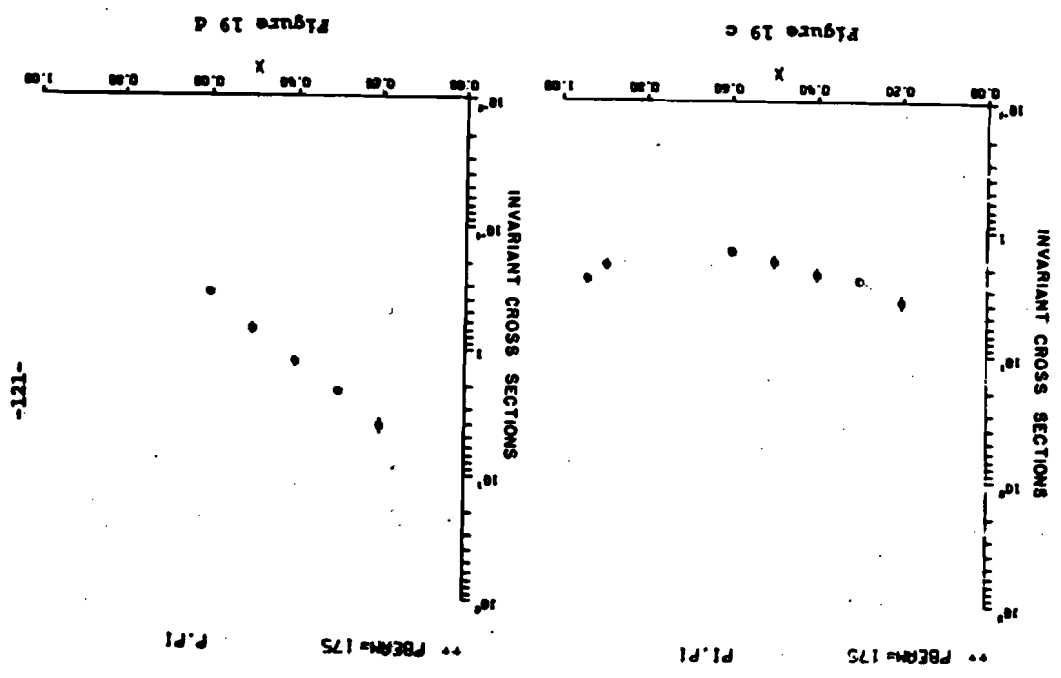
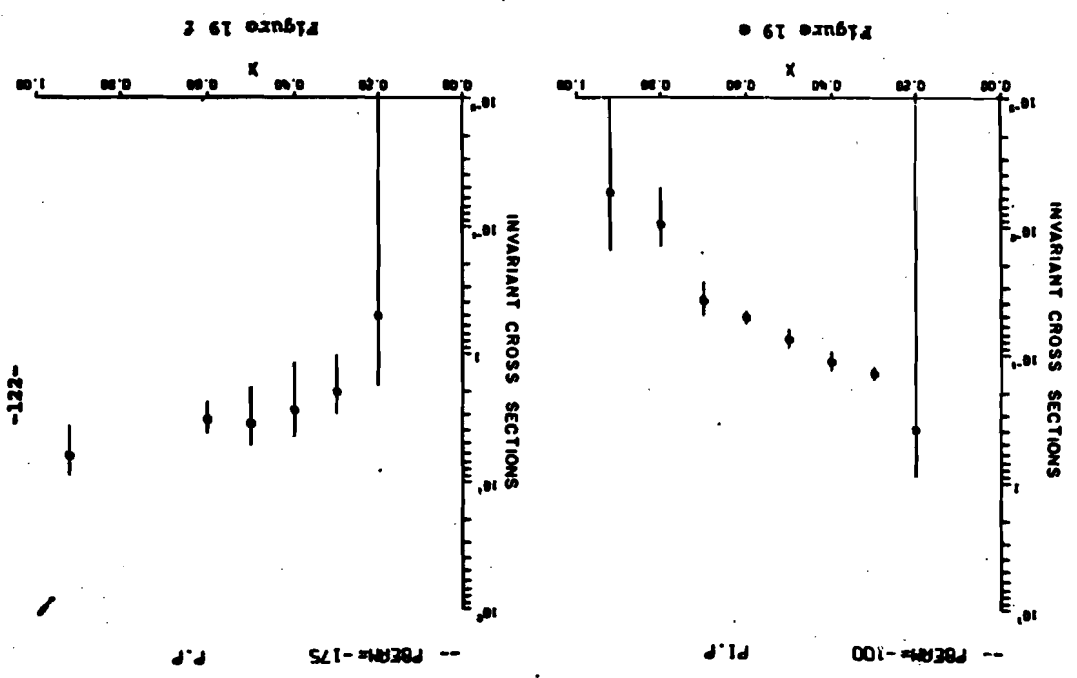
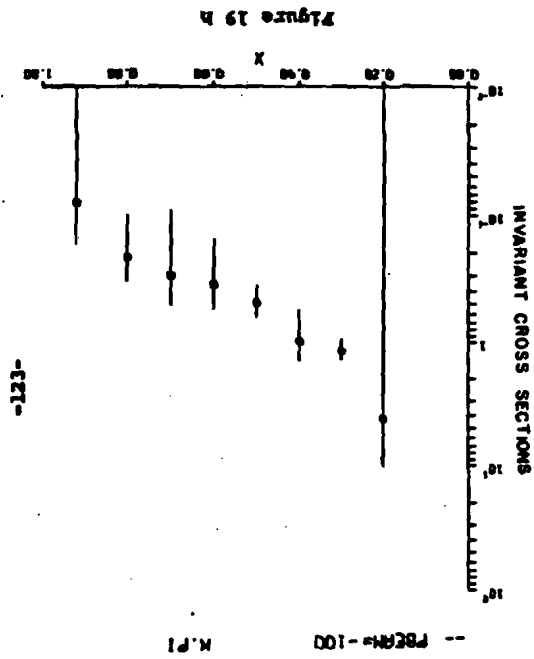
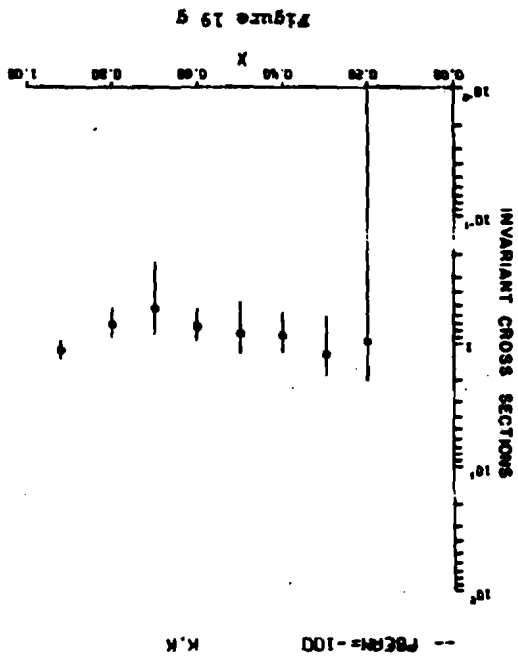
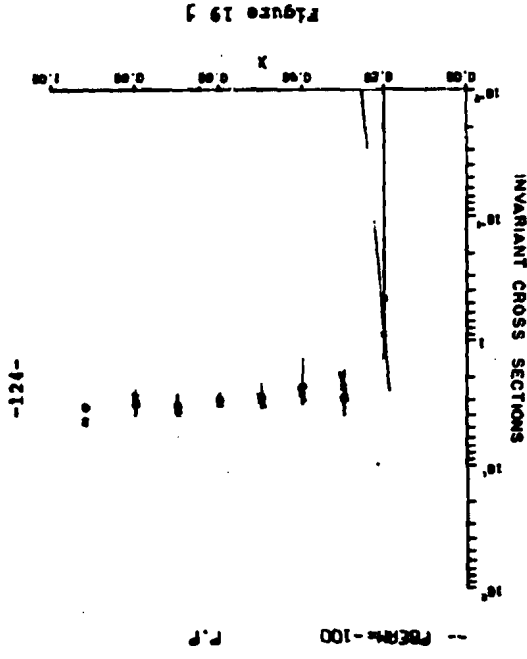
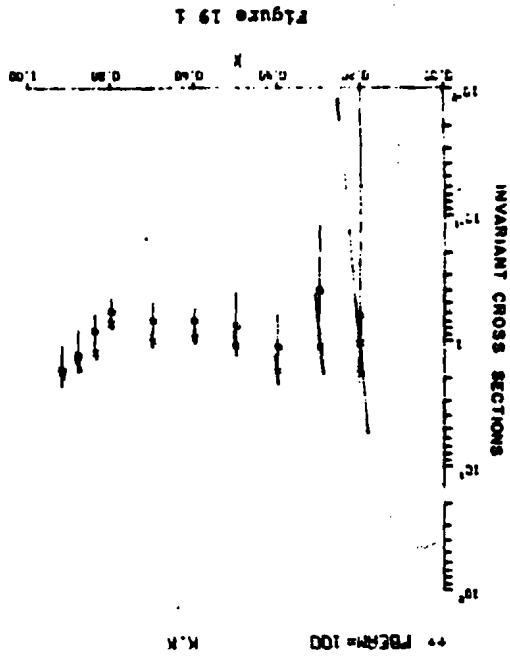
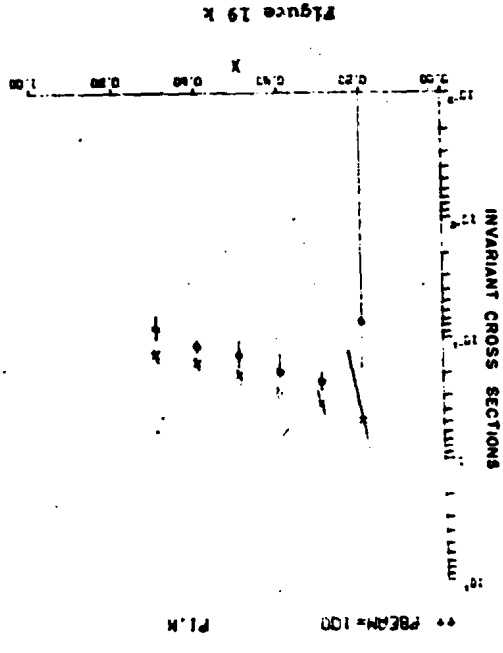
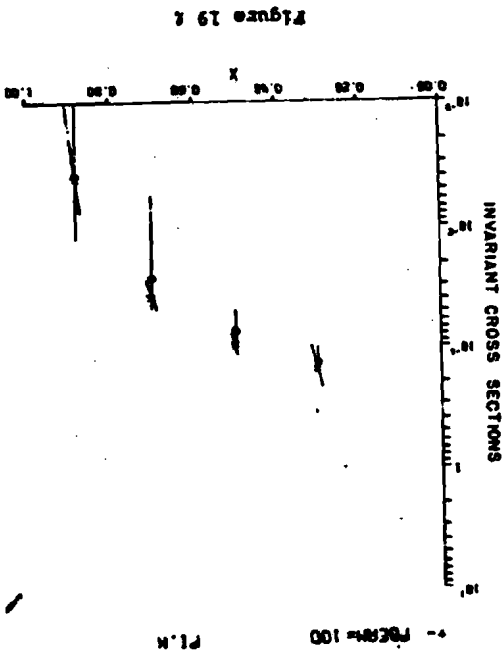


Figure 19 a





integrated cross sections. This can be seen in Figures 19 i-i where we have plotted unintegrated cross sections at $P_A = 0.5$ on the same graphs as our integrated values. The reason for this is that a small error in the determination of an exponential term can lead to a large error in its integral out to infinity.



B. Scaling

One property of high energy inclusive cross sections, which had been predicted by Feynman¹⁸ and Yang, et al.¹⁹, is known as scaling. We have defined the Lorentz invariant cross section as

$$f(s, \vec{p}_c) = E_c \frac{d^3\sigma}{d^3p_c}$$

For unpolarized experiments we can replace \vec{p} with p_{1c} and p_{2c} .

Thus we can write

$$f(s, p_{1c}, p_{2c}) = \frac{E_c}{\pi} \frac{d^3\sigma}{dp_{1c}^2 dp_{2c}}$$

In the center of mass frame we can define

$$x = \frac{p_c^{CM}}{p_{MAX}^{CM}}$$

and rewrite the cross section as

$$f(s, p_{1c}, x) = \frac{E_c^{c.m.}}{\pi p_{MAX}^{c.m.}} \frac{d^3\sigma}{dp_{1c}^2 dx}$$

The scaling hypothesis is the statement

$$f(s, p_{1c}, x) = f(p_{1c}, x).$$

That is, f is independent of s when written as a function of x and p_{1c} .

In Figures 20 and 21 we have plotted on the same graph our cross sections for incident energies of 175 and 100 GeV, corresponding to s values of 187.7 and 378.4 GeV². As can be seen

Figure 20. Scaling Comparisons as a Function of P_T .
The units are mb/GeV².

- o - Cross sections at $s=187.7$ GeV²
- x - Cross sections at $s=378.4$ GeV²

-130-
P.P1 PBERN=100 175
** X=0.300

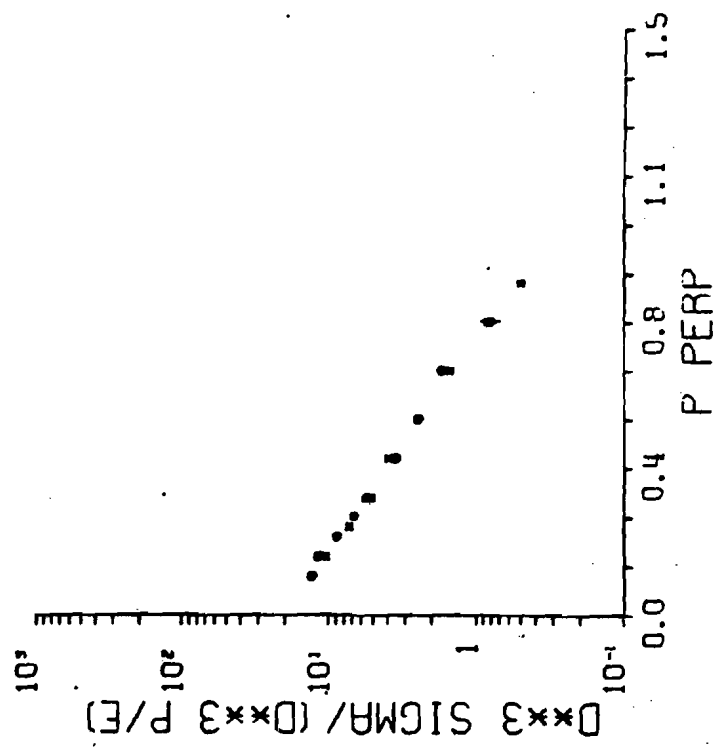


Figure 20 b

-129-
P1.P1 PBERN=100 175
** X=0.500

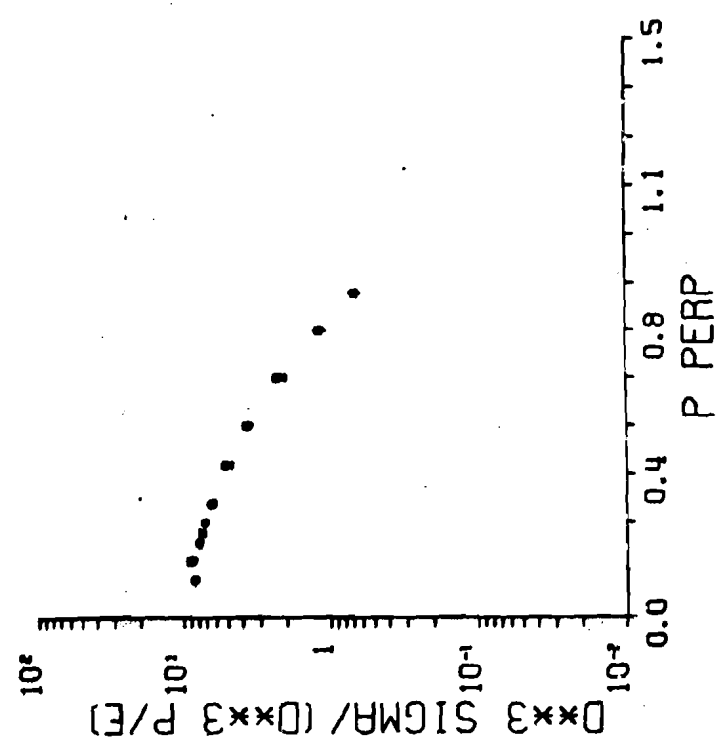


Figure 20 a

PI.P1 PBEAM=100 175
** X=0.600

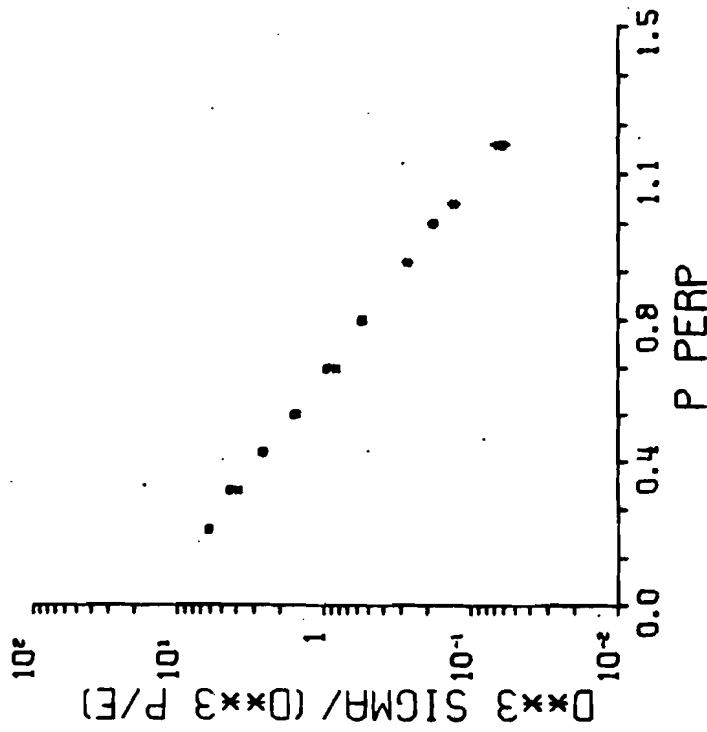


Figure 20 c

K.K PBEAM=100 175
** X=0.600

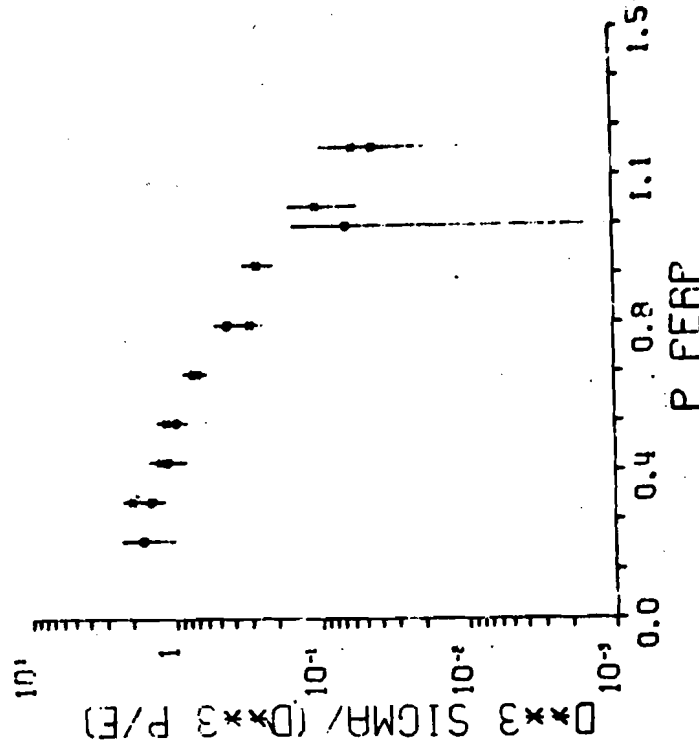


Figure 20 d

P.P1 PBEAM=100 175
** X=0.500

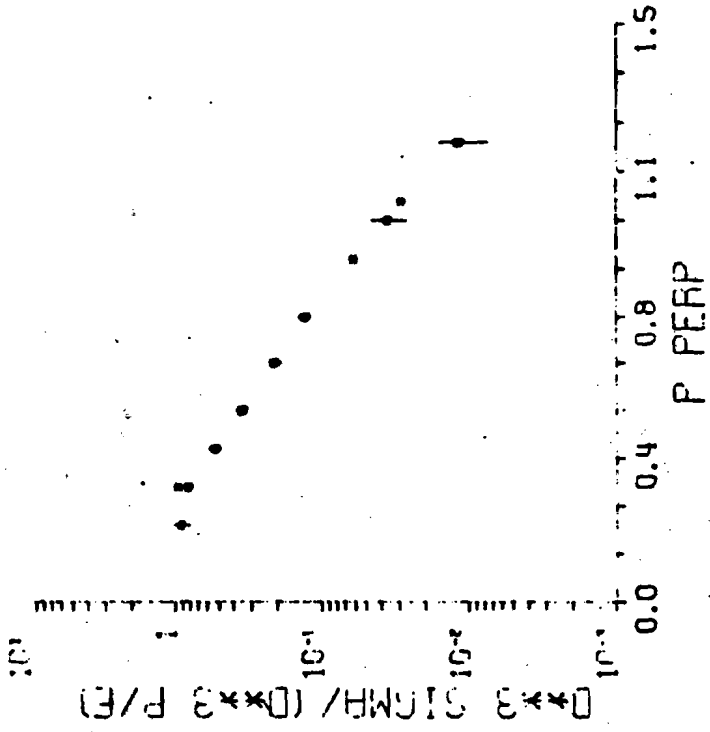


Figure 20

Figure 21. Scaling Comparisons as a Function of x_2 .
 The units are mb/GeV².
 o - Cross sections at $\sqrt{s}=187.7 \text{ GeV}^2$
 x - Cross sections at $\sqrt{s}=378.4 \text{ GeV}^2$

-135-

P1.P1 PBEAM=100 175
** P PEAP=0.300

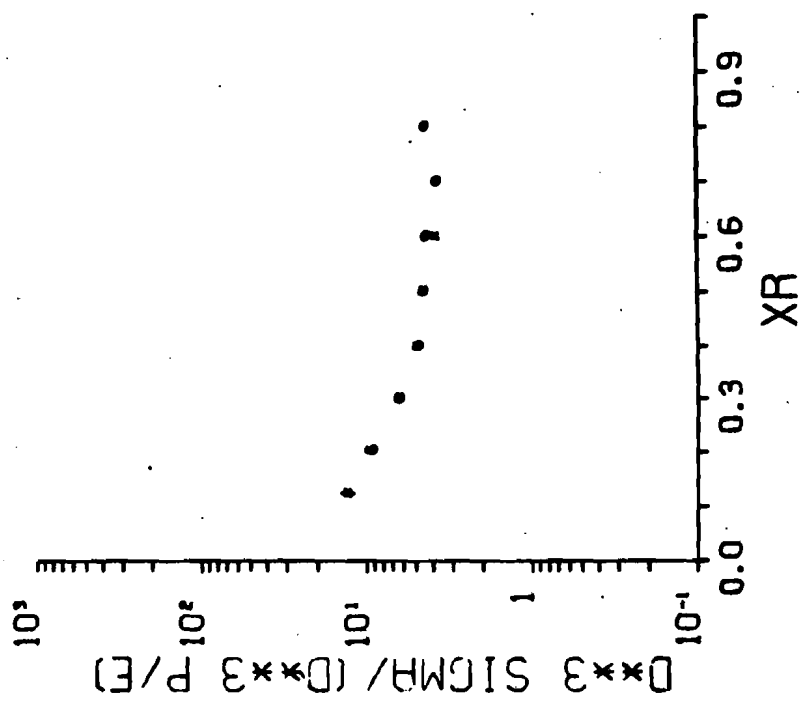


Figure 21 a

-136-

P1.P PBEAM=-100 -175
-- P PEAP=0.300

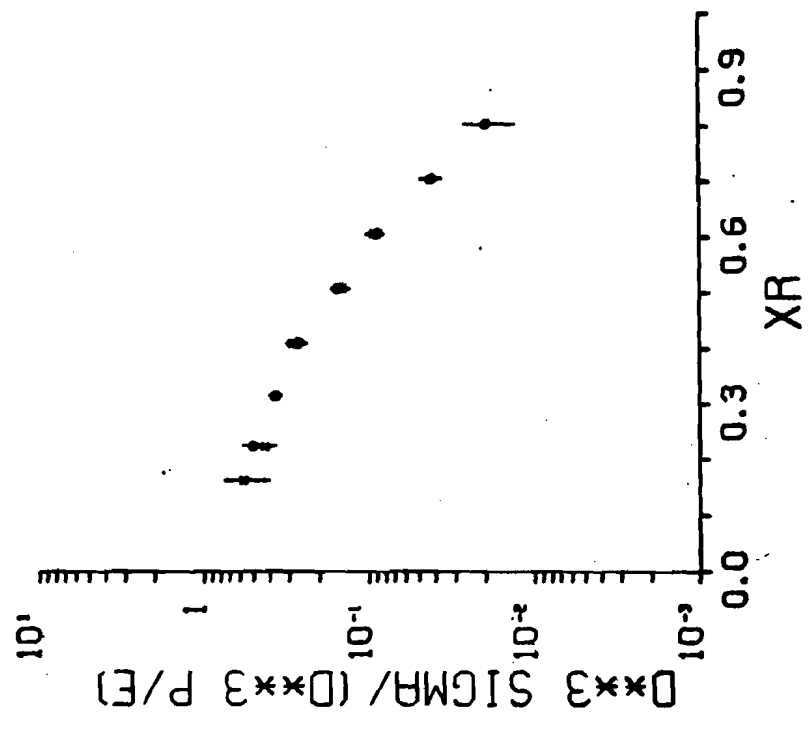


Figure 21 b

-138-
 P1.K PBEAM=100 175
 ** P PERP=0.500

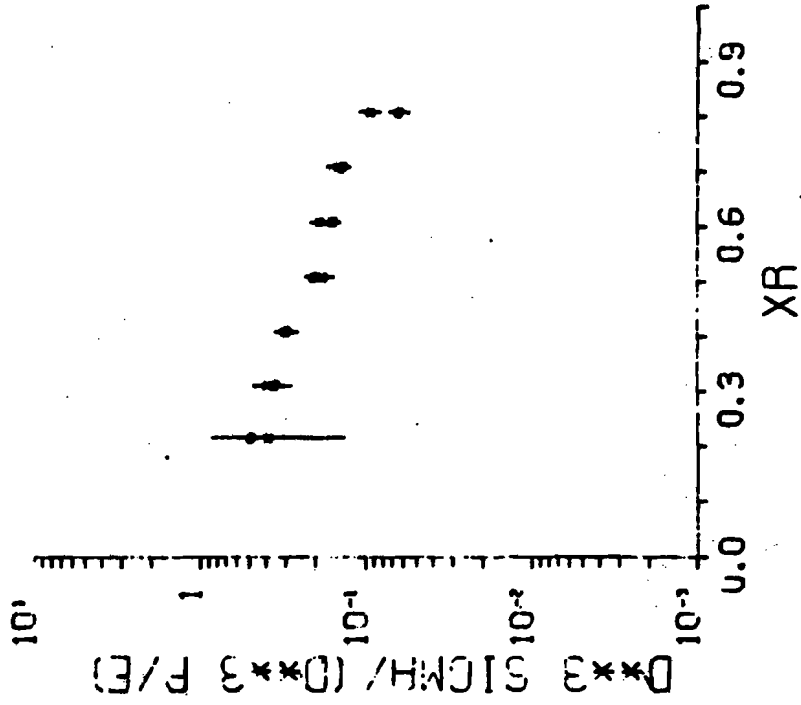


Figure 21 d

-137-
 P1.P1 PBEAM=100 175
 ** P PERP=0.500

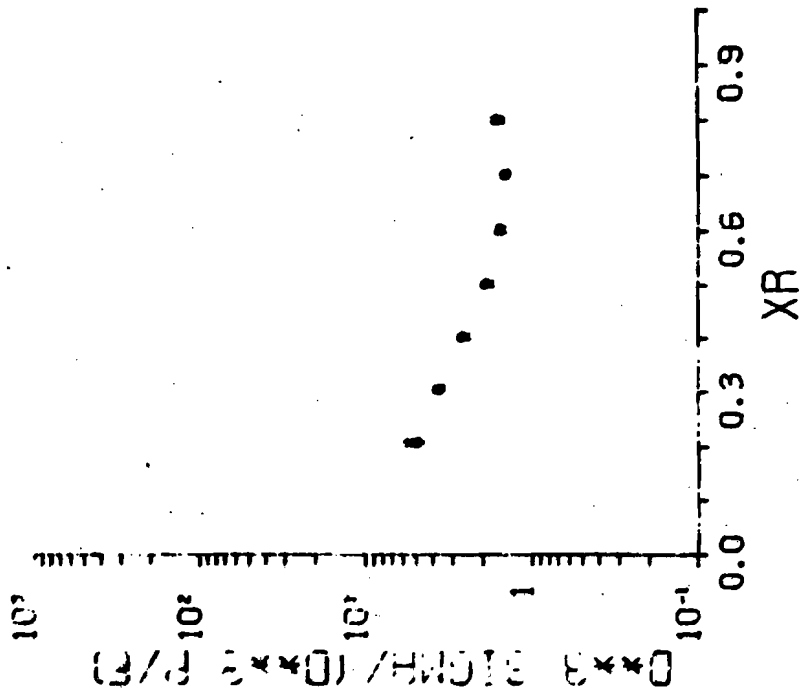


Figure 21 c

-139-
K.P1 PBEAM=100 175
** P PEMP=0.500

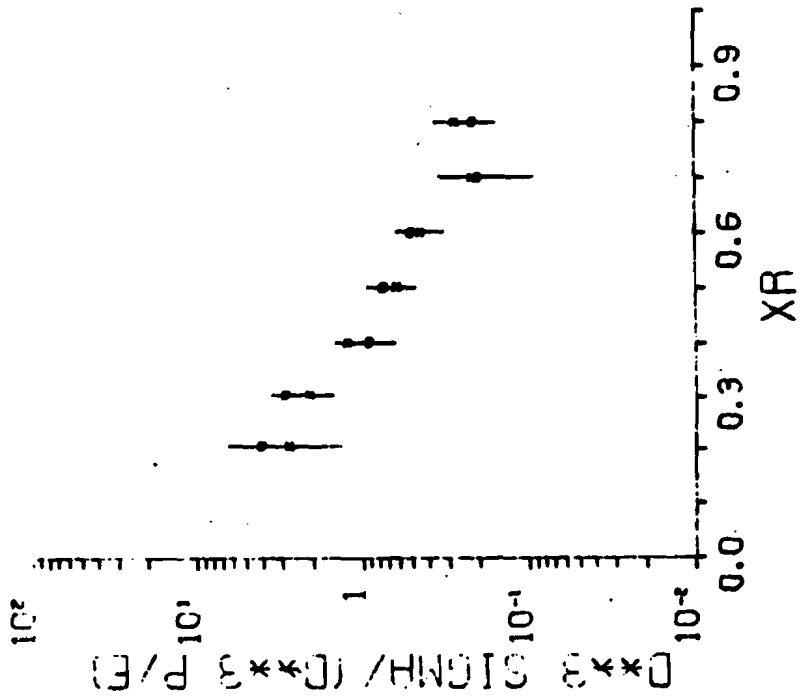


Figure 21

-140-
K.K PBEAM=100 175
** P PEMP=0.500

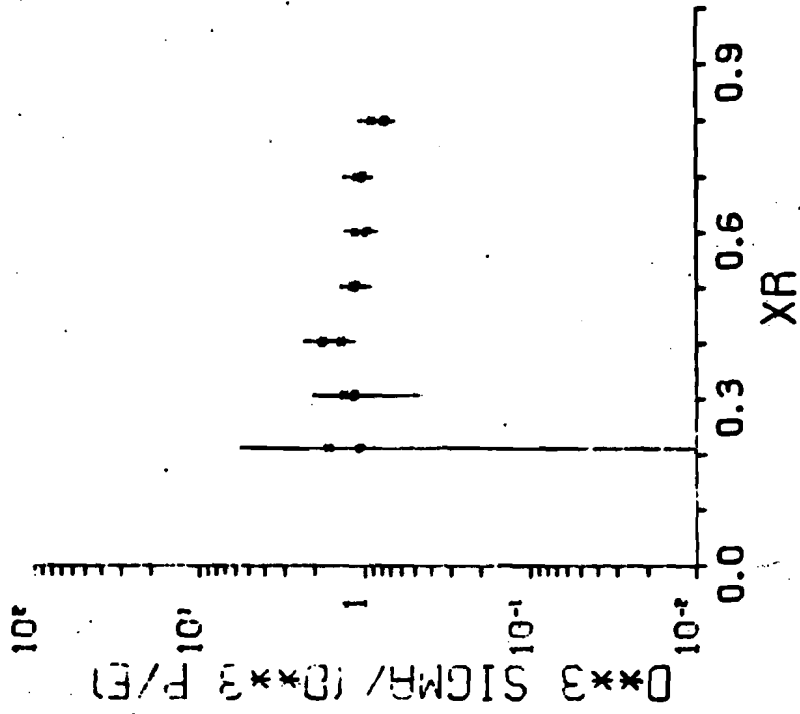
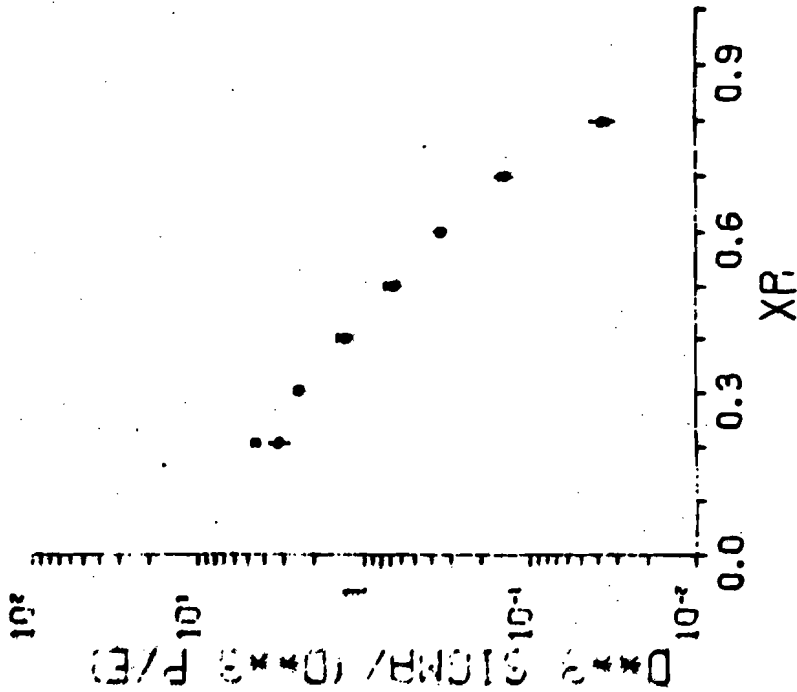
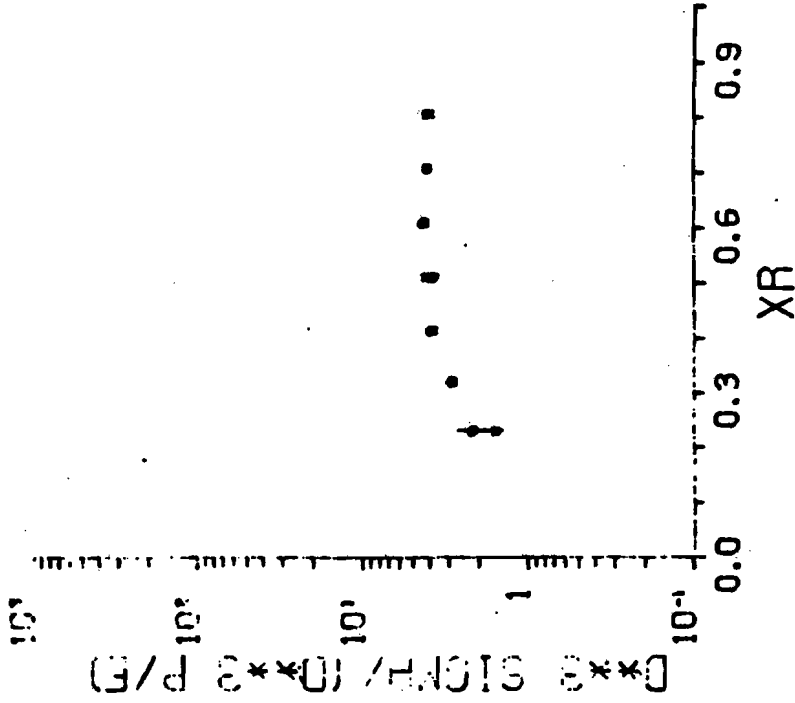


Figure 21

-141-
P.P1 PBEAM=100 175
** P PERP=0.500



-142-
P.P PBEAM=100 175
** P PERP=0.500



-143-
 P.P. PBEAM=-100 -175
 -- P PERP= 0.500

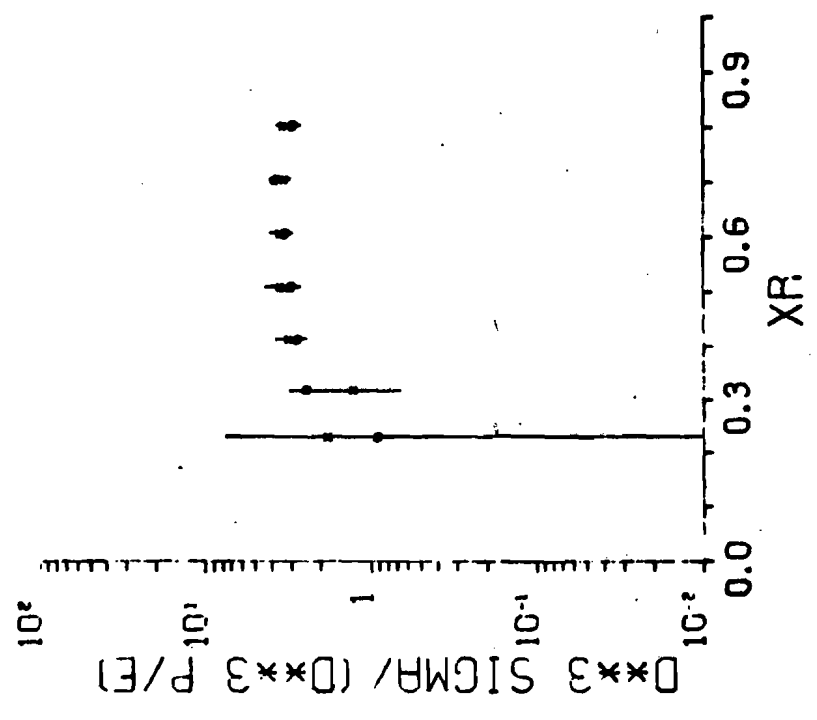


Figure 21.1

-144-
 K.K. PBEAM=-100 -175
 -- P PERP= 0.750

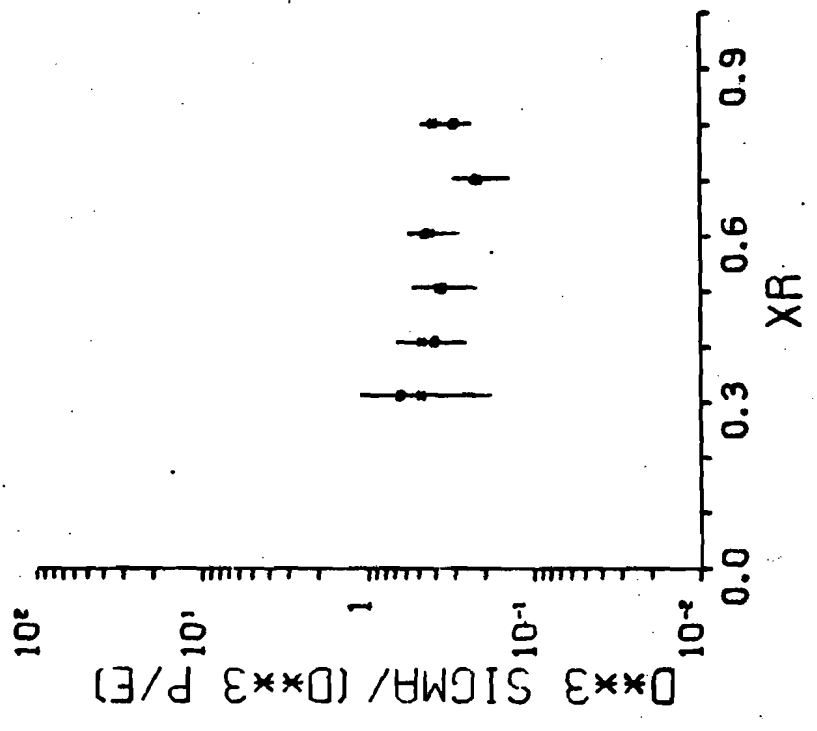


Figure 21.3

the two sets of data generally agree to better than 5% in both p_{\perp} sweeps and x sweeps. In these comparisons our overall normalisation uncertainty is not expected to play a role because it applies equally to both sets of data. The scaling hypothesis thus appears to be valid within the accuracy of our experiment. These data allow the first check of scaling at these energies for pion and kaon induced reactions.

C. The Quark Decay Model of Andersson, Gustafson, and Peterson

This fragmentation model by Andersson, et al.²⁰ draws upon some work of Field and Feynman in which the quark decay functions were determined.⁷ These quark decay functions, $D_q^h(z)$ are phenomenological constructs which give the probability of a quark, q , turning into a hadron h with some function, z , of the quark's momentum. Since the total momentum of all the hadrons must equal the momentum of the quark, the D_q^h functions must satisfy

$$\sum_h \int_0^1 dz z D_q^h(z) = 1$$

The assumption is made that these decay functions are independent of the source of the quark. Ideally these functions could all be determined from lepton-hadron experiments. However, since these experiments are not complete, theoretical prejudices have guided the final forms.

The basic idea, then, is that a quark shaken loose in a hadron-hadron collision will decay into an observable meson via these same quark decay functions. An obvious idea is to guess that the fragmentation distributions in x_T of the process $\text{hadron}_1 + p \rightarrow \text{hadron}_2 + X$ are a convolution of the momentum probability distributions, $f_q^{h_1}(x)$, of the quarks in hadron_1 with the quark decay functions $D_q^{h_2}(z)$:

where x is the quark's fraction of the total available momentum and z is hadron₂'s fraction of the quark's momentum. However, calculating this for the case of the reaction

$$p + p \rightarrow \pi^+ + x$$

using the quark distributions which have been determined in the proton, Das and Hwa found the resulting fragmentation function fell off with x_p much faster than the data indicated.²¹ They estimated that only about 1% of the high x_p cross section could come from this process.

A second piece of data Andersson *et al.* used is the result of a bubble chamber experiment in which the charge excess was measured as a function of rapidity as shown in Figure 22.²² For a 100 GeV pion, the rapidity in the center of mass for $x_p = 0.1$ is about 2.3. Hence it appears that about one-half to two-thirds of the pion's charge, on the average, is left in the central region. This would indicate the interaction proceeds via quark exchange, rather than some neutral particle exchange.

In the model they have developed, when a meson interacts with the target, one of its valence quarks is wee (having negligible momentum) and remains in the central region after interacting. The other quark continues on with almost all of the original momentum. This quark then fragments or decays via the D_q^h functions determined in lepton induced reactions. This is illustrated in Figure 23.

So for the case of an incoming π^+ , about equal probabilities

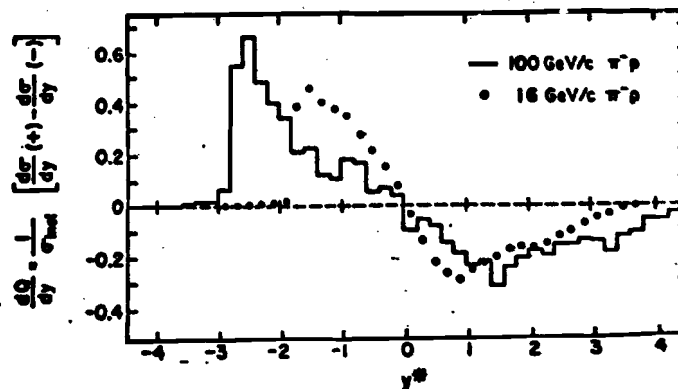


Figure 22
Charge Distributions in π^-p Interactions

QUARK FRAGMENTATION MODEL

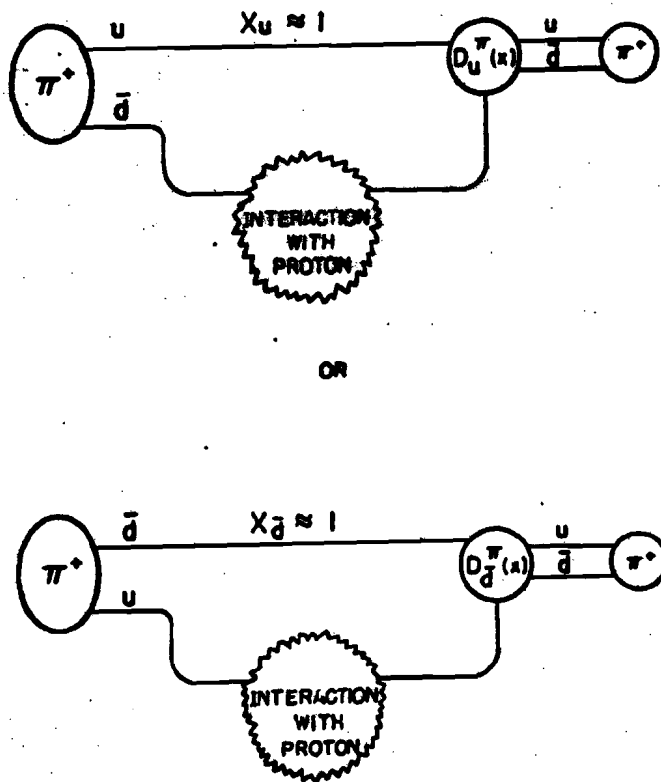


Figure 23

are expected for either the u or the \bar{d} quark to stay in the central region. The quark momentum distributions are

$$p_u^{\pi^+} \approx f_{\bar{d}}^{\pi^+} \approx \frac{1}{2} \delta(x-1)$$

This yields a fragmentation function given by

$$F^{\pi^+ \rightarrow h}(x_p) \approx \frac{1}{2} D_u^h(x_p) + \frac{1}{2} D_{\bar{d}}^h(x_p)$$

Note that by isospin and charge conjugation invariance the following are true:

$$D_u^{\pi^+} = D_{\bar{d}}^{\pi^-} = D_{\bar{d}}^{\pi^+} = D_u^{\pi^-}$$

$$D_{\bar{d}}^{\pi^+} = D_u^{\pi^-} = D_{\bar{d}}^{\pi^-} = D_u^{\pi^+}$$

$$D_s^{\pi^+} = D_s^{\pi^-} = D_s^{\pi^+} = D_s^{\pi^-}$$

Hence the predictions are:

$$F^{\pi^+ \rightarrow \pi^-} = F^{\pi^- \rightarrow \pi^+} = \frac{1}{2} D_u^{\pi^-} + \frac{1}{2} D_{\bar{d}}^{\pi^-} = \frac{1}{2} D_{\bar{d}}^{\pi^+} + \frac{1}{2} D_u^{\pi^+} = D'$$

$$F^{\pi^+ \rightarrow \pi^+} = F^{\pi^- \rightarrow \pi^-} = \frac{1}{2} D_u^{\pi^+} + \frac{1}{2} D_{\bar{d}}^{\pi^+} = D$$

(for the non-diffractive part)

For kaon beam particles, there may be some SU3-breaking effects. These have been estimated to have the effect that the s (or \bar{s}) quark will carry the momentum 50% more often than the nonstrange quarks.²³ Hence they predict

$$F^{K^+ \rightarrow \pi^+} = F^{K^- \rightarrow \pi^-} = 0.4 D_u^{\pi^+} + 0.6 D_s^{\pi^+}$$

$$F^{K^- \rightarrow \pi^+} = F^{K^+ \rightarrow \pi^-} = 0.4 D_u^{K^-} + 0.6 D_s^{K^-}$$

These predictions are parameterless and give absolute cross sections. Our data have been plotted along with the predictions scaled by $\frac{\sigma_{inel}^X}{s}$ in Figures 24 and 25. The values of σ_{inel} were taken from Ayres, et al.¹⁴ For the reactions $\pi^+ + p \rightarrow \pi^+ + X$ and $\pi^- + p \rightarrow \pi^- + X$, we have subtracted a term $\frac{A}{1-x} + \frac{B}{(1-x)^{3/2}}$ from our cross sections corresponding to the diffractive component. We see that the overall normalizations do not agree with the data although they are within a factor of two. However, a more important defect is the fact that the fall off with increasing x is slower than the data indicate.

Similar predictions can be made for mesons going to kaons. However, the functions used by Field and Feynman were derived with very little data and assumed the k/v ratio approached 0.5 as $x_F \rightarrow 1$. Recent data suggest that the k/v ratio is about 0.1.²⁴ For this reason, Andersson, et al. reparameterized the decay functions

$$D_u^{K^+}, D_u^{K^+}, D_s^{K^+}, \text{ where}$$

$$D_u^{K^+} = D_{\bar{u}}^{K^-}$$

$$D_u^{K^+} = D_{\bar{d}}^{K^-} = D_u^{K^-} = D_d^{K^+} = D_{\bar{d}}^{K^+} = D_d^{K^-}$$

$$D_s^{K^+} = D_s^{K^-}$$

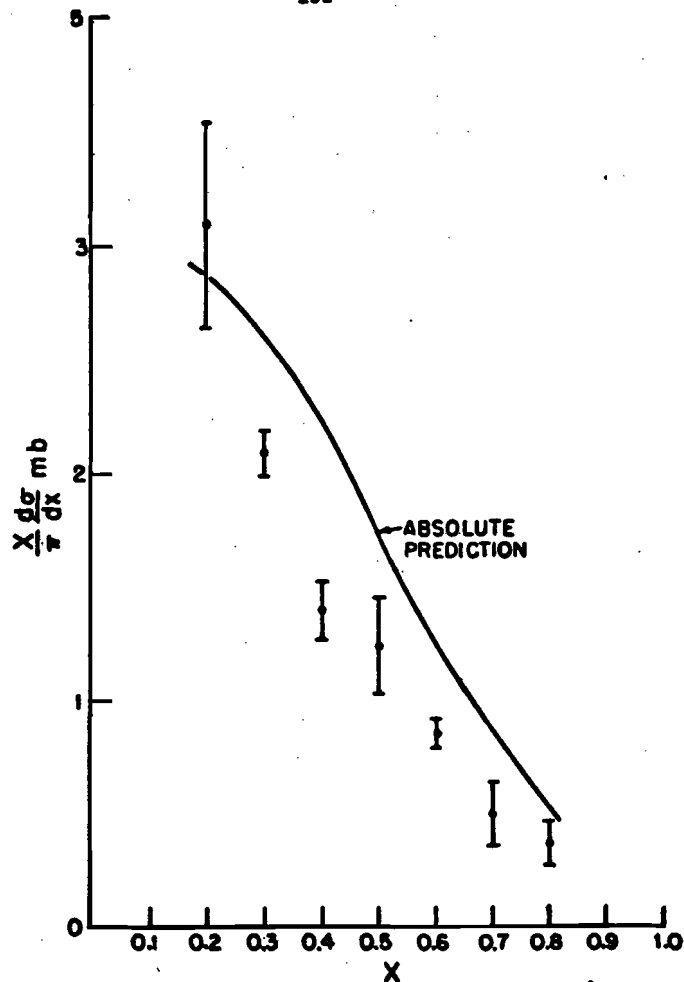


Figure 24 a. Quark Fragmentation Model $\pi^+ + p \rightarrow \pi^+ + X$ after Diffractive Peak Subtraction.

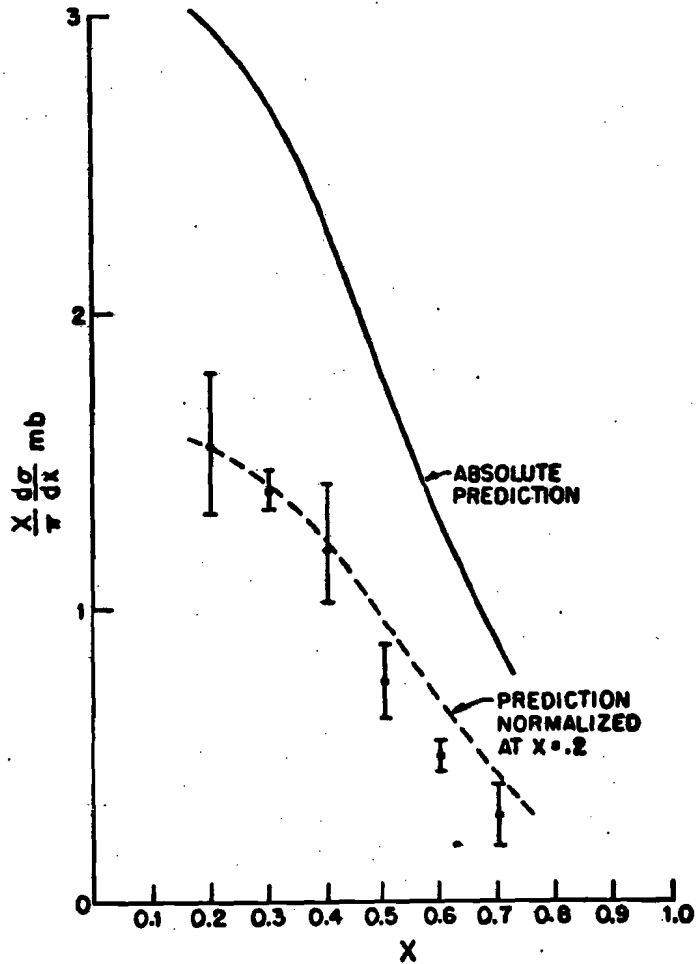


Figure 24 b. Quark Fragmentation Model
 $\nu^-p \rightarrow \nu^-X$ after Diffractive Peak Subtraction

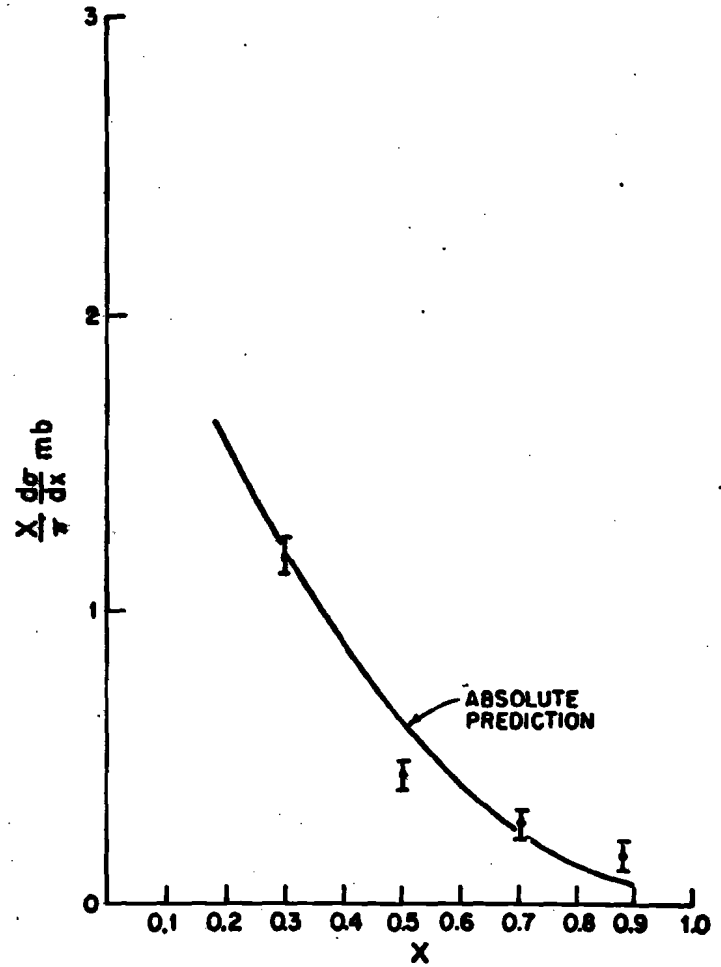


Figure 24 c. Quark Fragmentation Model
 $\nu^+p \rightarrow \nu^+X$

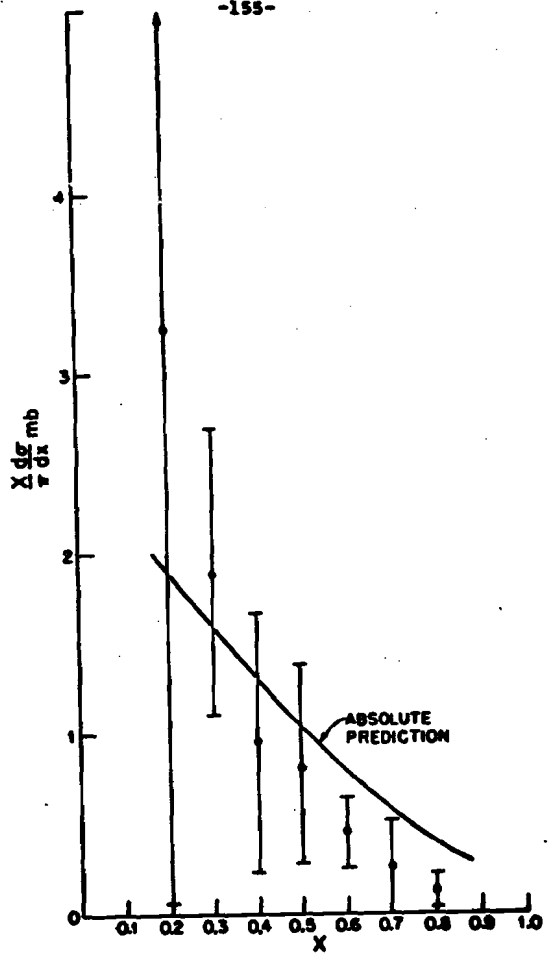


Figure 25. Quark Fragmentation Model $K^+ + p \rightarrow \pi^+ + X$

They also made the assumption

$$D_S^{k^+} = D_S^{k^-} = D_S^{k^0}$$

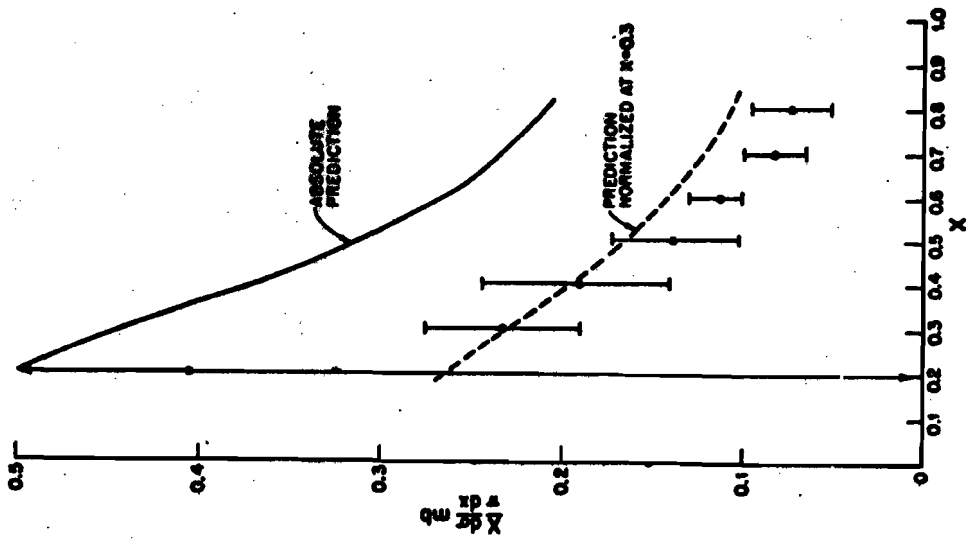
With these assumptions, our data for $\pi^+ + p \rightarrow k^+ + X$ are plotted in Figure 26 along with the model predictions, i.e.,

$$F^{\pi^+ \rightarrow k^+} = F^{\pi^+ \rightarrow k^-} = \frac{1}{2} D_u^{k^+} + \frac{1}{2} D_d^{k^+}$$

We see that the model suffers from the same problem of falling off too slowly.

Putting aside the question of normalizations, the slopes of the curves do not seem to agree well with the data. We believe the slopes are related to the requirement of the delta functions in the quark momentum probability distributions. The delta function requirement was introduced without rigorous physical justification. We can ask whether a different assumption will produce better agreement. We have replotted in Figure 27 the $K^+ + \pi^+$ data along with the prediction using a $\delta(x - 0.7)$ function instead of $\delta(x - 1)$, i.e., the case where the fast quark has only 70% of the incident meson's momentum. We normalized this curve at $x = 0.3$. We see that we have much better agreement. However, this method corresponds to using values of $D_q^h(x_p/0.7)$. These decay functions were only defined for arguments between 0 and 1. Hence a naive application of this delta function assumption may result in unphysical results when $x_p > 0.7$.

-157-



-158-

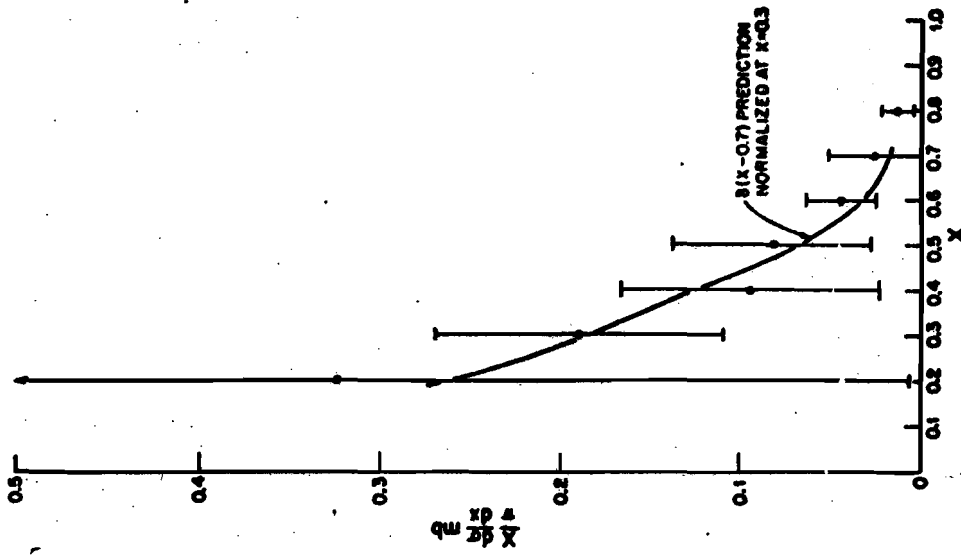


Figure 27. Quark Fragmentation Model
 $K^+ p \rightarrow \pi^+ X$

Finally, Andersson et al. assume that for baryon fragmentation only one valence quark is left in the central region. In this case a diquark system carried most of the momentum and decays. Hence they require the definitions

$$D_{uu}^{\pi^+}(z) \equiv H_1(z)$$

$$D_{ud}^{\pi^-}(z) = D_{ud}^{\pi^+} \equiv H_2(z)$$

and

$$D_{uu}^{\pi^-} \equiv H_3(z)$$

These functions could in principle be determined from high E_{jet} x lepton production in which a valence quark is "kicked out" by the virtual photon and what is left is a diquark system. This system should produce particles in the same way that hadronic processes do. However, the data are too skimpy for any parameterizations to be made.

The assumptions in this model have been introduced in a rather ad hoc fashion. For instance, we know that the valence quark momentum distributions, $f_u^{\pi^+}$, $f_d^{\pi^+}$, of the quiescent pion are not delta functions and are probably not completely independent. The way the assumptions of the model have incorporated these facts is not clear. K. Huang has suggested a more physical interpretation of this model.²⁵

Assume that the quiescent pion has some joint momentum probability distribution $\psi(x_1, x_2)$ for its valence quarks. The process of interaction transforms this joint probability

distribution such that the resulting distribution is sharply peaked at $x_1 \sim 1$, $x_2 \sim 0$, and $x_2 \sim 1$, $x_1 \sim 0$. This comes about because the interacting quark must be a *wee* quark; the pion's remaining momentum must be carried by the other quark. The final momentum distribution can be approximated by independent delta functions

$$\psi_{\text{final}}(x_1, x_2) \sim \frac{1}{2} \delta(x_1 - 1) \delta(x_2) + \frac{1}{2} \delta(x_2 - 1) \delta(x_1)$$

The quarks then fragment according to the D_Q^h functions as before.

D. Quark Recombination Model of Das and Hwa

The basic idea of this recombination model by Das and Hwa²¹ is illustrated in Figure 28 for the reaction $p + p \rightarrow \pi^+ + X$. Let us assume that the incoming proton has valence quark distributions $u(x_1)$, $u(x_2)$, and $d(x_3)$, where the x_i are equal to the momenta of the i^{th} quark divided by the momentum of the incoming proton. Then the argument is made that to produce a pion at large Feynman x , a large quark whose momentum is also large must initiate the process. The only quarks with a reasonable probability of having a large momentum are the valence quarks. The central assumption in this model is that the fast quark distribution is unchanged by the collision between the hadrons. This allows the use of the valence quark distributions in the proton as determined by deep inelastic electroproduction. All other details of the interaction are not specific in this model. The antiquark required to produce the pion can either come from the incident hadron sea or can be produced by a gluon from the interaction. Whatever their source, only antiquarks moving in the same direction as the incident hadron are allowed to recombine. These antiquarks would not be present in electroproduction and hence this process would not be allowed. The final element in this model is a recombination probability function, R , which gives the probability that quarks at x_1 and x_2 recombine to make a meson with some x . For this process, then, we have

RECOMBINATION MODEL

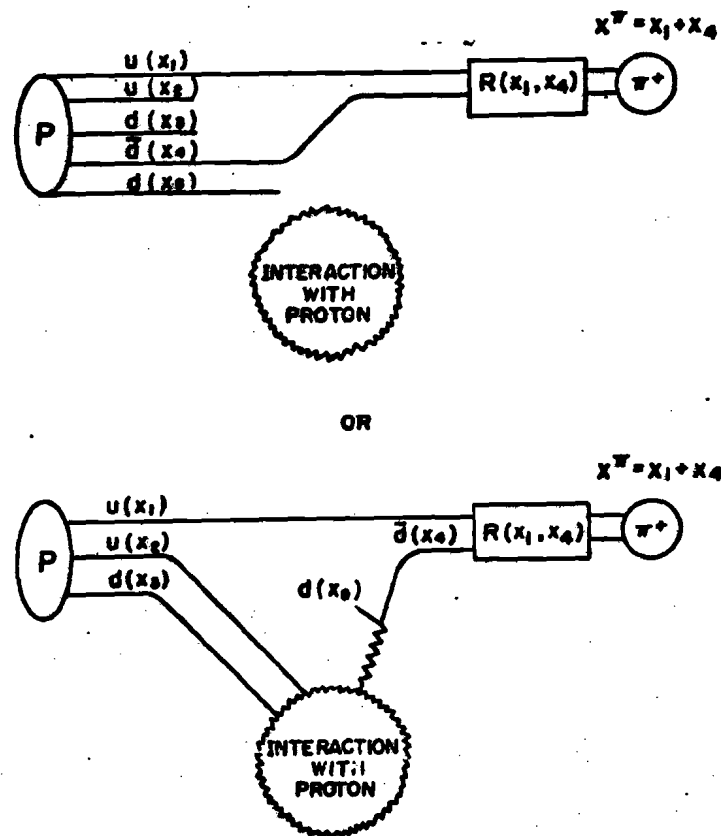


Figure 28

$$x \frac{d\sigma}{dx} \propto \int F(x_1, x_2) R(x_1, x_2, x) (x_1 x_2)^{-1} dx_1 dx_2$$

$F(x_1, x_2)$ is the momentum probability distribution for having a quark at x_1 and an antiquark at x_2 . The quark distributions should be uncorrelated aside from kinematical constraints because of the sizable difference between x_1 and x_2 on the average. Das and Hwa assume

$$F(x_1, x_2) = F_q(x_1) F_{\bar{q}}(x_2) \beta (1 - x_1 - x_2)$$

where $\beta(1 - x_1 - x_2)$ is the phase space factor and β is a constant. This is only an approximation since integration of the joint quark probability distribution does not reproduce the single quark distributions.²⁶

The recombination function is assumed to be scale invariant and is taken to be

$$R(x_1, x_2, x) = R_2 \left(\frac{x_1}{x}, \frac{x_2}{x} \right) \delta \left(\frac{x_1}{x} + \frac{x_2}{x} - 1 \right) + R'$$

where R_2 represents the probability of recombination of the q and \bar{q} and where R' represents all other recombination processes involving the q , \bar{q} and other constituents such as quark-antiquark pairs and gluons. R' is expected to be small with respect to R_2 and will be ignored. The form of R_2 is taken to be:

$$R_2 = c \frac{x_1 x_2}{x}$$

where c is some normalization constant. This symmetric form gives the maximum probability for recombination when $x_1 = x_2$.

So for our example of $p + p \rightarrow \pi^+ + X$ we have

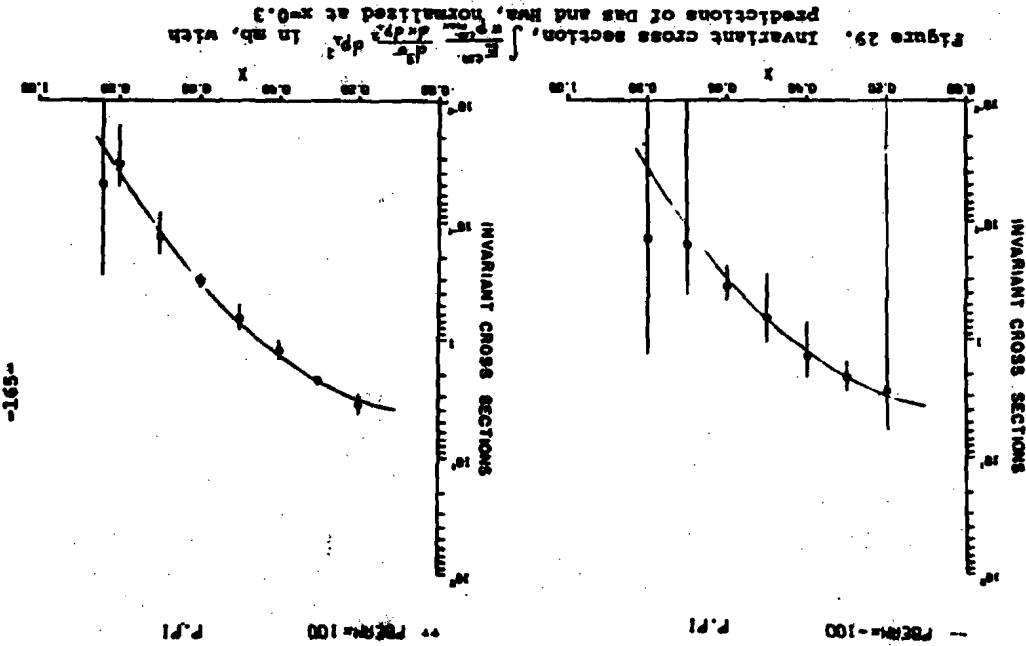
$$x \frac{d\sigma}{dx} \propto \frac{1-x}{x} \int_0^x F_u(x_1) F_{\bar{d}}(x-x_1) dx_1$$

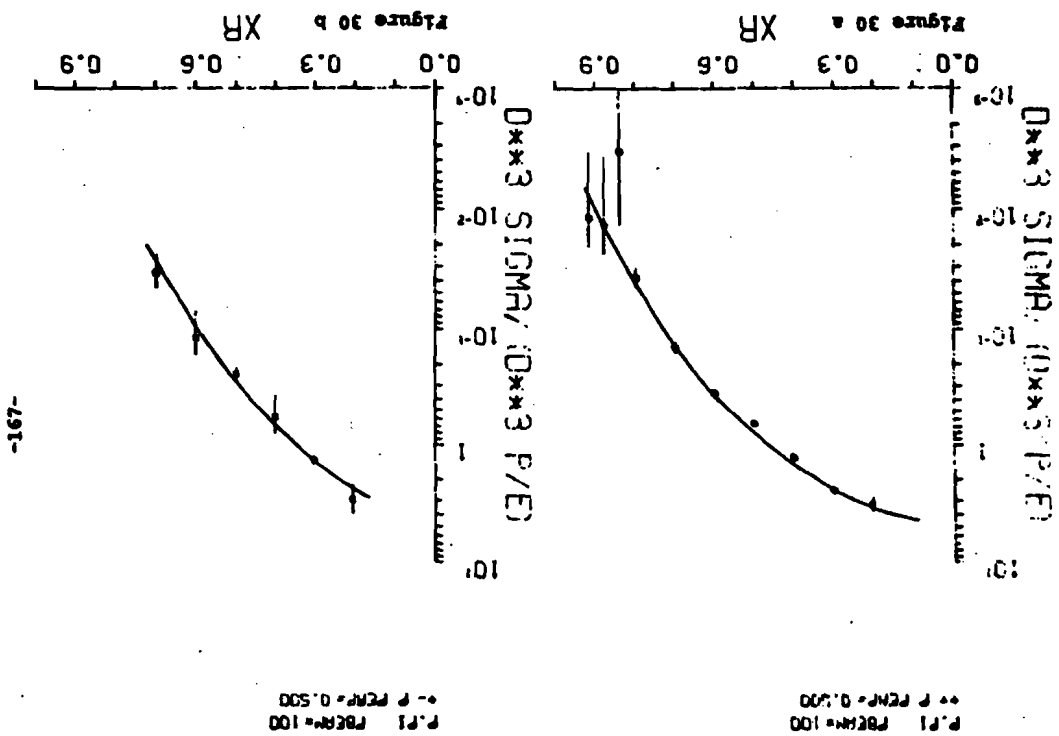
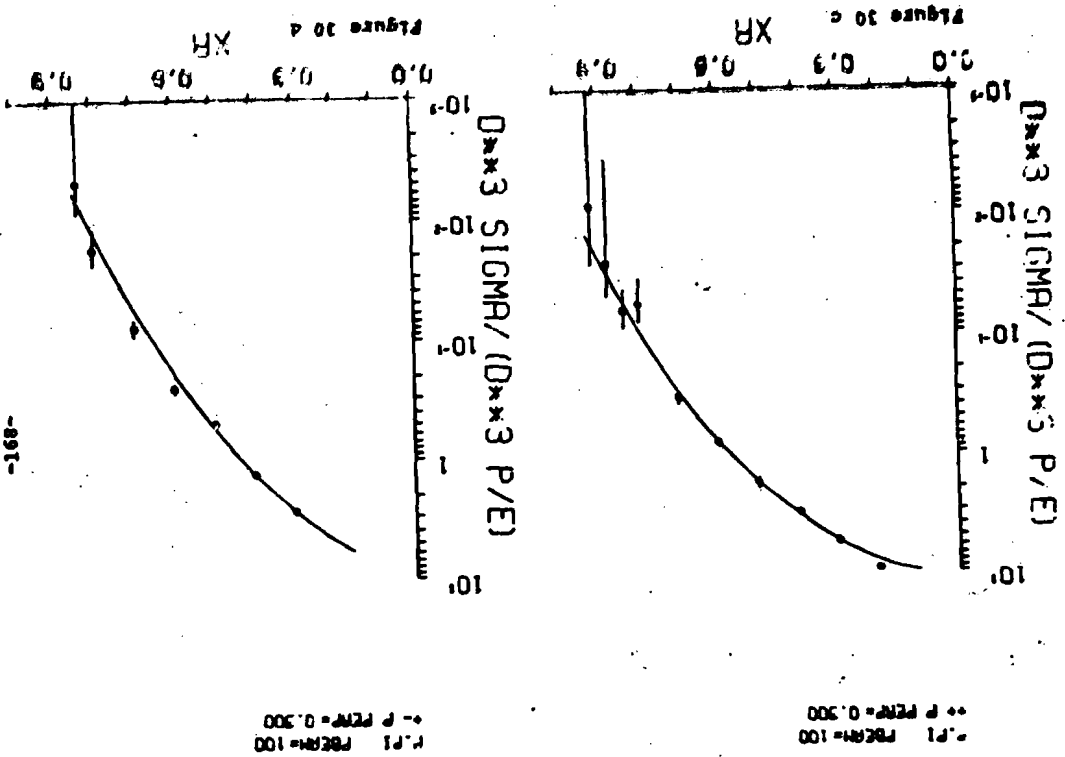
It should be noted that the antiquark distribution need not be the same as those in the initial hadron since the interaction could have created many $q\bar{q}$ pairs.

These distributions have been generated and our data plotted over them in Figures 29 and 30. The F_q distributions were taken from parameterizations of electroproduction data by Field and Feynman.⁷ For simplicity the antiquark distributions were taken to be those determined by Field and Feynman also. Since our integrated results are similar to the unintegrated cross sections, we have plotted both sets of data. In either case we have normalized the data at one value of x . We have also plotted the data for the reaction $\bar{p} + p \rightarrow \pi^- + X$. Except for normalization, this reaction should be similar to $p + p \rightarrow \pi^+ + X$. Our data show that within errors, this is so.

These predictions are not very sensitive to the exact form of the sea quark distributions, $F_{\bar{u}}$, $F_{\bar{d}}$, $F_{\bar{s}}$ and $F_{\bar{c}}$. Duke and Taylor have used this model and shown that these

Figure 30. Invariant Differential Cross Sections, $E \frac{d^2\sigma}{d^3p_T dy}$ in mb/GeV^2 , with predictions of Das and Hwa's quark recombination model. Predicted curves are normalized at $x_F=0.3$ with the exception of plot e where the curve is normalized at $x_F=0.12$





P.F1 PBCRM=100
P.P PCRM=0.500

P.F1 PBCRM=100
P.P PCRM=0.500

-491-

-891-

P.T. BEAM=175
P PERM=0.500

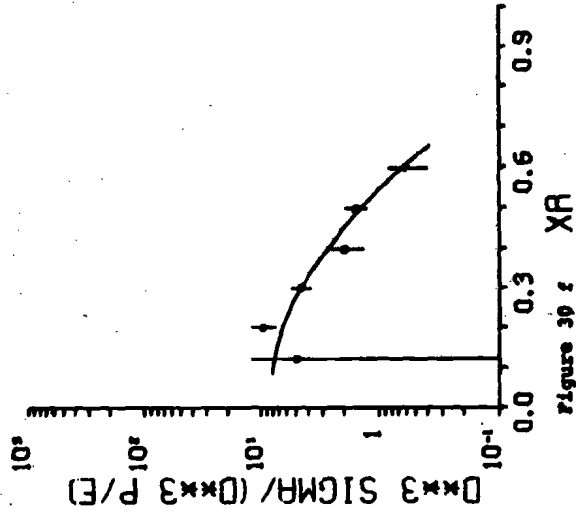


Figure 30 z XR

P.T. BEAM=175
P PERM=0.500

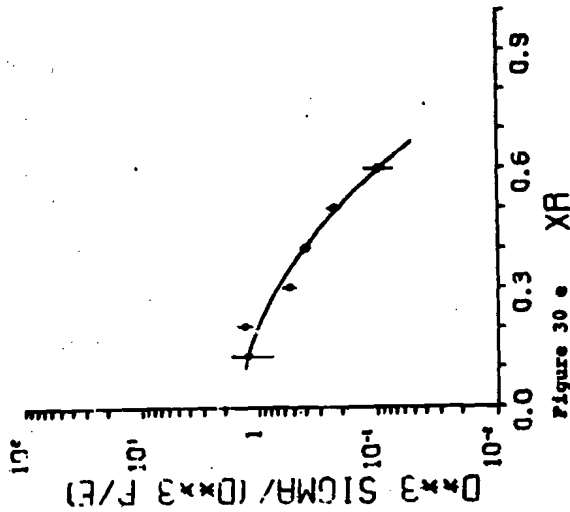


Figure 30 e XR

sea quark distributions are sensitive to the particle production ratios²⁷, e.g.,

$$\frac{\pi^+}{\pi^-}(x) = \frac{\alpha_u + \beta_u + \int_0^x F_u(x_1) F_d(x-x_1) dx_1}{\alpha_s + \beta_s + \int_0^x F_s(x_1) F_u(x-x_1) dx_1}$$

and

$$\frac{K^+}{K^-}(x) = \frac{\alpha_u + \beta_u + \int_0^x F_u(x_1) F_s(x-x_1) dx_1}{\alpha_s + \beta_s + \int_0^x F_s(x_1) F_u(x-x_1) dx_1}$$

They assumed all the α 's and β 's were equal and cancelled in the ratios. They have also assumed the forms $\bar{u}(x) = \bar{d}(x) = u_0(1-x)^{n_u}$ and $s(x) = \bar{s}(x) = s_0(1-x)^{n_s}$. They have fit averaged data from FNAL¹ and ISR² from several p_T values, since no systematic p_T dependence over the low p_T range was observed. They obtained the values $n_u = 8 \pm 1$ for the FNAL results and a somewhat higher value, about $n_u = 10$, to accommodate the ISR data. The FNAL results were fit well by $u_0 = 1.2 \pm 0.1$, $n_s = 5.75 \pm 2.3$, and $s_0 = 0.135 \pm 0.015$.

Our ratios have been fit by this process, although we chose to fit the inverse of the ratios given above. The results are shown in Figure 31. Our values are $u_0 = 1.03 \pm 0.55$, $n_u = 12.9 \pm 4.6$, $n_s = 3.62 \pm 1.33$, which are consistent with Duke and Taylor's determination. s_0 was not determined by our fits.

This model is incomplete at present. It only accounts for

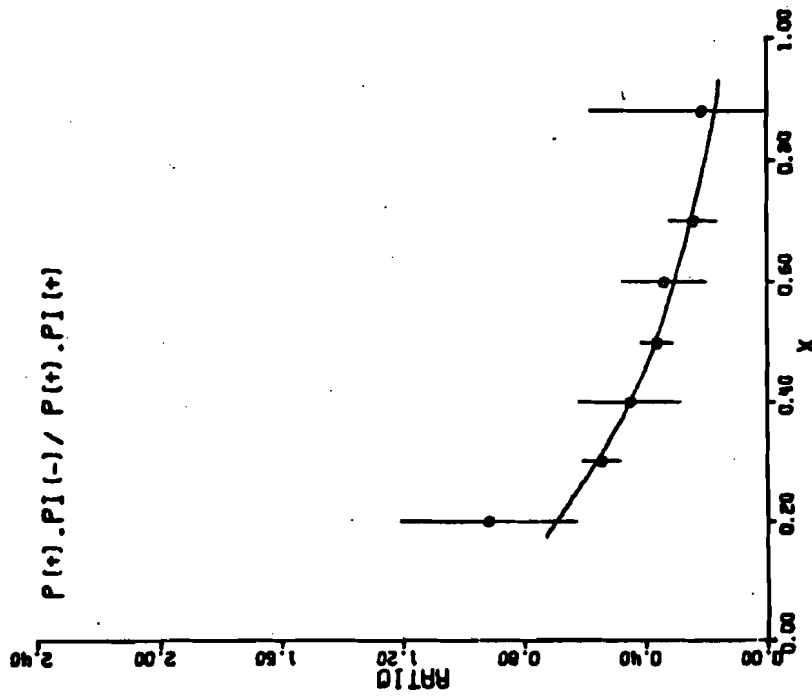


Figure 31 a. Particle Ratios with Best Fit using Das and Hwa's Model

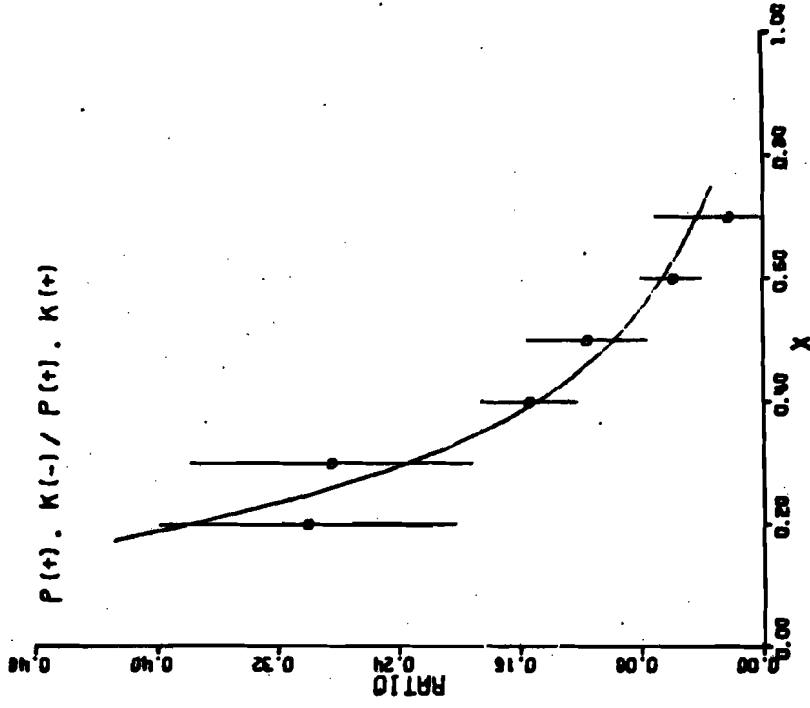


Figure 31 b. Particle Ratios with Best Fit using Das and Hwa's Model

two-body recombination and hence does not allow for reactions which produce a baryonic fragment. A second difficulty is that only the proton's quark distributions have been determined with any accuracy so that no predictions can be made for meson fragmentation. In this sense it complements the quark fragmentation model whose predictions are now available for meson fragmentation but not for baryon fragmentation. It is also interesting to note that one of the original motivations for this model was that a naive application of the quark fragmentation ideas did not predict the correct normalization for the data, as mentioned in section C. This model however, does not even attempt to predict the absolute normalizations, but instead used the α 's and β 's to scale the predictions to the data.

Although we could not use this model to make predictions about the pion fragmentation cross sections, we have used this model to attempt the inverse process. That is, we used our data to try to determine the pion's quark distributions by fitting to the cross sections $\pi^+ + p \rightarrow \pi^+ + X$, $\pi^+ + p \rightarrow \pi^- + X$, $\pi^+ + p \rightarrow K^+ + X$ and $\pi^+ + p \rightarrow K^- + X$, at $p_A = +100$ GeV/c and $p_{\perp} = 0.3$ GeV/c. We immediately encountered two problems. The first was the diffractive peak in the $\pi^+ + p \rightarrow \pi^+ + X$ reaction. We attempted to remove this by subtracting terms of the form $\frac{A}{1-x} + \frac{B}{(1-x)^{3/2}}$. A and B were evaluated at $x = 0.89$ and $x = 0.92$ where the error due to a fragmentation tail was believed to be small. These terms were motivated by the work

of Hsing²⁸ who determined that these were the forms of the significant triple Regge contributions. The second problem was the known resonance production of ρ^0 's and f^0 's in both the $\pi^+ + p \rightarrow \pi^+ + X$ and $\pi^+ + p \rightarrow \pi^- + X$ reactions. We have attempted to remove this contribution by estimating these cross sections at $p_{\perp} = 0.3$ from a fit to the data assuming one pion exchange.¹⁷

The form of the pion distributions was assumed to be:

$$s(x) = \bar{s}(x) = s_0 (1-x)^{n_s}$$

$$\bar{u}(x) = d(x) = d_0 (1-x)^{n_d}$$

$$u(x) = \bar{d}(x) = a x + \bar{u} x \text{ for } x \leq 0.15$$

$$a \sqrt{0.15} (1-x)^{n_u} + \bar{u}(x) \text{ for } x > 0.15$$

The small x form for the valence quarks is motivated by the "Regge scaling" requirement as suggested by Farrar.²⁹ The results of this fit are shown in Figure 32. While the fits are not perfect, they seem to do remarkably well in predicting the trend of the data, especially with such a simple model and such crude approximations. The values of the fit parameters were

$$n_u = 1.51 \pm 0.58$$

$$n_d = 3.04 \pm 0.26$$

$$n_s = 0.85 \pm 0.25$$

The values of the coefficients were essentially undetermined although the values

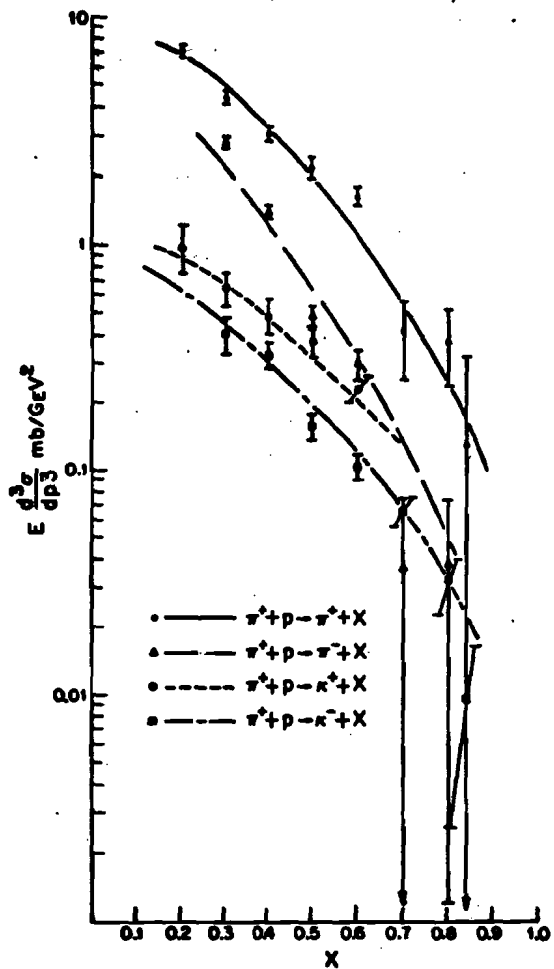


Figure 32. Das and Hwa Model
Fits to Quark Momentum Probability
Distributions.

$$a = 2.28$$

$$s_0 = 0.66$$

$$d_0 = 4.66$$

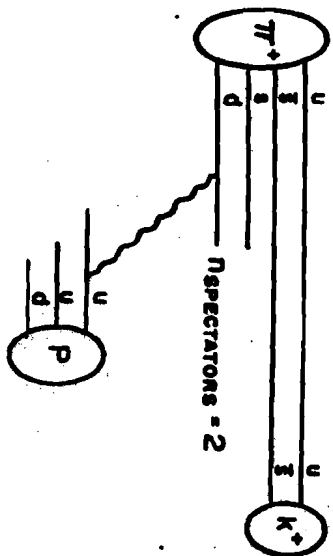
and an overall normalization constant equal to 0.39 gave a reasonable fit with a $\chi^2 = 72.9$ for 28 degrees of freedom.

2. Fragmentation Model of Brodsky and Gunion

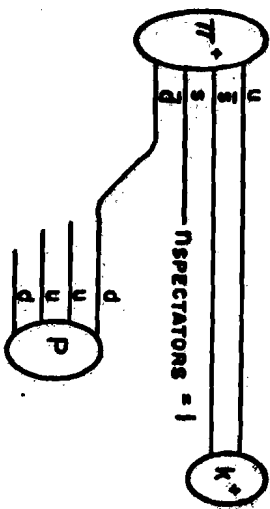
The fragmentation model presented by Brodsky and Gunion can be well tested by our data.³⁰ The essential point of this model is that by examining the behavior of the cross sections as a function of $(1-x)$, it can be determined whether the initial interaction between hadrons is mediated by gluon exchange or wee quark exchange or annihilation. Examples of the three possible cases are shown in Figure 33 for the reaction

$$\pi^+ + p \rightarrow K^+ + X$$

The quark exchange or annihilation process is the quantum chromodynamic version of Feynman's wee parton exchange idea.⁶ This model predicts the same $(1-x)$ behavior for both processes and does not propose to distinguish between the two. In either case, the incident pion, which has a u and \bar{d} valence quark, is required to have in addition an s and \bar{s} quark pair taken from its sea in order to make a K^+ . Brodsky and Gunion impose this condition from the requirement of Feynman scaling. Either the s or \bar{d} quark is required to have rapidly in the central region. This quark then interacts with the target via quark exchange or quark annihilation into a color singlet with a wee quark from the target. The remaining quarks in the π^+ and the proton form color triplets which start to separate. The u and \bar{s} quarks in the beam particle, however, can form a K^+ with some fraction of the incident momentum x . This leaves the fraction $(1-x)$ of the incident momentum to be taken up by the remaining



WEE QUARK EXCHANGE



QUARK ANNIHILATION

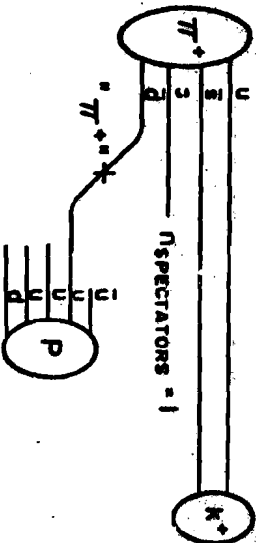


Figure 33. Fragmentation Model of Brodsky and Gunion

quark. This quark is known as a spectator, since it cannot combine to form a detectable particle nor did it interact with the target.

By invoking the dimensional counting rules³¹, the cross sections $x \frac{d\sigma}{dx}$ are predicted to have the form

$$x \frac{d\sigma}{dx} \sim (1-x)^{2n_{\text{spectators}}-1}$$

Intuitively, as the number of spectators, which share the total momentum, increases, the probability for finding a fragment with a large fraction of the momentum, i.e., high x , must be suppressed. Thus the above situation represents the lowest order process. Since the incident pion can have more than one $q\bar{q}$ pair from the sea, there will be contributions from processes with more spectators. However, these contributions will have higher powers of suppression for large values of x .

The gluon exchange mechanism differs from quark exchange in that a gluon is exchanged in the interaction. The gluon changes the color of both the receiving and originating quark. Thus what are left are two separating color octets. Again the u and \bar{s} quarks can form a color singlet, the K^+ . However, now there are two quarks left to share the momentum; i.e., two spectators. Note that these quarks do not form a color singlet. Therefore the counting rule predicts the power of $(1-x)$ for this process to be two greater than that for quark exchange.

The x which describes these reactions is the light cone or

infinite momentum fraction. The best approximation to this variable is the radial scaling variable $x_R = E_C^{C.M.}/E_{\text{max}}^{C.M.}$ used by Taylor, et al.¹⁶ This variable becomes equal to the Feynman x_F as $s \rightarrow \infty$. Our fits were made in terms of x_R .

The predicted powers of $(1-x)$ should be essentially independent of transverse momentum for small values of p_T . The exchanged quark or gluon absorbs the momentum transfer t prior to the beginning of fragmentation. For this reason, fits were performed on our cross sections for selected p_T values, as well as on the integrated cross sections. Some of these fits are shown in Figure 34.

Tables 4, 5, and 6 are summaries of the predicted powers and of the powers determined by the fits. The agreement with the quark exchange predictions is generally good. It should be noted that the predictions are for the minimum powers. Higher order contributions can increase the observed powers. These powers still seem to lie below the minimum allowable for the gluon exchange process. The observed powers are essentially p_T independent as predicted. This justifies our use of unintegrated cross sections in situations where the x dependence was involved.

Some reactions, however, appear to have powers which may be the result of resonance production and decay which will produce hadrons in a region where they would normally be suppressed. This is the case in the reaction $K^+ + p \rightarrow \pi^+ + X$, where K^* (890) and $K^*(1420)$ resonance production is present.¹⁷ The average

-181-

FLK PBEAM=100 -182-
 ** P PERP=0.300
 FIT: A=(1-XR) **B
 A = 0.08 +- 0.17
 B = 1.59 +- 0.25

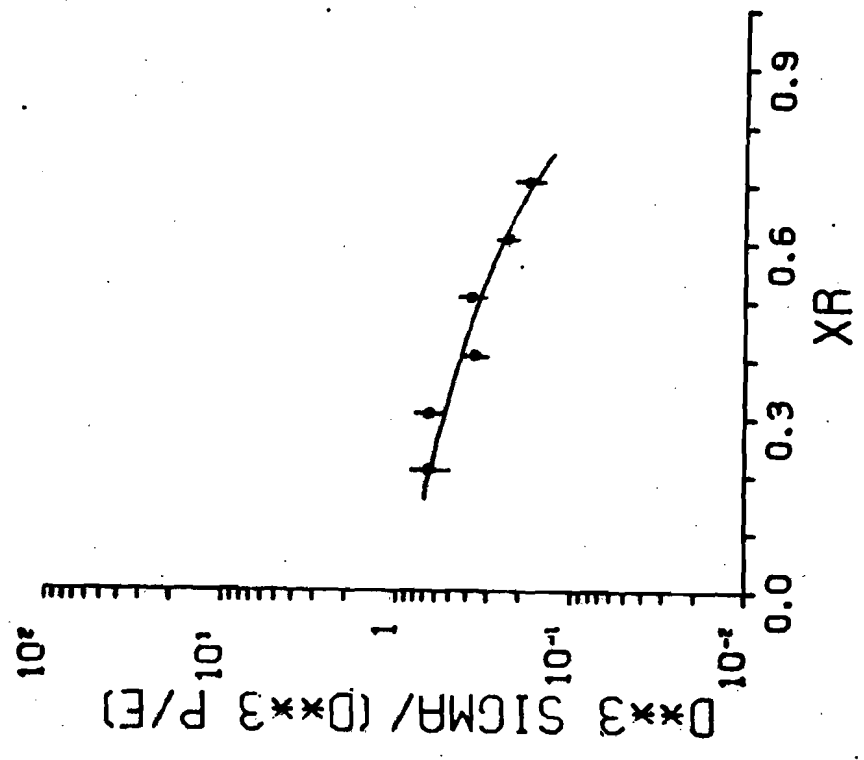


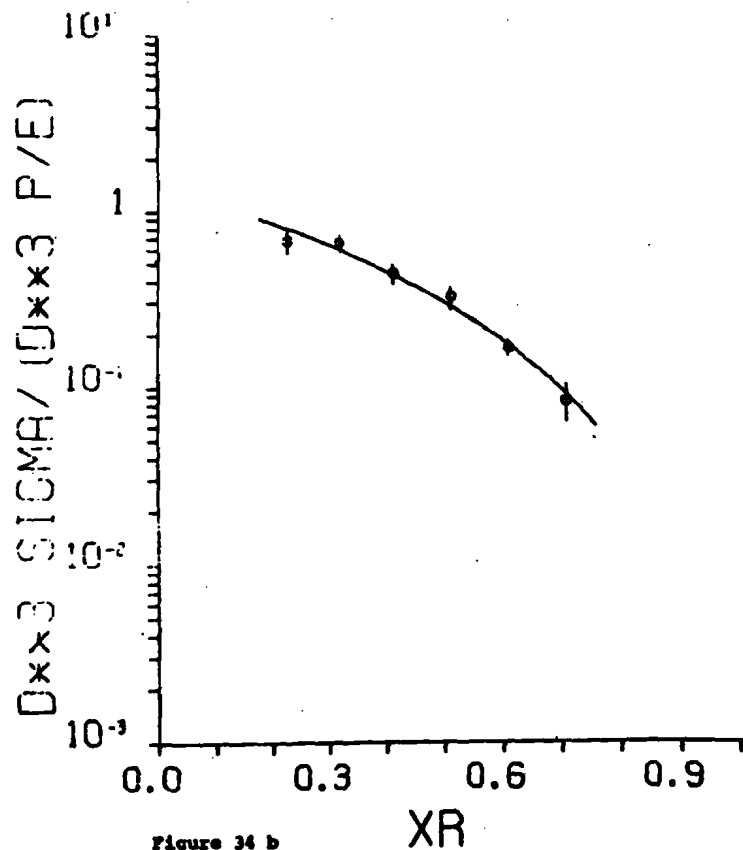
Figure 34 a

Figure 34. $(1-x_R)^B$ fits

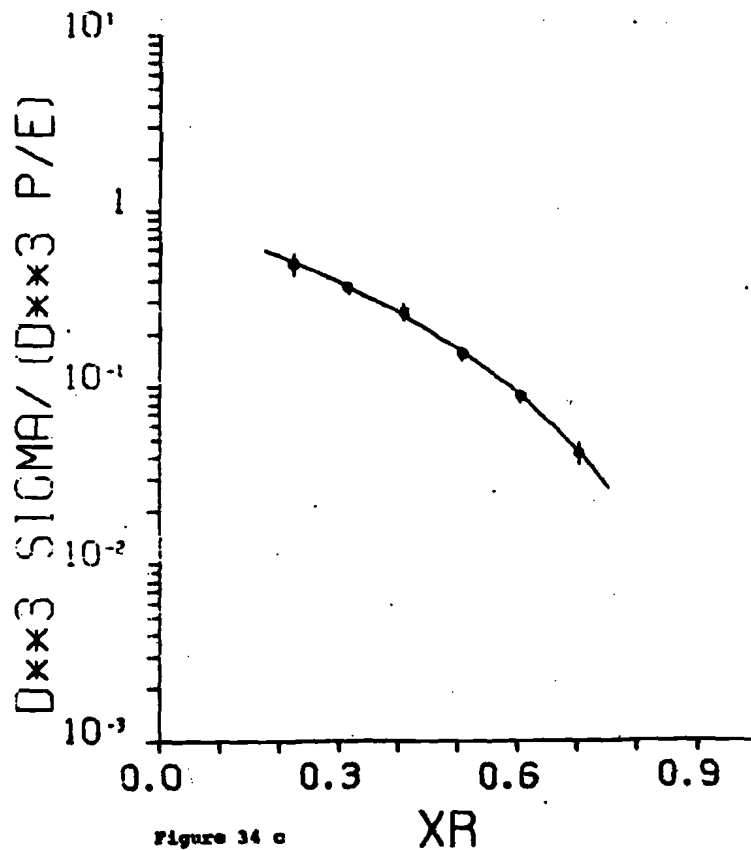
The units are mb/cos².
 The symbols denote

- x unaveraged cross sections (data taken at only one sign of the AVB angle)
- o averaged cross sections (data taken at both signs of the AVB angle)

PI.P PBEAM=100 -183-
-- P PERP=0.300
FIT: $A \times (1 - XR)^{-B}$
A = 1.39 \pm 0.18
B = 2.21 \pm 0.19



PI.P PBEAM=-100 -184-
-- P PERP=0.300
FIT: $A \times (1 - XR)^{-B}$
A = 0.98 \pm 0.11
B = 2.56 \pm 0.16



FERMILAB LIBRARY

P1.P PBEAM= 100 -106-
 +- P PERP= 0.300
 FIT: A*(1-XR) **B
 A = 0.70 +- 0.15
 B = 2.83 +- 0.28

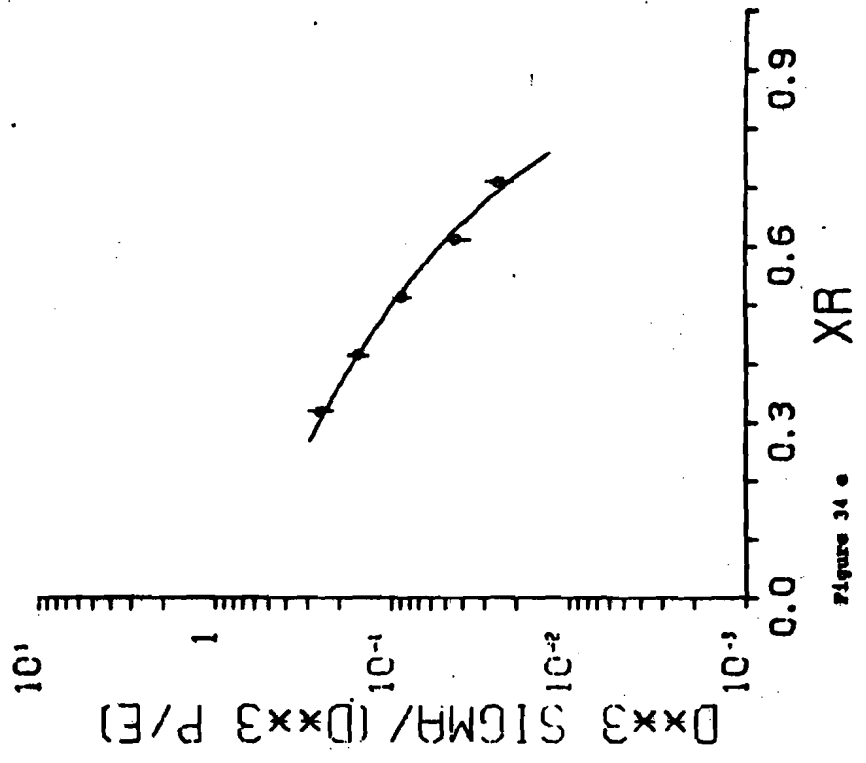


Figure 34 a

P1.P PBEAM= -175 -105-
 +- P PERP = 0.300
 FIT: A*(1-XR) **B
 A = 0.96 +- 0.14
 B = 2.90 +- 0.24

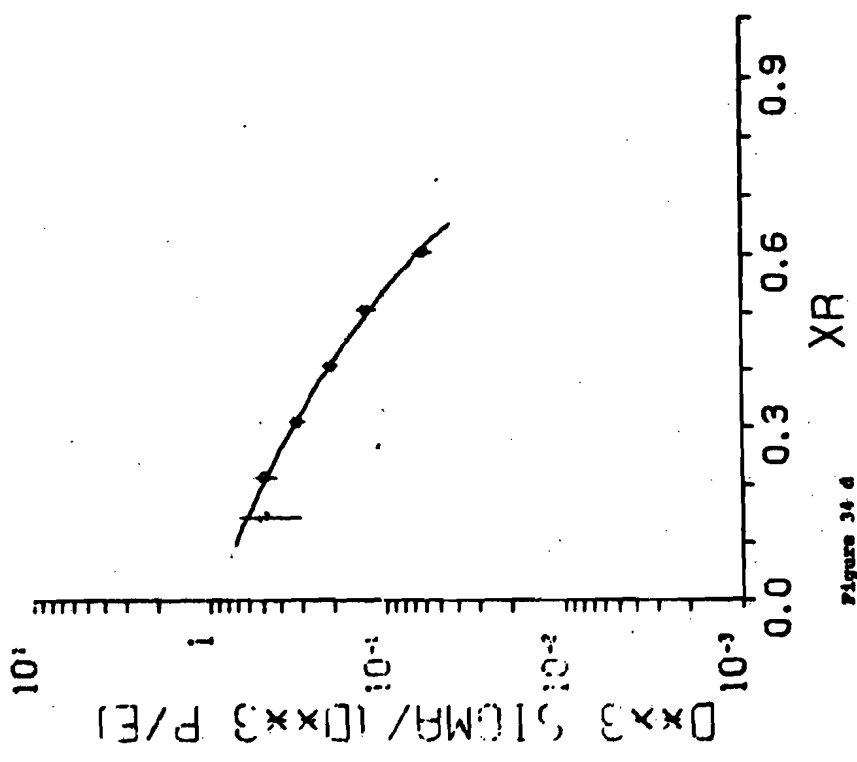


Figure 34 b

K.PI PBEAM=175 -187-

-- P PERP= 0.300

FIT: $A \times (1 - XR)^{-B}$

A = 8.14 +- 2.32

B = 3.29 +- 0.51

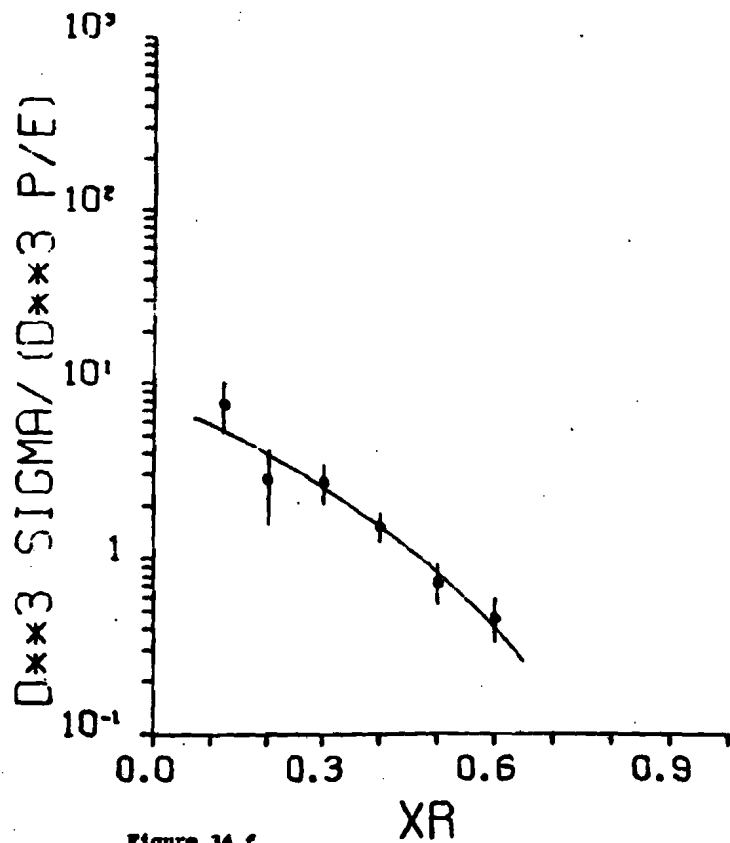


Figure 34 z

K.PI PBEAM=175 -188-

-- P PERP= 0.500

FIT: $A \times (1 - XR)^{-B}$

A = 4.99 +- 1.77

B = 2.76 +- 0.55

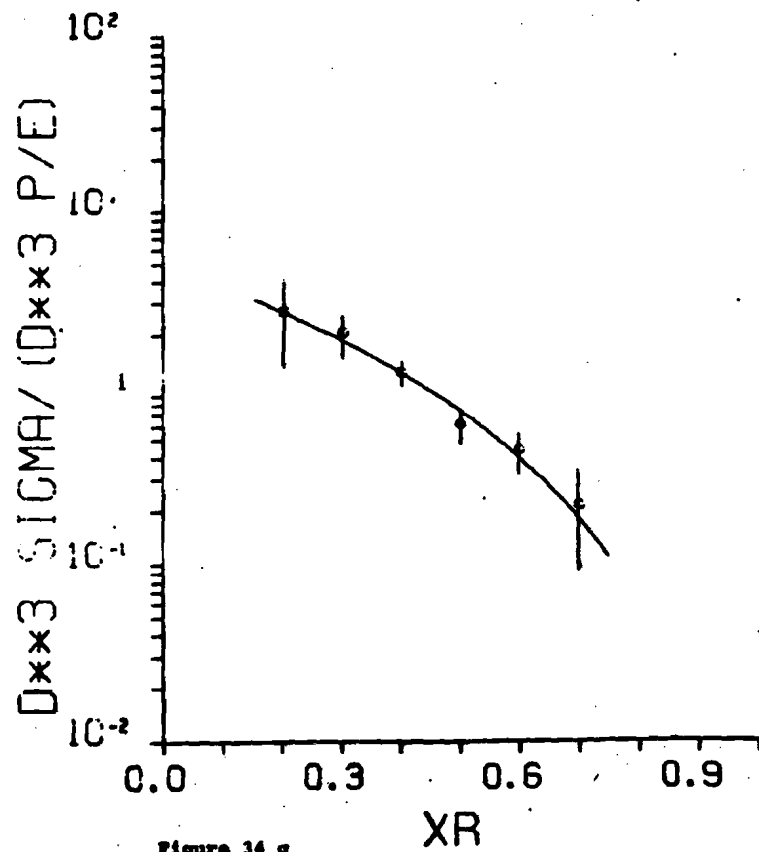


Figure 34 y

-189-

P.PI PBEAM=100
-- P PERP=0.500

FIT: A*(1-XR)**B
A = 7.52 +- 1.42
B = 4.85 +- 0.36

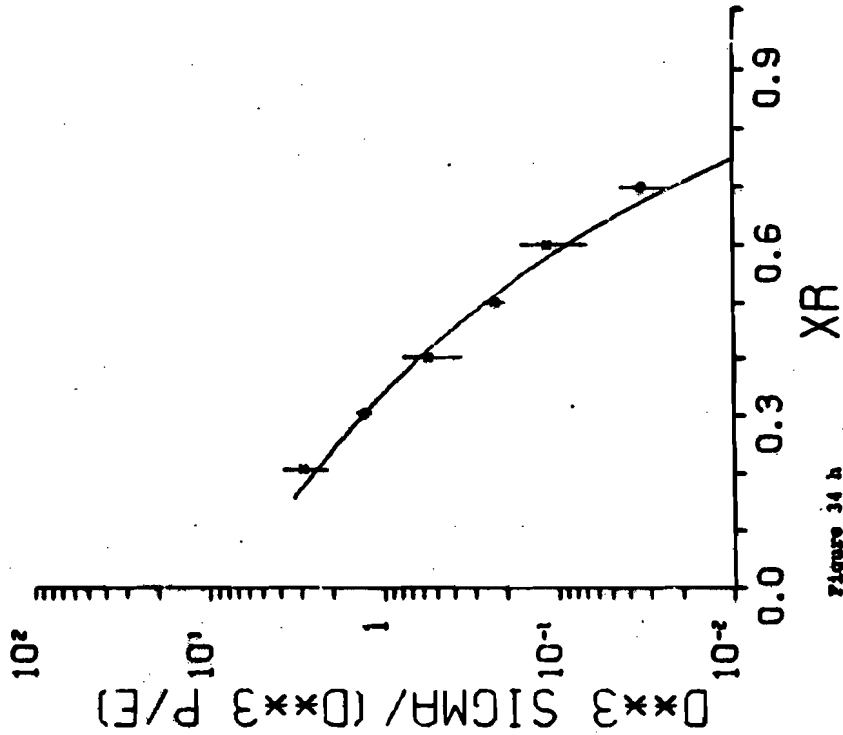


Figure 34 b

-190-

P.PI PBEAM=-100
-- P PERP=0.500

FIT: A*(1-XR)**B
A = 8.16 +- 4.23
B = 4.80 +- 1.10

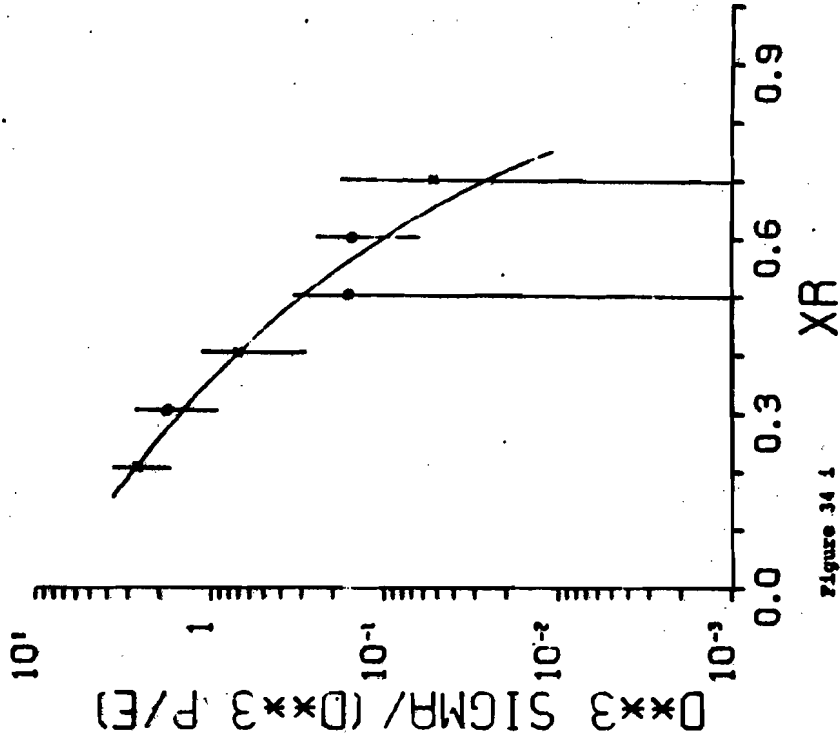


Figure 34 a

P.PI PBEAM=100
 ** P PERP=0.300
 FIT: A*(1-XR)**B
 A = 19.60 +- 1.17
 B = 3.48 +- 0.10

-191-

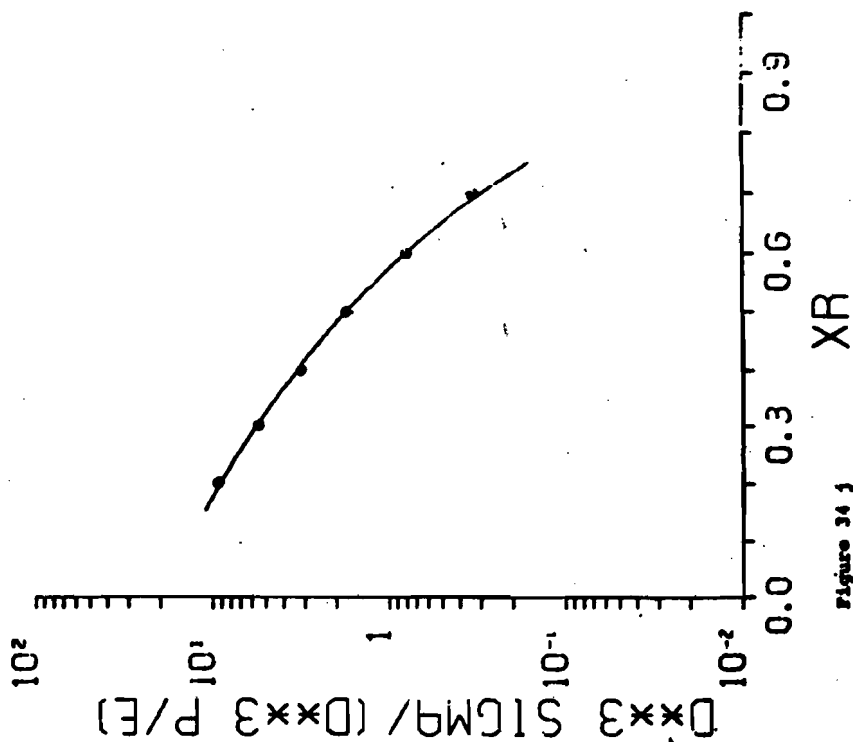


Figure 34 J

P.PI PBEAM=100
 ** P PERP=0.500
 FIT: A*(1-XR)**B
 A = 7.44 +- 0.60
 B = 3.30 +- 0.13

-192-

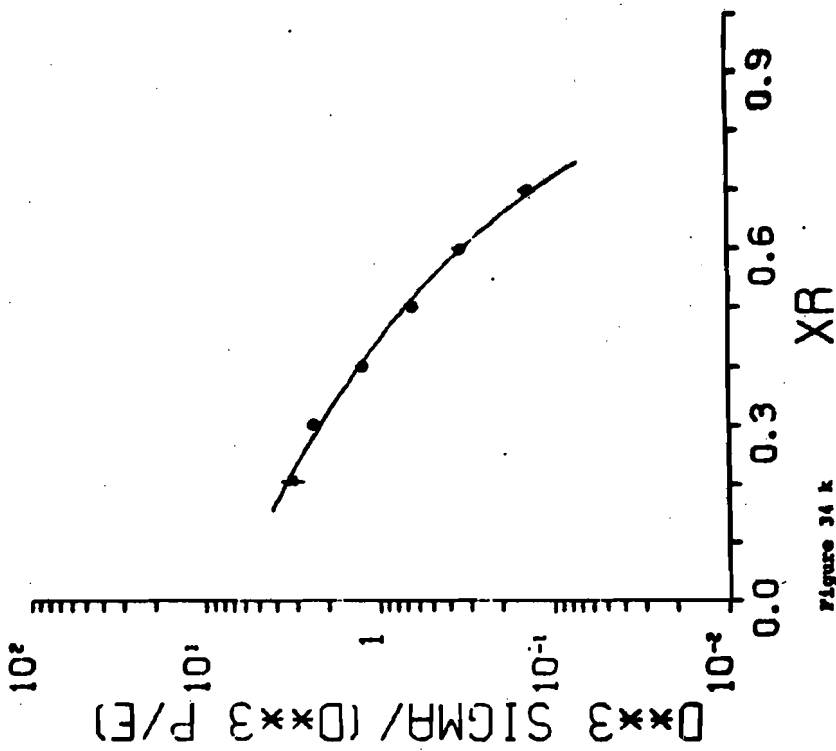


Figure 34 K

-193-

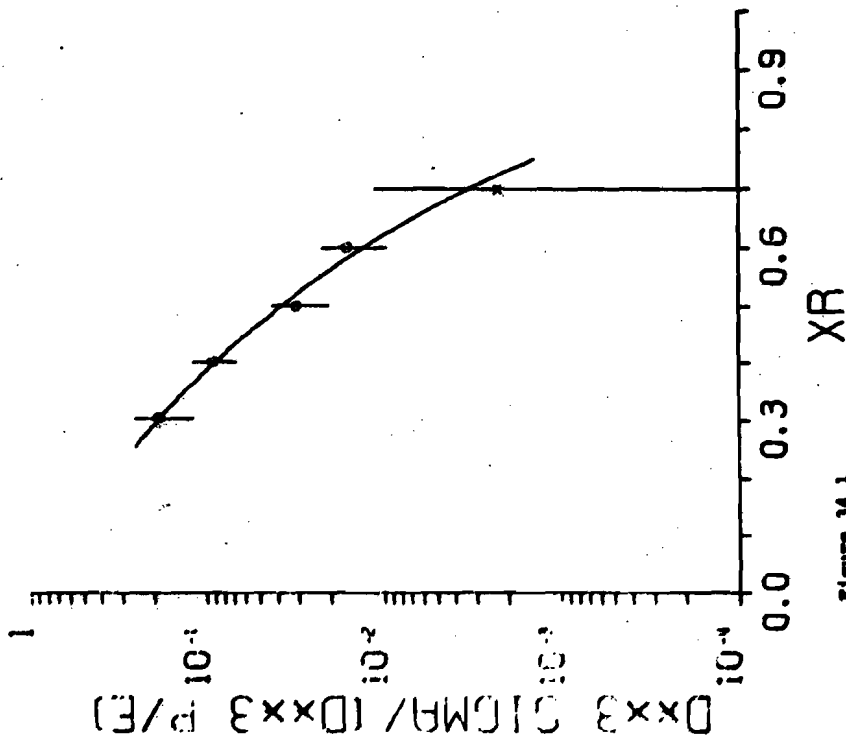
P.K PBEAM=100

+ P PERP=0.300

FIT: A*(1-XR)**B

A = 1.05 +- 0.64

B = 4.78 +- 0.99



-194-

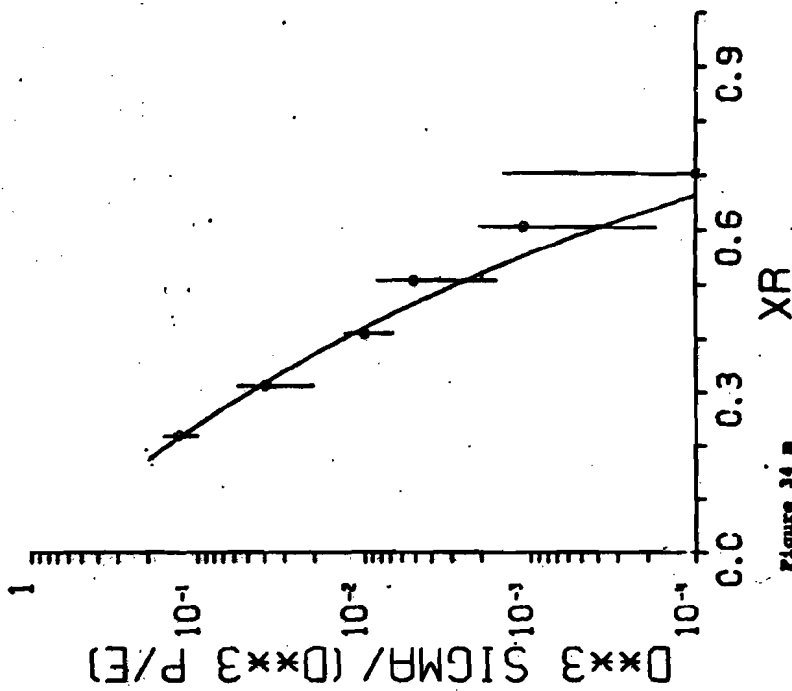
P.P PBEAM=175

+ P PERP=0.500

FIT: A*(1-XR)**B

A = 0.98 +- 0.48

B = 8.49 +- 1.24



P.P PBEAN=175
 +- P PERP=0.300
 FIT: $A \ln(1-XR) + B$
 A = 1.56 +- 0.40
 B = 0.40 +- 0.57

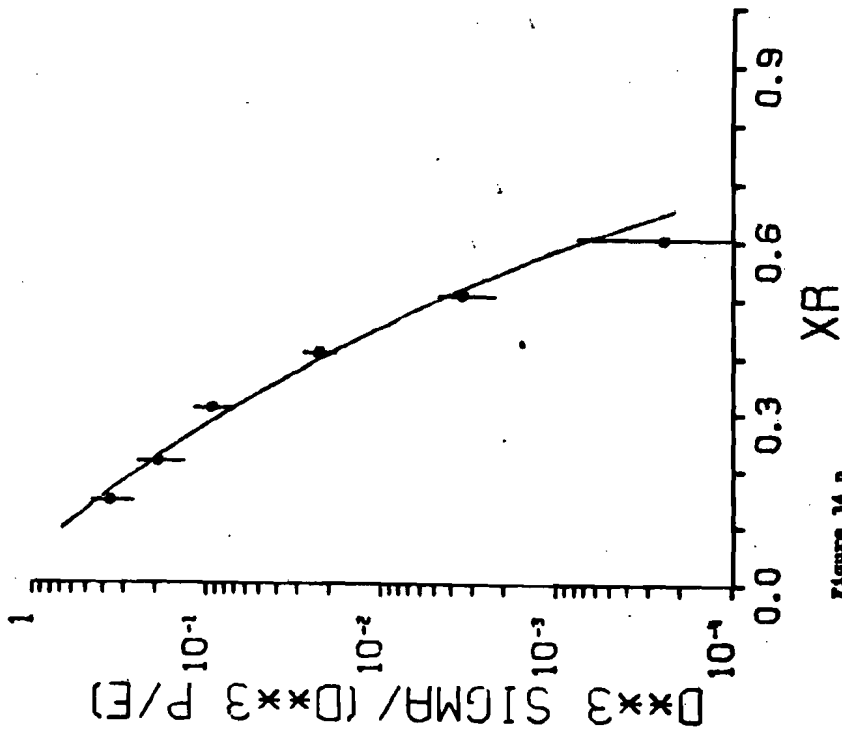


Figure 34 n

-196-

Table IV: $(1 - x^2)^B$ Plus

Minimum Pre- Dilution For B	Quark Epoch k	Incl- denc Energy GeV/c	100	175	-100	-175
1	1	1	1.39 ± .25	1.72 ± .35	1.05 ± .20	1.42 ± .20
3	3	3	1.07 ± .07	1.03 ± .27	1.93 ± .25	1.05 ± .18
5	5	5	1.39 ± .25	1.43 ± .30	1.05 ± .20	1.42 ± .20
1	1	1	1.98 ± .18	1.41 ± .50	2.56 ± .16	2.39 ± .21
3	3	3	2.82 ± .51	2.75 ± .55	2.68 ± .47	2.80 ± .16
5	5	5	1.98 ± .28	1.41 ± .50	2.03 ± .26	2.74 ± .41
1	1	1	2.29 ± 1.4	2.92 ± 1.8	1.97 ± 1.09	3.35 ± 1.8
3	3	3	3.28 ± .23	3.56 ± .10	3.50 ± .70	3.61 ± .53
5	5	5	3.48 ± .10	3.56 ± .10	3.31 ± .27	3.61 ± .53
1	1	1	2.85 ± .37	3.22 ± .33	2.93 ± 1.1	4.20 ± 2.5
3	3	3	2.36 ± .41	2.75 ± .22	3.46 ± .08	4.34 ± .91
5	5	5	2.85 ± .37	3.22 ± .33	3.46 ± .08	4.34 ± .91

Table V: $(1 - x_B)^2$ Fits

Reactions With Charge Exchange

Minimum Prediction for B Quark Exch. Gluon Exch.	Inci- dent Energy GeV	p_1 GeV/c	v^+k^+	v^+p^+	k^+n^+	k^+k^+	p^+p^+	v^+k^+	p^+p^+
			5 7	5 5	5 7	5 7	5 5	7 9	9 11
+100	.3		2.13± .17	2.69± .20	2.12± .23	3.06±1.24	4.34± .16	4.79± .90	7.81±3.4
	.5		2.00± .40	3.47± .70	3.37±1.4		4.83± .36	7.02±6.0	
+175	.3		2.19± .57	3.29± .40	3.29± .51	4.11±1.59	4.40± .09	5.48± .34	8.41± .57
	.5		2.27± .20	3.61± .51	3.51± .54	4.13±2.54	4.56± .11	5.43 .57	8.49 1.24
-100	.3		1.73± .13	2.69± .15	2.07± .22	2.77±1.37	3.42± .44		
	.5		1.85± .19	2.22± .20	2.70± .50		4.78±1.1		
-175	.3		2.86± .23	2.90± .24	4.34± .66	5.54±1.6	3.77± .79	4.27±2.6	

-197-

Table VI: Integrated Cross Sections $-(1 - x_B)^2$ Fits

Minimum pre- diction for B Quark Exch. Gluon Exch.	Inci- dent Energy GeV	v^+k^+	v^+p^+	k^+n^+	k^+k^+	p^+p^+	v^+k^+	p^+p^+
		5 7	5 5	5 7	5 5	5 5	7 9	9 11
+100		1.44± .24	1.90± .19	3.21± .76		2.52± .40		
		1.47± .20	1.13± .30	3.09± .01	3.37± .13	2.89± .22		
+175		1.40± .31	2.20± .18	2.82± .50	2.37± .61			
		1.26± .36	2.23± .24	2.56± .90	2.88±1.0			
-100		2.32± .63	3.44±1.2	3.16± .08	5.00± .42			
		1.88± .31	2.56± .33	2.75± .04	4.86±4.71			
-175								

-198-

power for this reaction is 3, whereas the quark exchange minimum is predicted to be 5. However, the source of discrepancy in the other reactions has not been isolated.

This model is the most complete of the three discussed here. It makes predictions for all the reactions with the exception of those with a leading particle effect. In these latter cases, the diffractive contributions to the cross section complicate the fragmentation analysis.

V. DISCUSSION

We have seen that this experiment has provided a wealth of data in the low p_T beam fragmentation region. This is the first time that high energy data of high statistical accuracy has been made available for a variety of beam particles other than protons. For example, p_T distributions as a function of x_T are now available for 36 different reactions. Many theories now make predictions only for distributions integrated over p_T . This new data provides input to new models which may include a p_T dependence. Furthermore, scaling has now been shown to be valid within 5% for pion and kaon induced reactions.

As for the models we have tested, the results are encouraging. The model of Andersson, *et al.* seems to describe meson fragmentation well, if minor changes are made. This model employs a set of phenomenological functions and is less appealing, in a sense, since the details of the actual hadron-hadron scattering process are hidden. In addition the assumptions of the model are introduced in a rather ad hoc manner. Also the case of baryons in fragmentation processes, both as fragments and as projectiles, have not yet been tested since no detailed predictions have been made. Here our data can serve as a guide. If we believe this model, we can use our distributions to determine both the D_q^{proton} and the D_q^{meson} functions.

The model of Das and Iwa makes specific assumptions about

the fragmentation process. Furthermore, this model is sensitive to the quark distributions in the incident hadron and allows us to determine these also. These quark distributions, it should be noted, are not necessarily those of the quiescent hadron. Many $q\bar{q}$ pairs can be made during the interaction process, some of which can recombine to make the observed meson. The drawback of this model is the fact that it describes only the two-body recombination. An interesting extension will be one which allows the production of baryons.

The Brodsky and Gunion model is interesting in that it makes predictions about the exact nature of the interaction. Our data show overwhelmingly that quark exchange or annihilation is the dominant process. However, it remains to be understood whether our data which have powers of $(1-x)$ which are lower than the minimum predicted are evidence of the breakdown of the model or whether other processes, besides fragmentation, are in effect.

These three models each focus on a different part of the hadron-hadron interaction. The Brodsky and Gunion model focuses on the actual interaction mechanism. The model of Andersson et al. really describes the final state interaction. The Das and Hwa picture is sensitive to the quark distribution in the incident hadron. A complete picture would unify all three concepts.

All three of these models focus on the quark content of the hadrons. These are some of the few models which employ

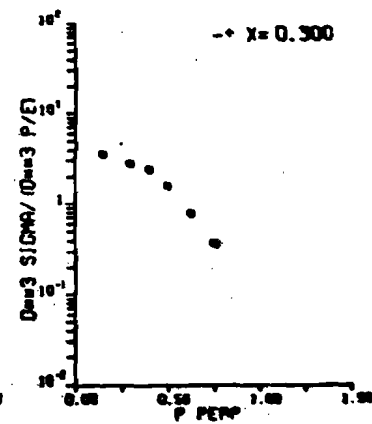
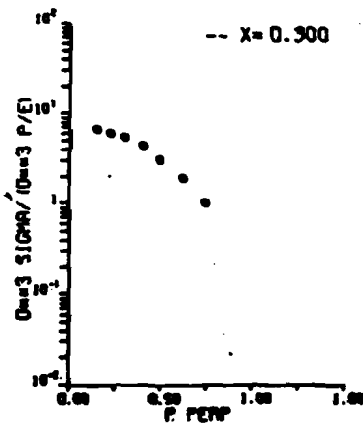
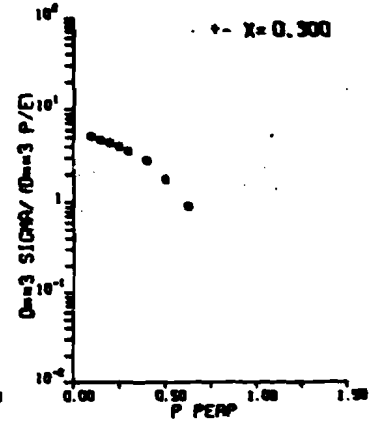
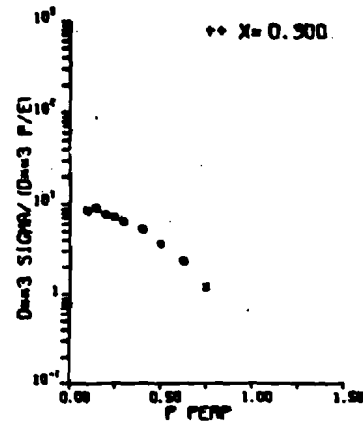
this idea in describing low p_T hadron-hadron collisions. Based on the fairly good agreement between the predictions and data, one can be encouraged to believe that there may be some unifying principle in describing hadronic and leptonic interactions.

APPENDIX I. Invariant Differential Cross Sections -
 P_T Dependence

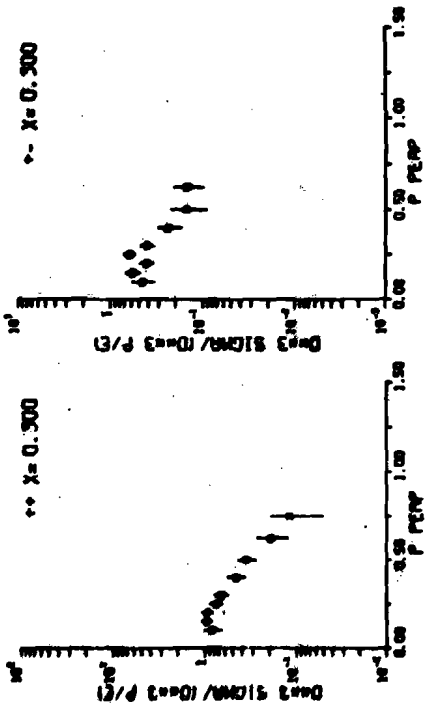
This appendix contains additional plots of invariant differential cross sections as a function of P_T for x_R values of 0.3 and 0.6. The symbols denote

- x unaveraged cross sections (data taken at only one sign of the AVB angle)
- o averaged cross sections (data taken at both signs of the AVB angle)

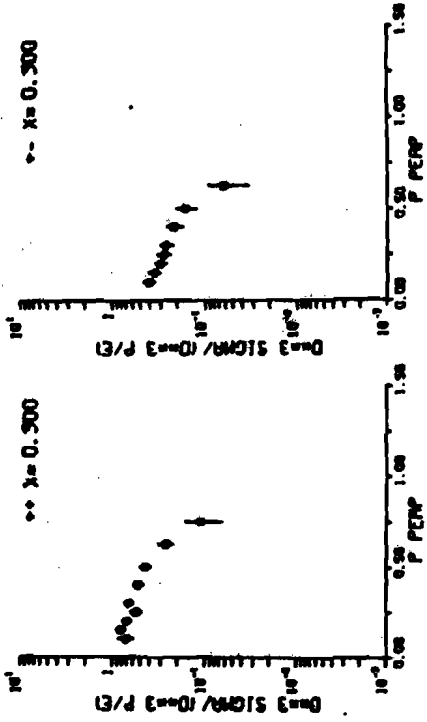
The units are mb/GeV^2 .



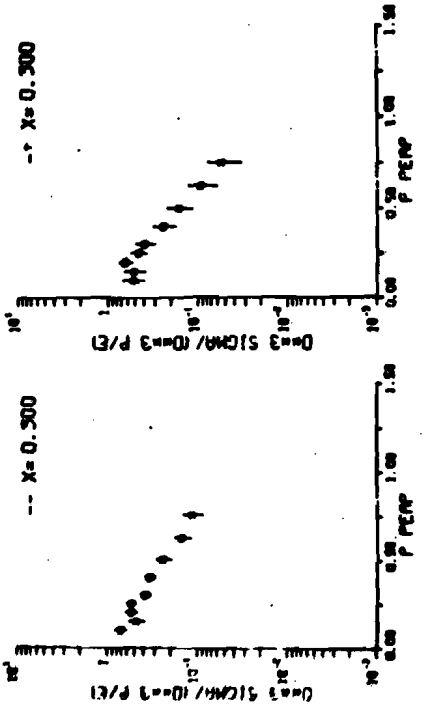
PI.A FBEM=100



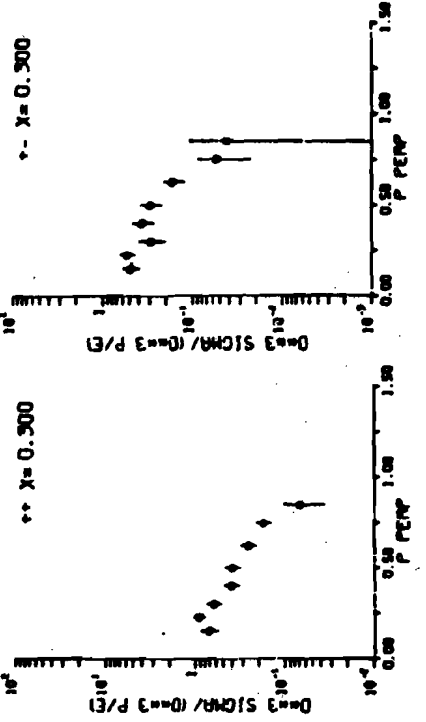
PI.F FBEM=100



PI.K FBEM=100

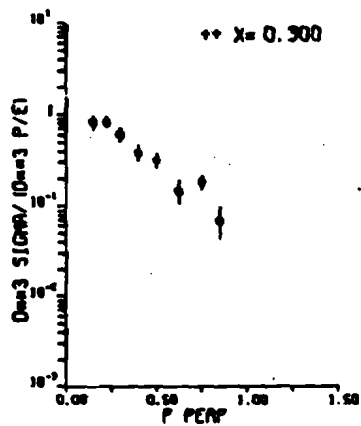
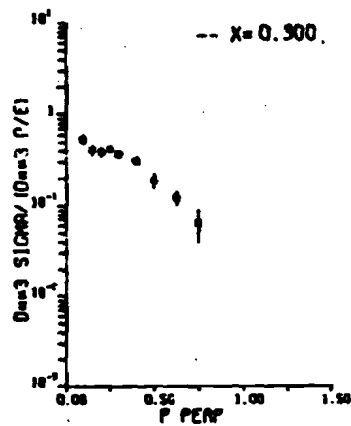


PI.K FBEM=175

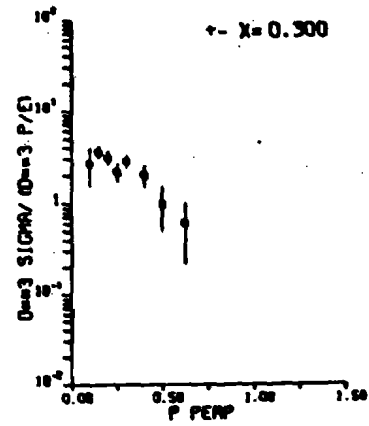
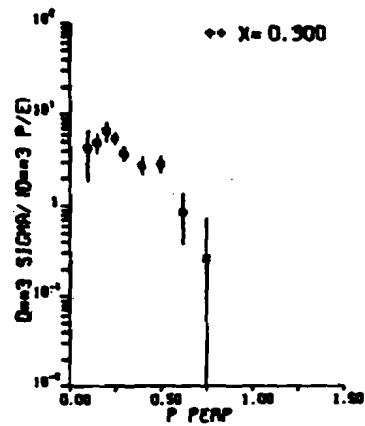


PI.P PBEAM=-100

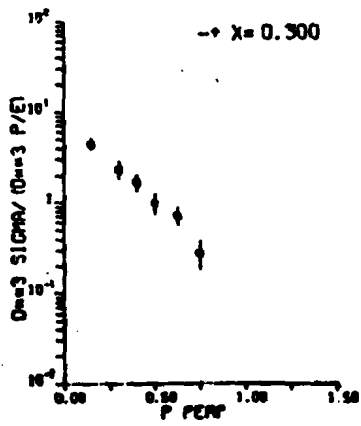
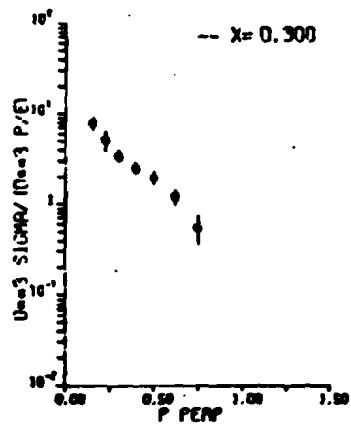
PI.P PBEAM=175



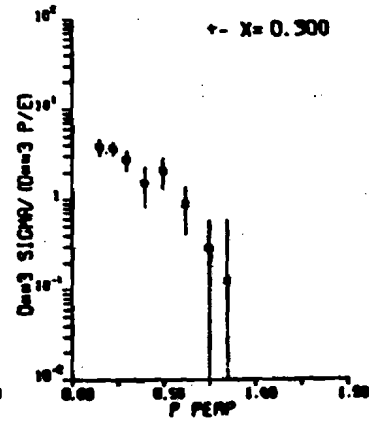
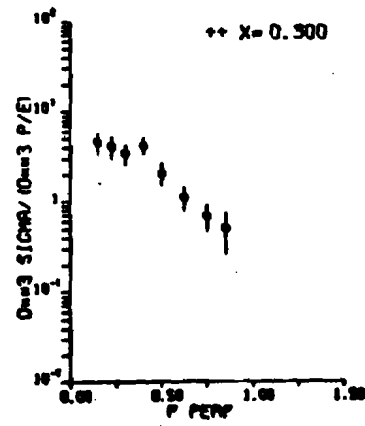
K.PI PBEAM=100



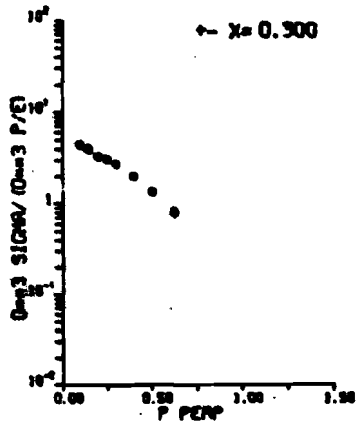
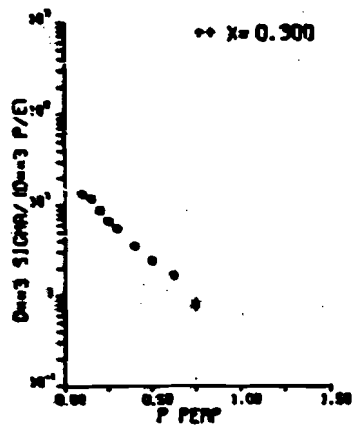
K.PI PBEAM=-175



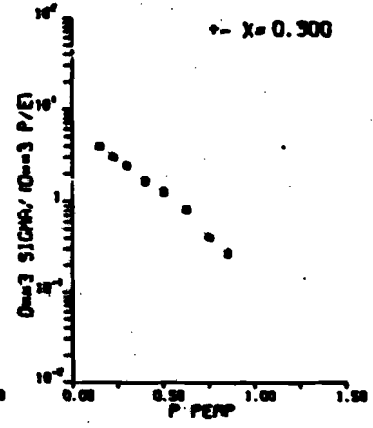
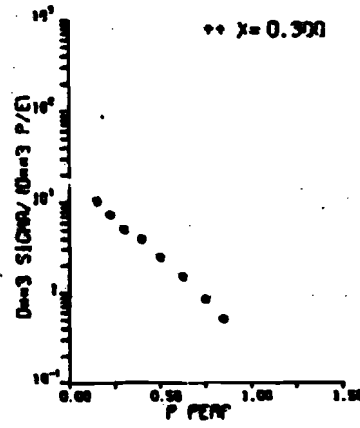
K.PI PBEAM=175



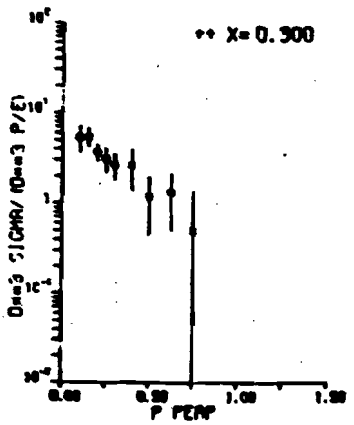
P.P.1 FBEAN=100



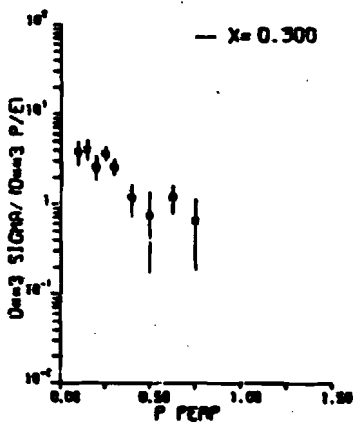
P.P.1 FBEAN=175



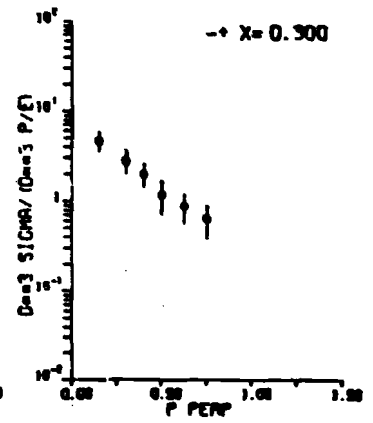
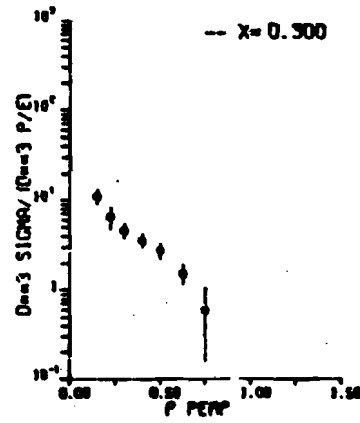
K.K FBEAN=100



K.K FBEAN=-100

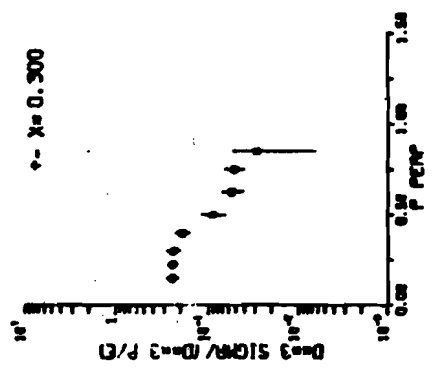
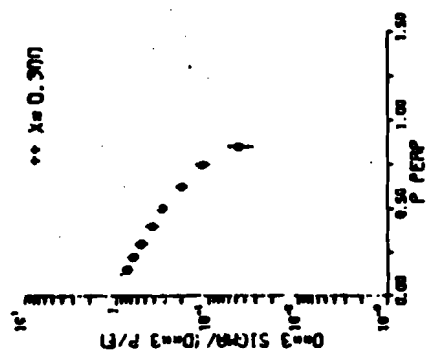


P.P.1 FBEAN=-175



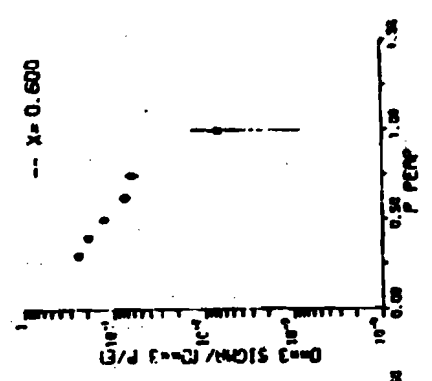
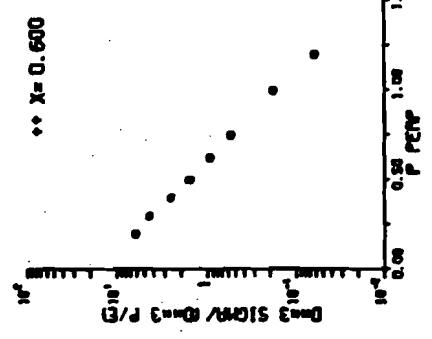
-211-

P.K. PBEAM=175

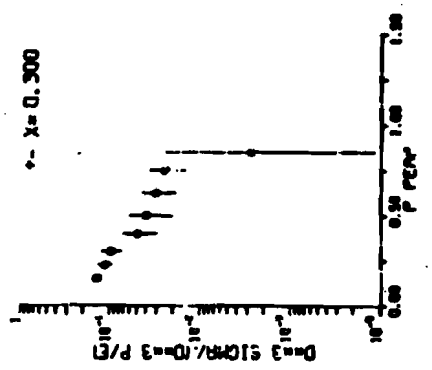
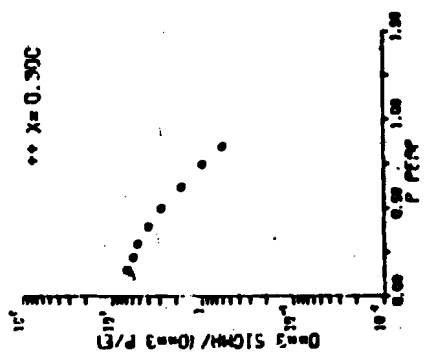


-212-

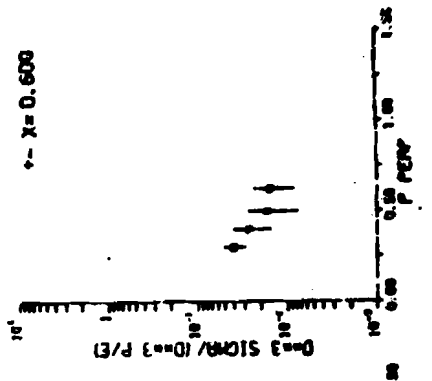
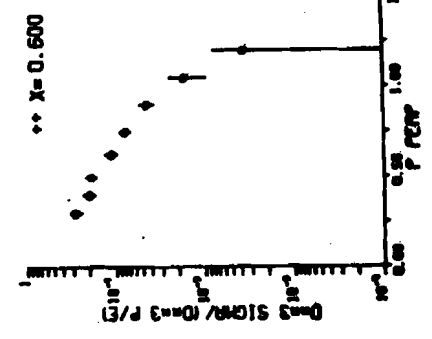
P.I.F. PBEAM=100



P.P. PBEAM=175

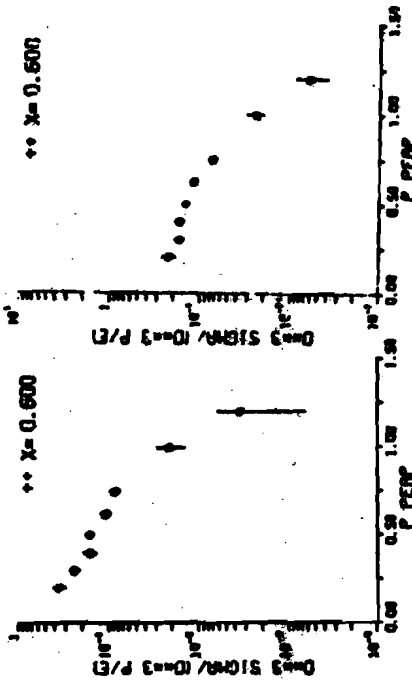


P.I.K. PBEAM=175

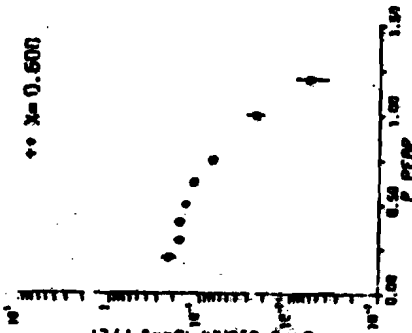


-213-

P1.N FBCEM=100

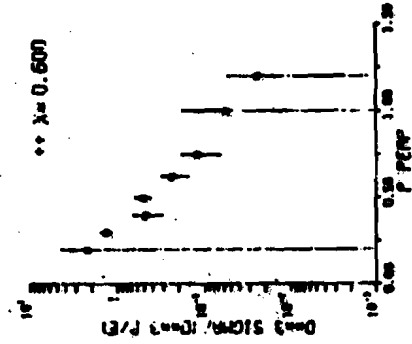


P1.P FBCEM=100

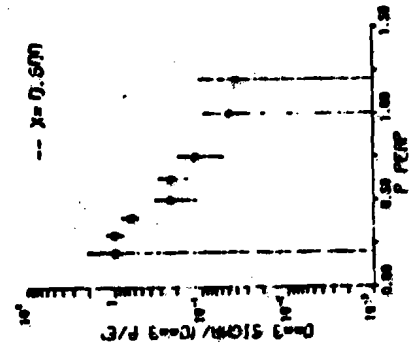


-214-

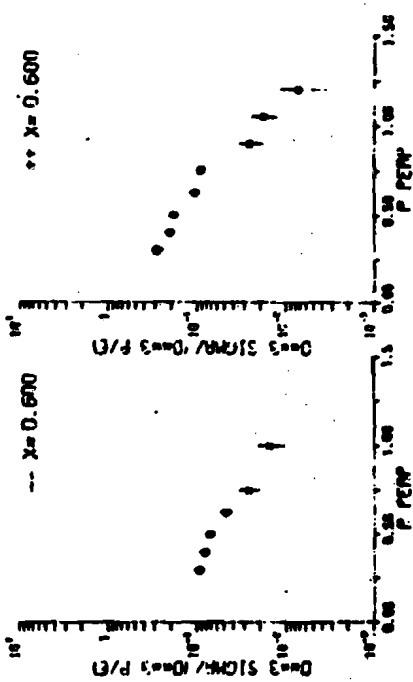
K.P1 FBCEM=100



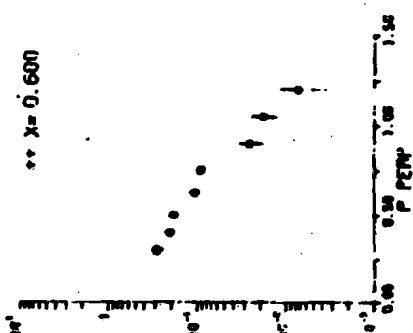
K.P1 FBCEM=170



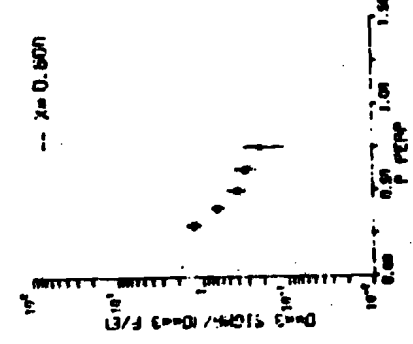
P1.P FBCEM=175



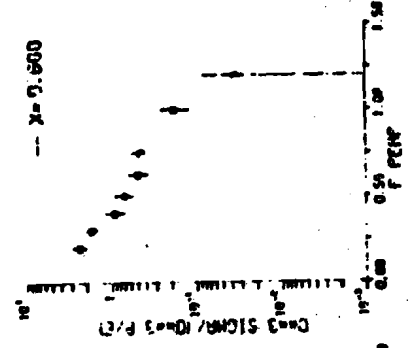
P1.P FBCEM=100

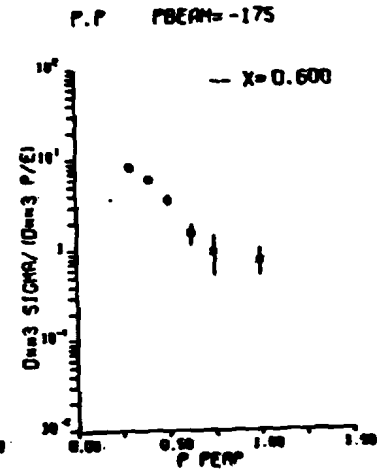
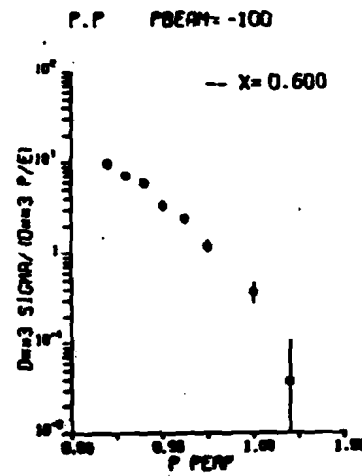
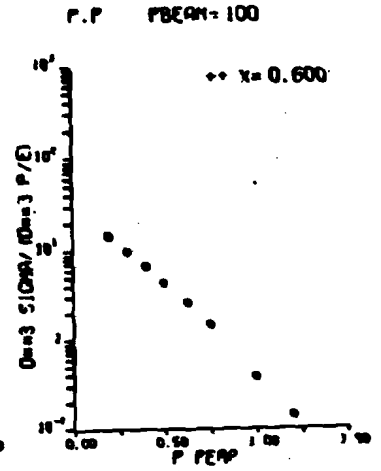
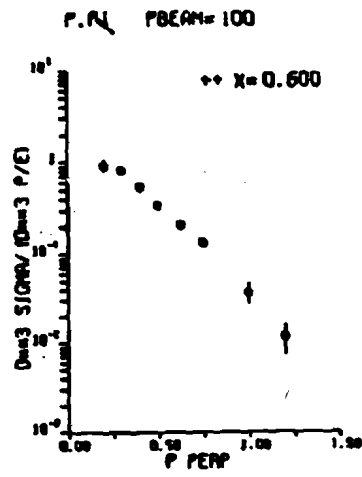
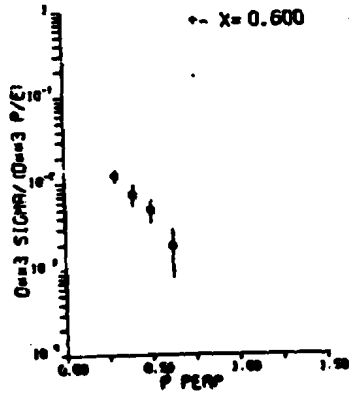
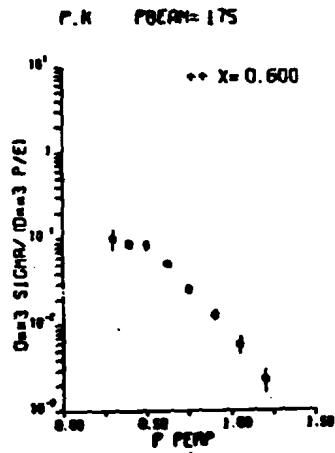
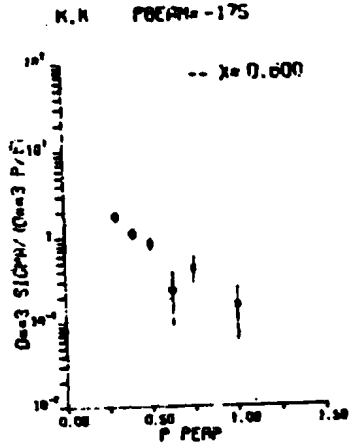
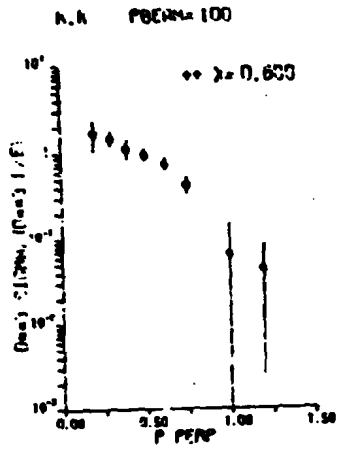


K.N FBCEM=175



K.N FBCEM=100



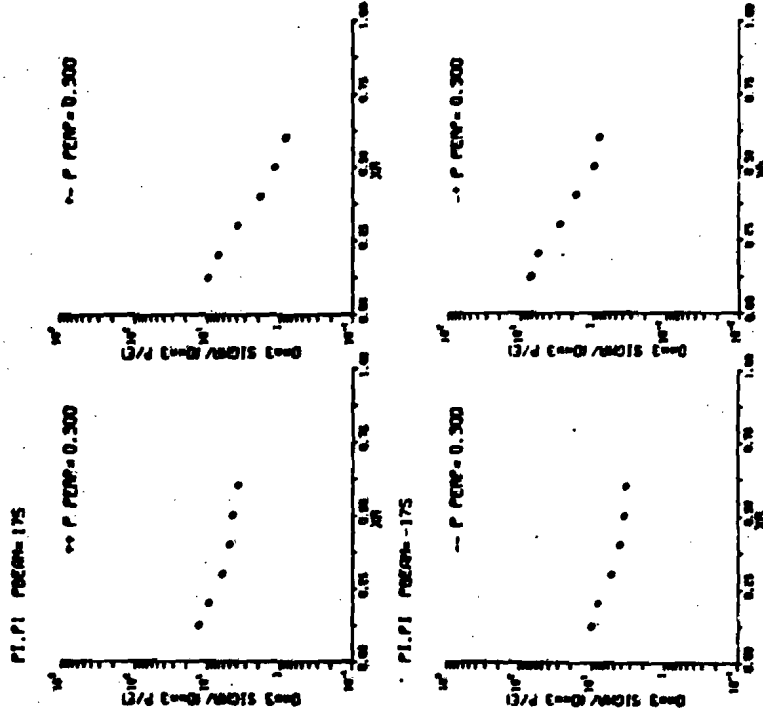


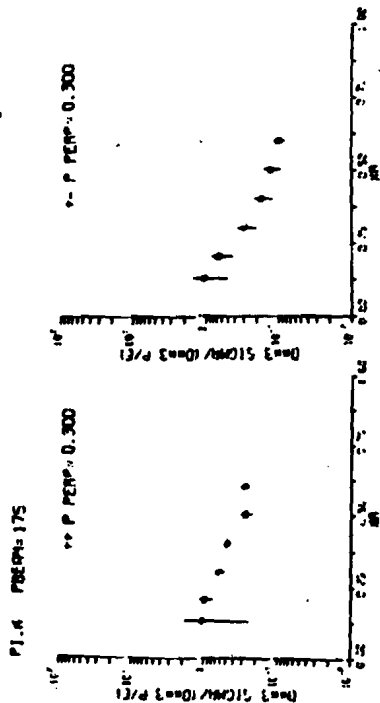
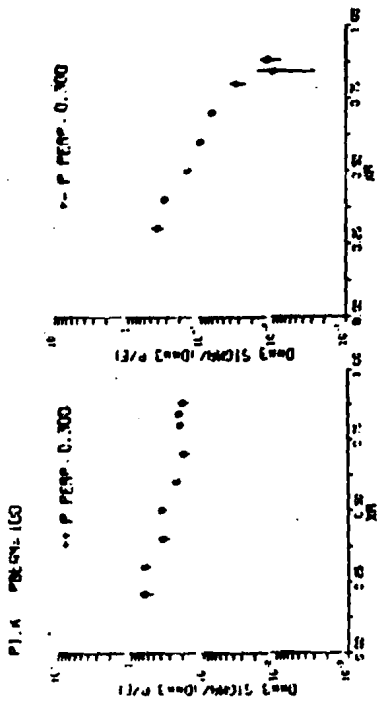
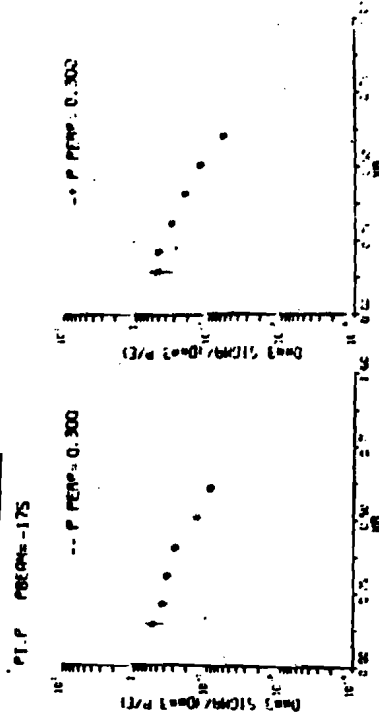
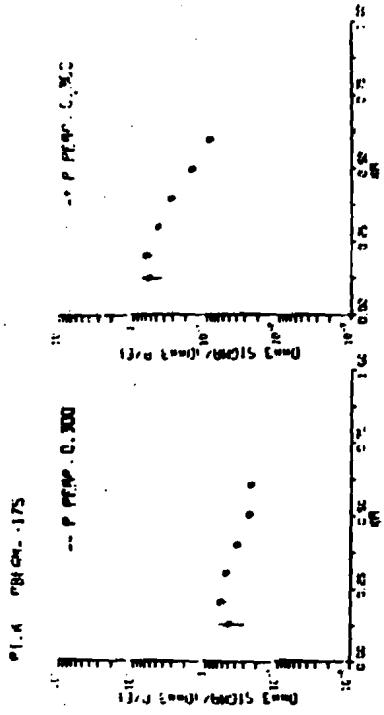
APPENDIX II. Invariant Differential Cross Sections -
 x_B Dependence

This appendix contains additional plots of invariant d
differential cross sections as a function of x_B for P_T values
of 0.3, 0.5 and 0.75 GeV/c. The symbols denote

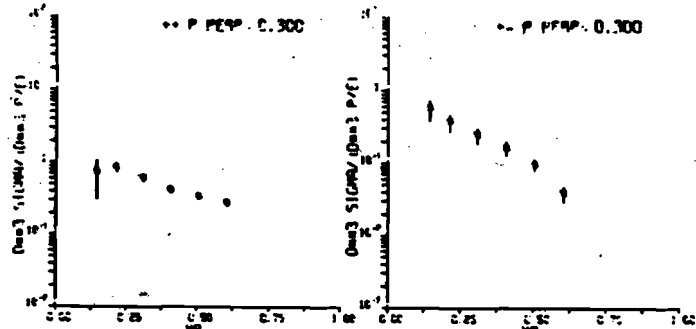
- x unaveraged cross sections (data taken at
only one sign of the AFB angle)
- o averaged cross sections (data taken at
both signs of the AFB angle)

The units are mb/GeV².

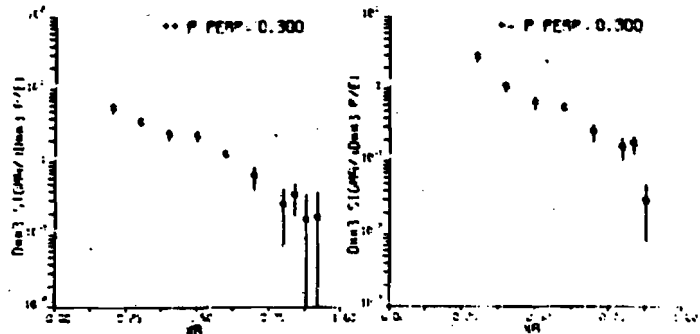




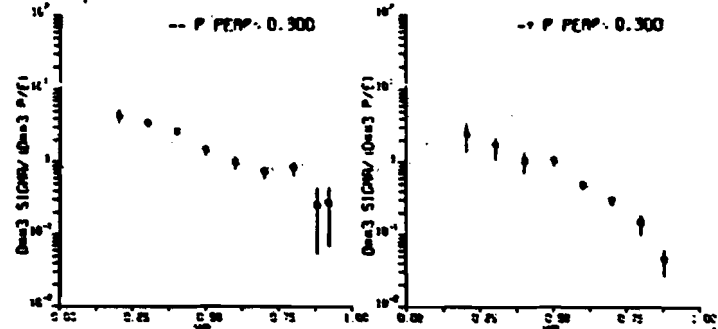
P.I.P. PBECH-175



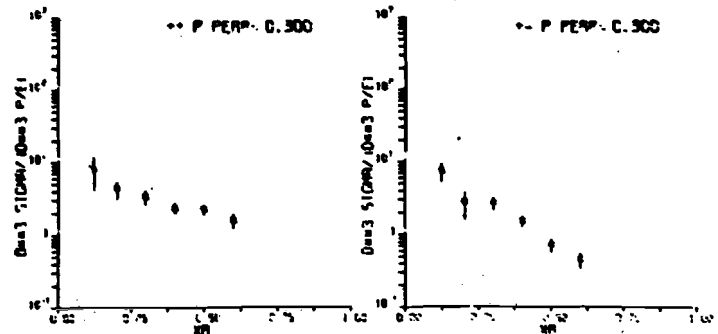
K.P.I. PBECH-100

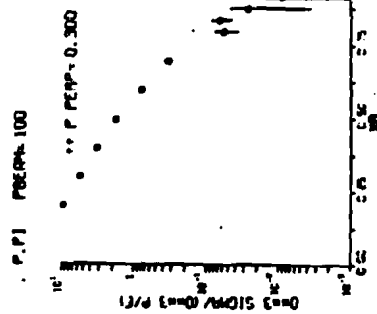
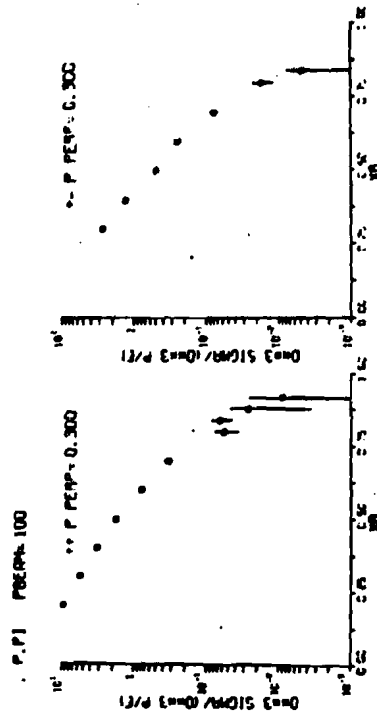
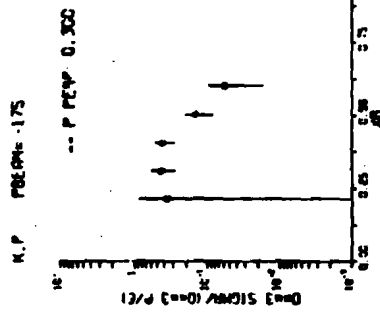
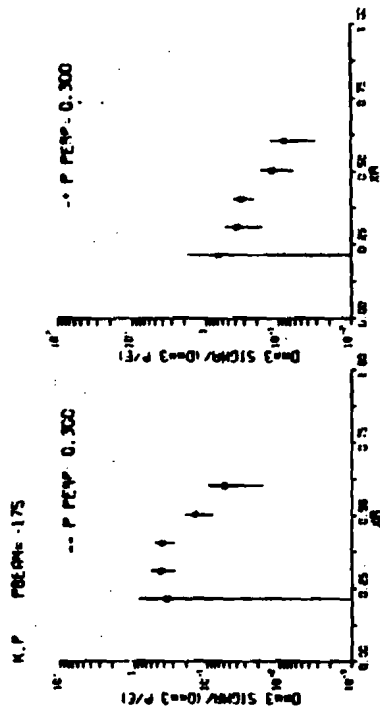
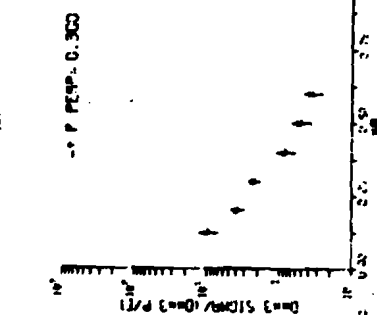
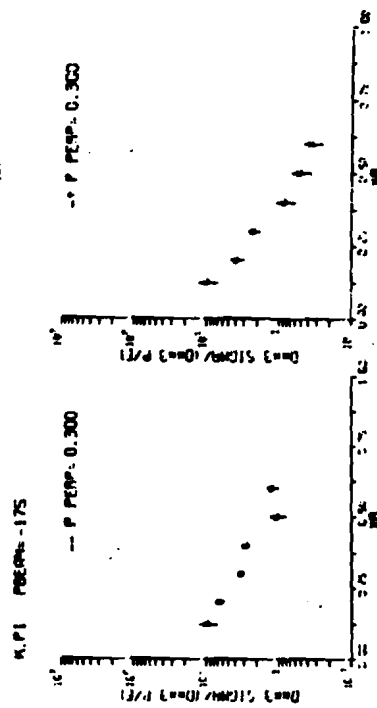
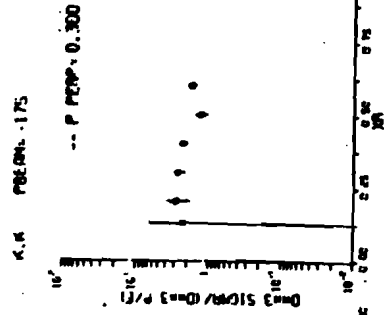
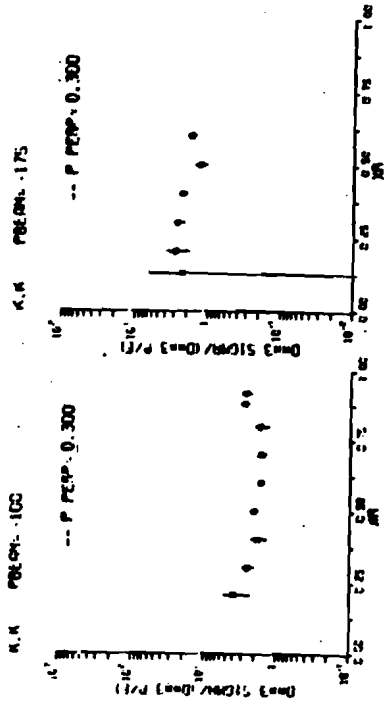


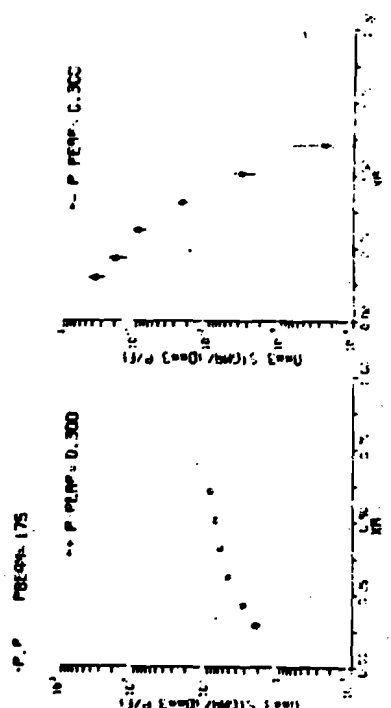
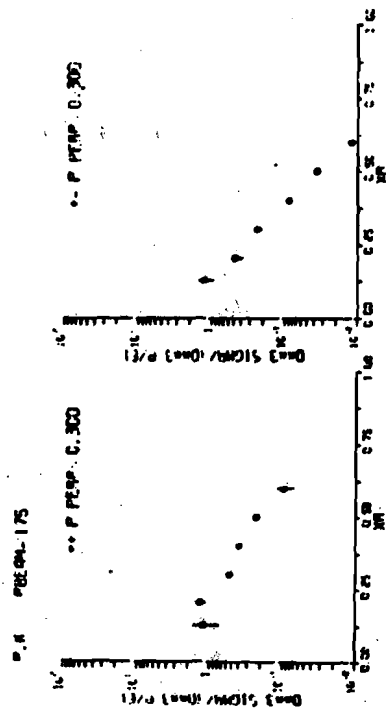
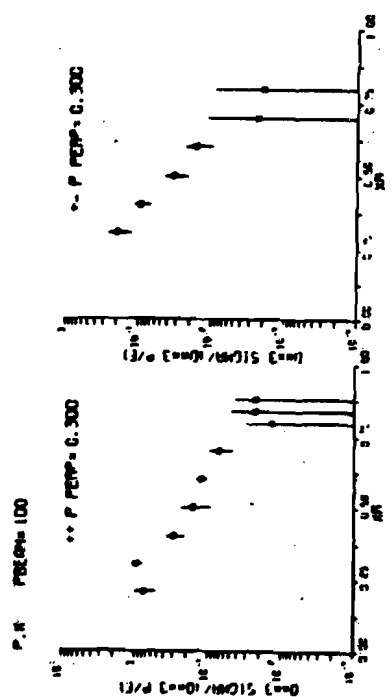
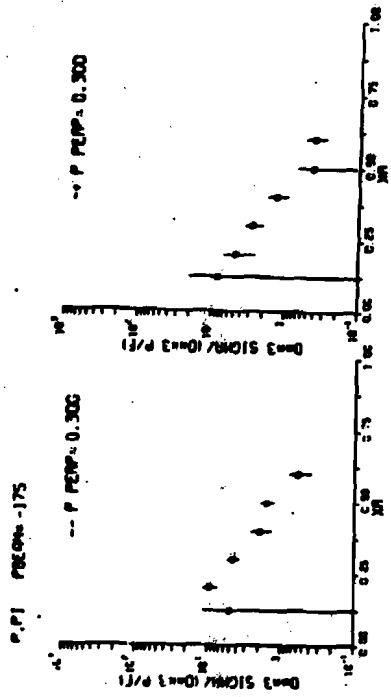
K.P.I. PBECH-100

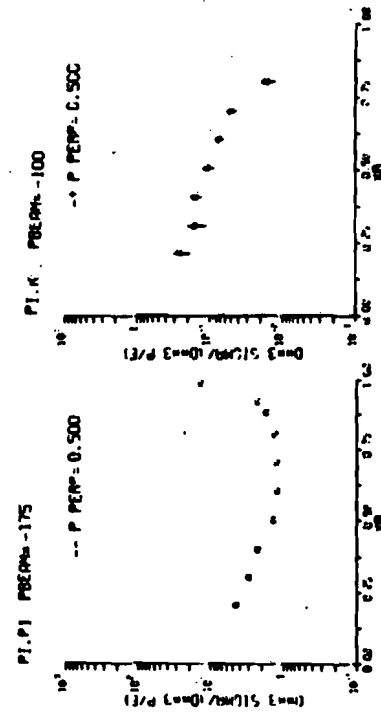
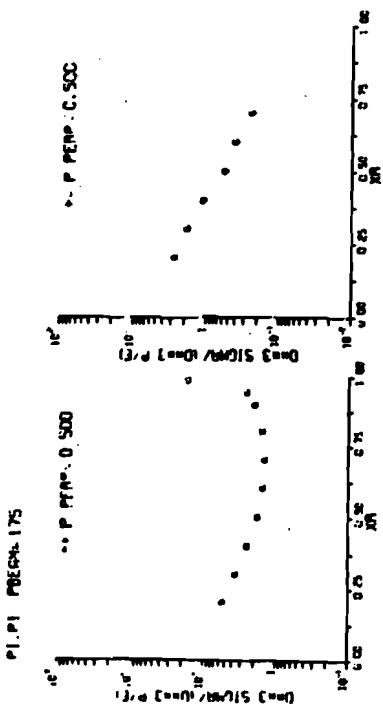
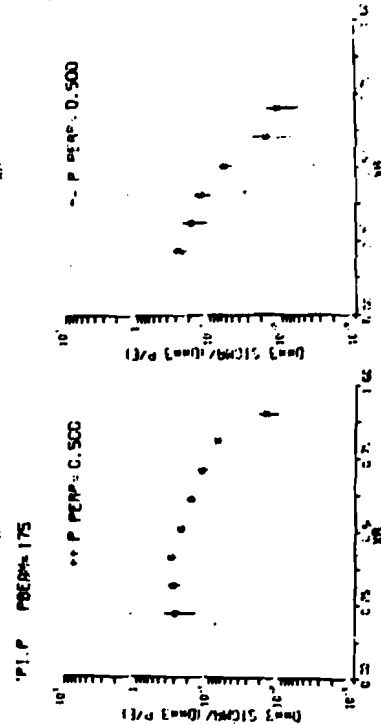
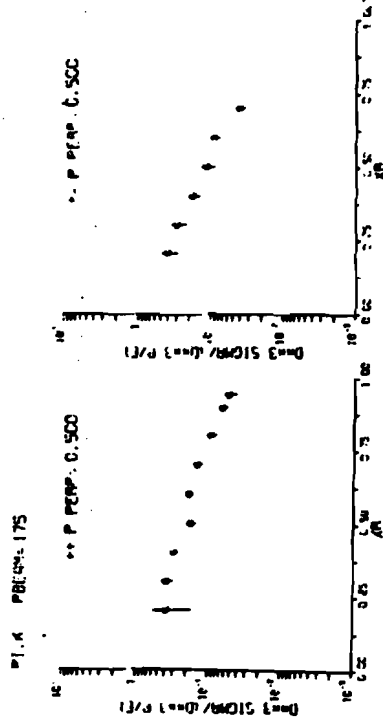


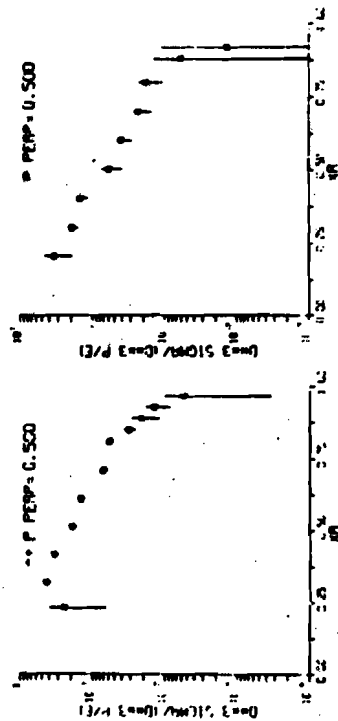
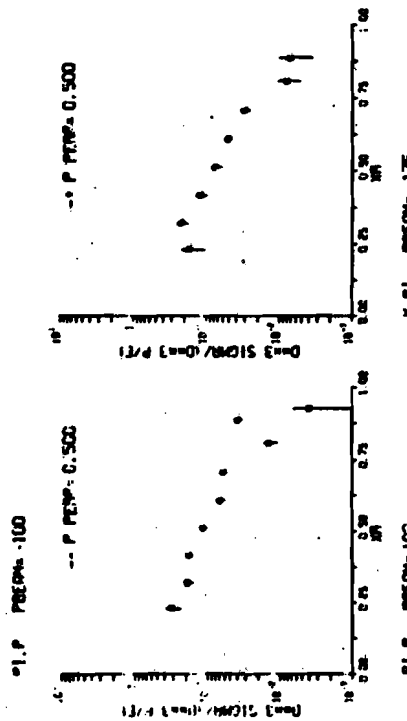
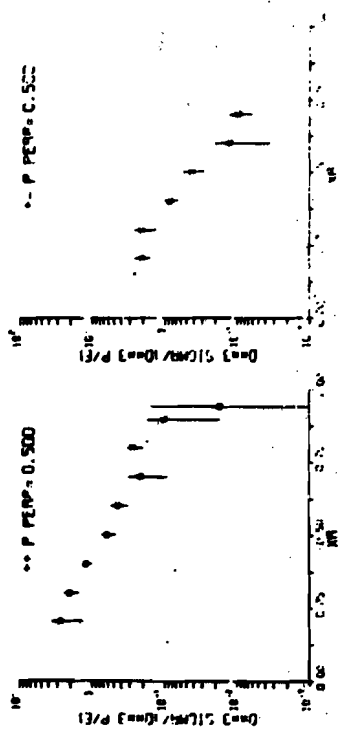
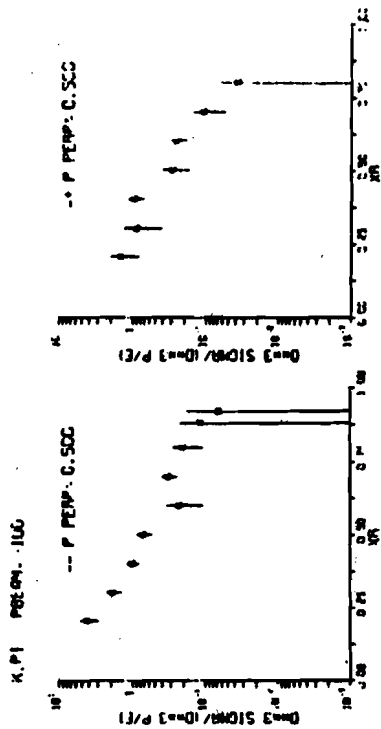
K.P.I. PBECH-175

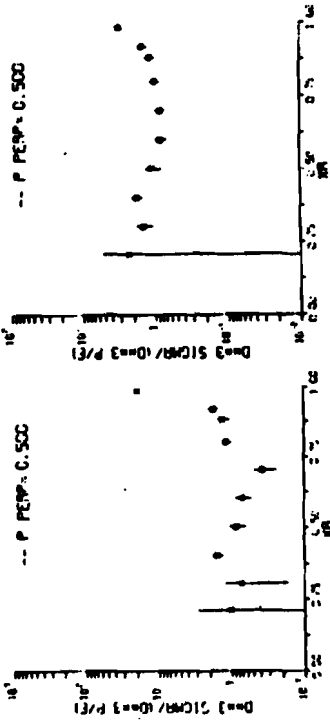
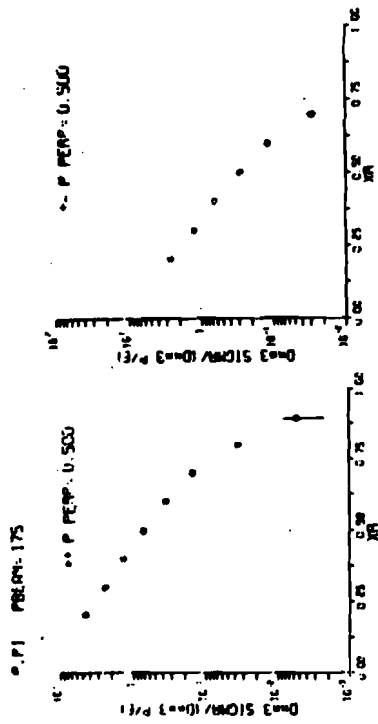
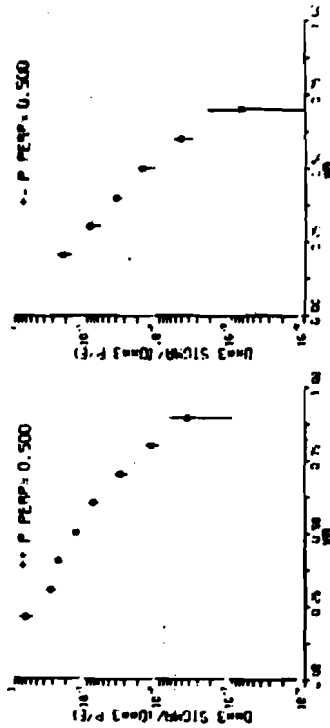
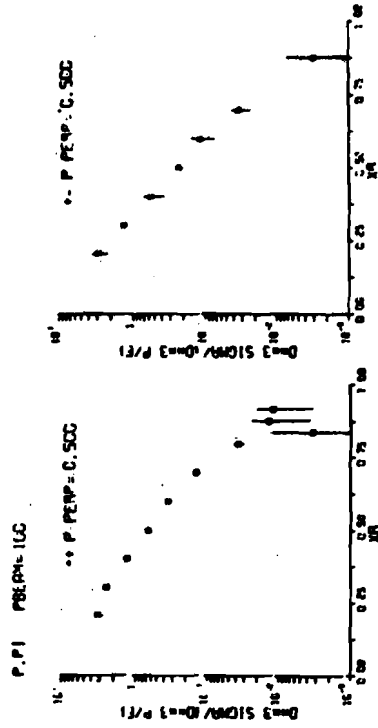


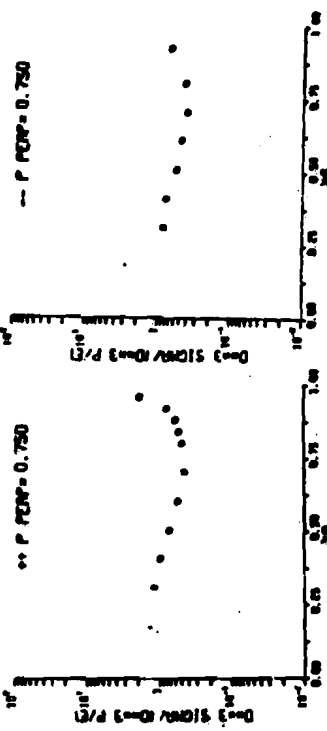
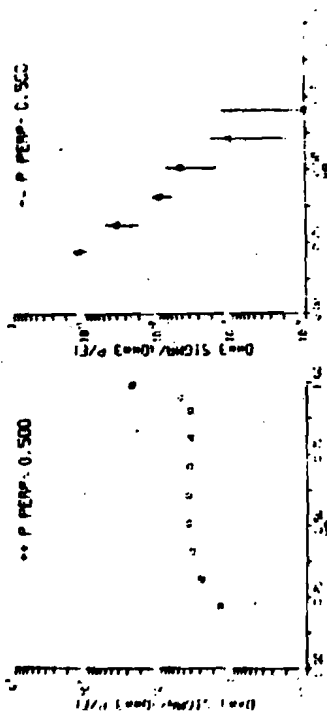
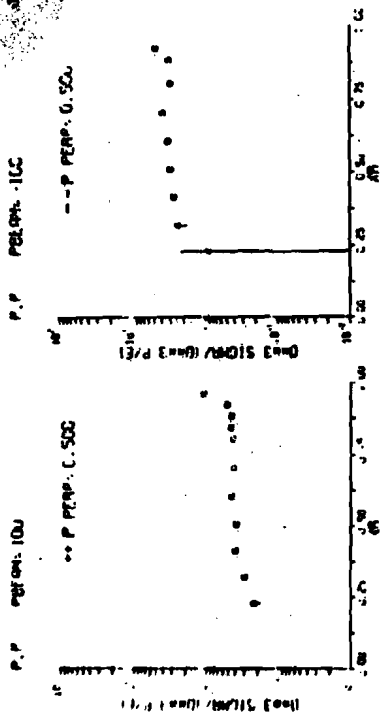


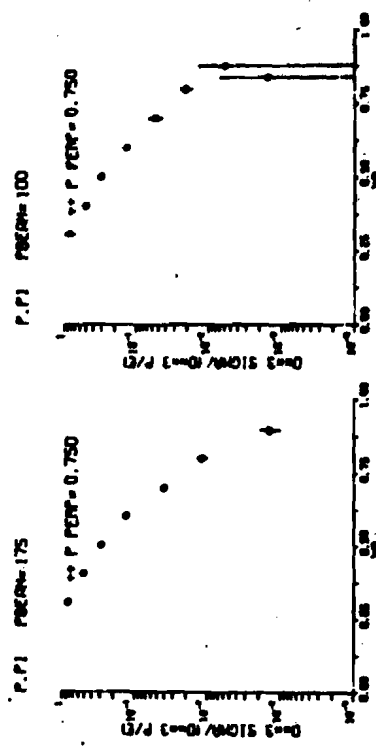
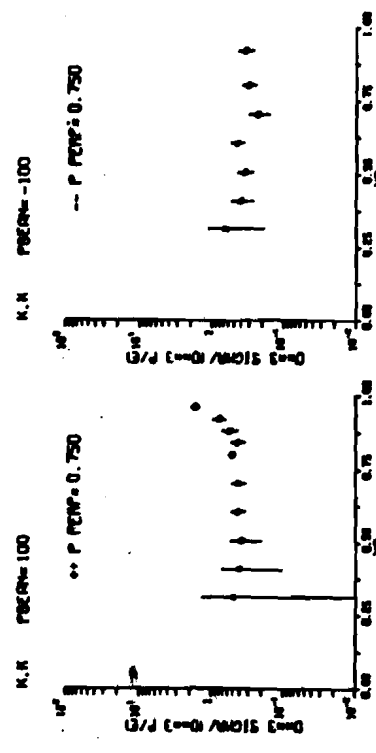
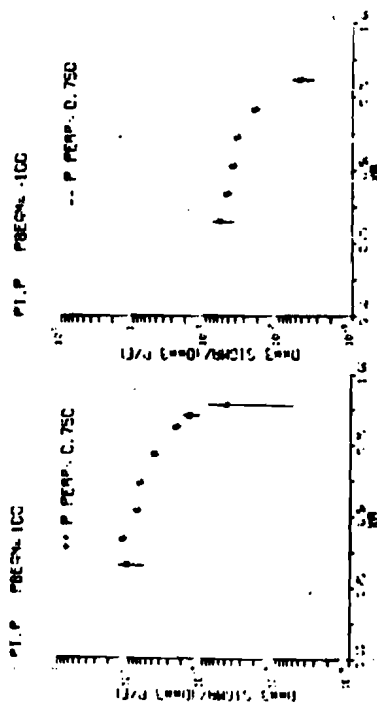
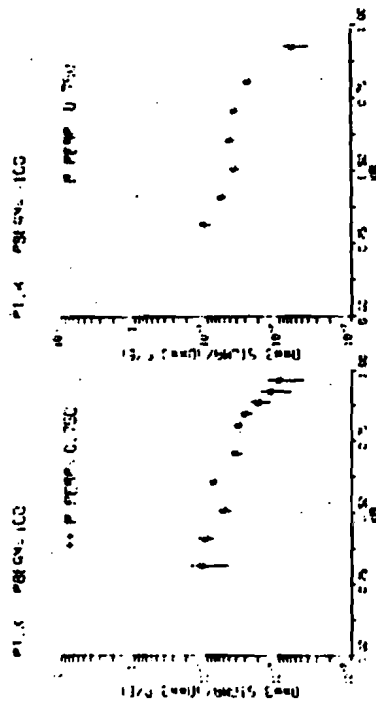


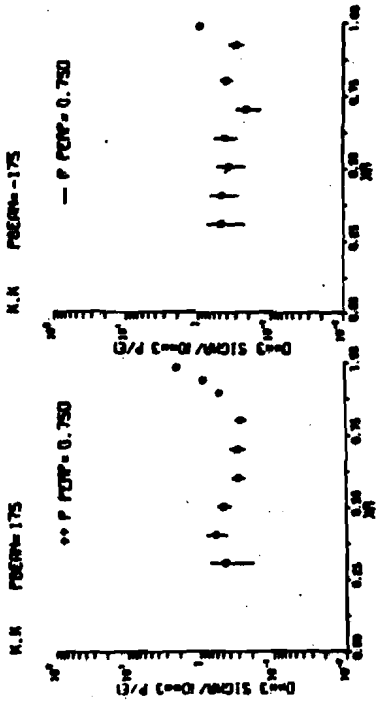
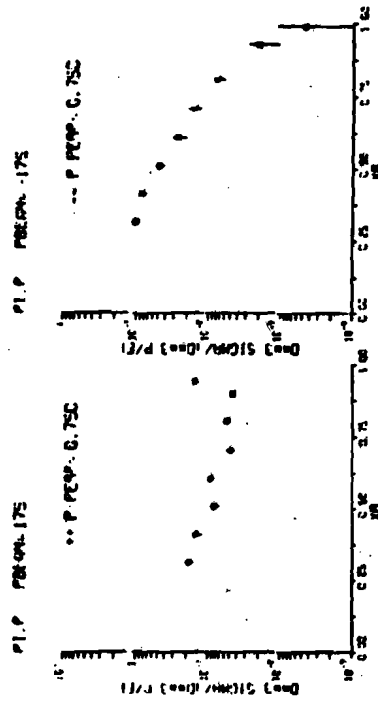
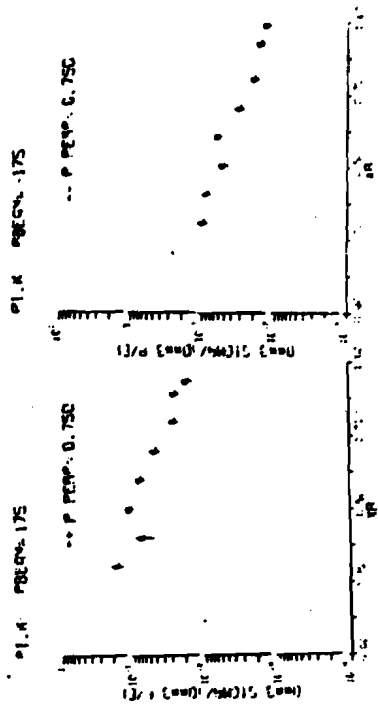
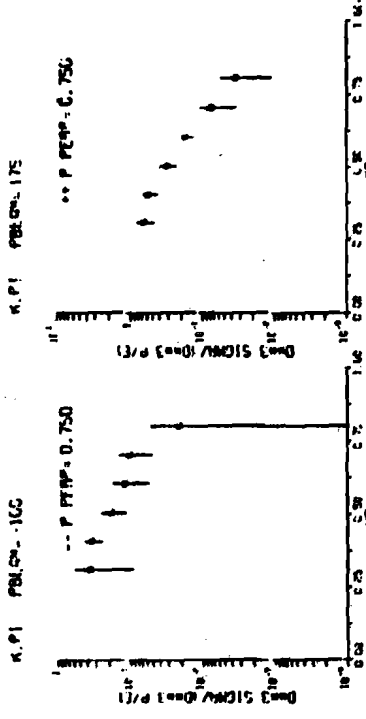


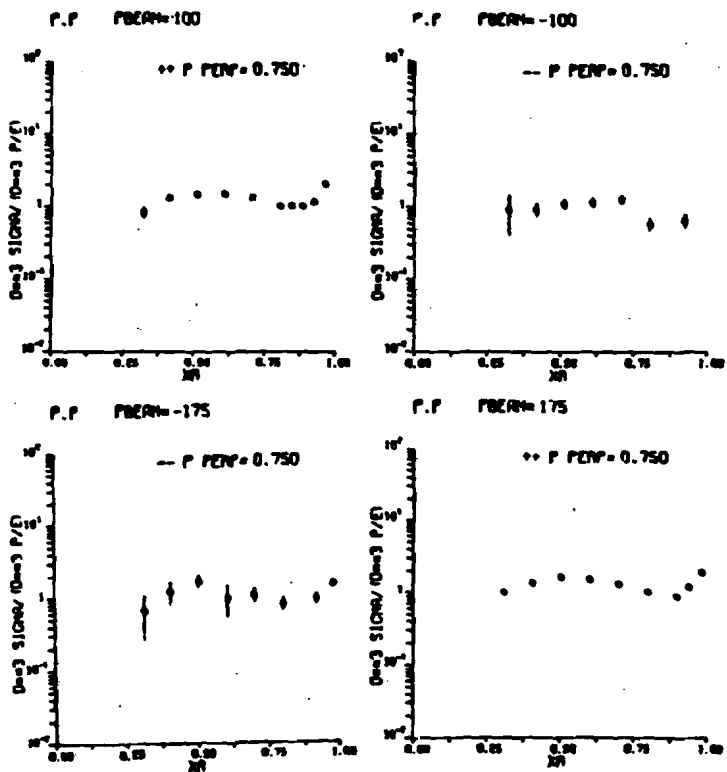












APPENDIX III

Radiative Corrections for $a + b + c + X$

The formula used for the radiative corrections was

$$\left. \frac{d\sigma}{d\Omega dE'}(E_0, E', \theta) \right|_{\text{TRUE}} = C \left[\left. \frac{d^2\sigma}{d\Omega dE'} \right|_{\text{MEASURED}} - I_1^A - I_1^B - I_2^A - I_2^B \right]$$

$$I_1^A = \left[1 + 1.16 v_c \right] \left[\ln \frac{E_0}{E'} \right]^{v_c} \left[\ln \frac{E_0}{E'} \right]^{v_c} \frac{v_c S_A}{E_{of} - E'} \left. \frac{d\sigma}{d\Omega}(E_0, \theta) \right|_{\text{ELAST.}}$$

$$I_1^B = \left[1 + 1.16 v_c \right] \left[\ln \frac{E_{of}}{E'} \right]^{v_c} \left[\ln \frac{E_0}{E_0} \right]^{v_c} \frac{v_c S_B}{E_0 - E_0'} \left. \frac{d\sigma}{d\Omega}(E_0', \theta) \right|_{\text{ELAST.}}$$

are the elastic scattering contributions, where

$$E_{of} = \frac{E_0}{1 + \frac{2E_0}{m_b} \sin^2 \theta/2}$$

$$E_0' = \frac{E'}{1 - \frac{2E'}{m_b} \sin^2 \theta/2}$$

$$E_e = \frac{E_o + E_o'}{2}$$

$$E_e' = \frac{E_e}{1 + \frac{2E_e}{m_b} \sin^2 \theta/2}$$

and $v_c = \frac{\alpha}{\pi} \frac{2m_a^2 - t'}{Q'} \ln \frac{Q' - t'}{Q' + t'}$ is the equivalent virtual radiator length, where

$$Q' = (t'^2 - 4m_a^2 t')^{1/2}, \quad t' = 2m_a^2 - 2E_a E_c + 2p_a p_c \cos \theta < 0$$

The S_A and S_B are given by

$$S_A = \frac{E'}{E_{of}} + \frac{1}{2} \left[\frac{(E_{of} - E')}{E_{of}} \right]^2$$

$$S_B = \frac{E_o'}{E} + \frac{1}{2} \left[\frac{(E_o - E_o')}{E_o} \right]^2$$

These functions give the approximate spectral distribution of the emitted photons.

The contributions from inelastic scattering are

$$C = [1 - 0.83(v_A + v_B)] e^{S_A}$$

$$I_2^A = [1 + 0.7(v_A + v_B)] \left(\frac{\Delta'}{E'} \right)^{v_B}$$

$$\times \int_{E_o'_{min}}^{E_o - \Delta E_o} dE_o' \left[\frac{\ln(E_o/E_o')}{E_o - E_o'} \right]^{v_B} v_B S_B \frac{d^2\sigma}{d\Omega dE'}(E_o', E_o', \theta) \Big|_{TRUE}$$

$$I_2^B = [1 + 0.7(v_A + v_B)] \left(\frac{\Delta}{E_o} \right)^{v_B}$$

$$\times \int_{E'+\Delta E'}^{E_{MAX}} dE_{of} \left[\frac{\ln(E_{of}/E')}{E_{of} - E'} \right]^{v_A} v_A S_A \frac{d^2\sigma}{d\Omega dE_{of}}(E_o, E_{of}, \theta) \Big|_{TRUE}$$

where $v_A = v_B = \frac{\alpha}{\pi} \left[\frac{2m_a m_c - t}{Q} \ln \left(\frac{Q-t}{Q+t} \right) \right]$

$$Q = (t^2 - 4m_a m_c t)^{1/2}$$

$$t = m_a^2 + m_c^2 - 2E_a E_c + 2p_a p_c \cos \theta$$

$$S_R = v_A \left[\ln \frac{E_0}{\Delta E'} + \ln \frac{E'}{\Delta E'} \right]$$

$$\Delta = \frac{1}{2} \left[E_0 - \frac{E'}{1 - \frac{2E'}{m_b} \sin^2 \theta/2} \right]$$

$$\Delta' = \frac{1}{2} \left[\frac{E_0}{1 + \frac{2E_0}{m_b} \sin^2 \theta/2} - E' \right]$$

and $\Delta E_0 = \Delta E' = 1/2$ of the energy acceptance of our spectrometer
 $E_{0 \min}$ is the minimum incident energy kinematically permitted
 to cause a particle c to be detected at energy E' .
 E'_{\max} is similarly the maximum energy permitted kinematically
 for a particle c produced by a scattering of particle
 a at energy E_0 . The spectral functions S_A and S_B are
 defined exactly as in the elastic case, but now involve
 the integration variables.

APPENDIX IV. Spectrometer First Order TRANSPORT Coefficients

This appendix contains a listing of all the magnetic elements in the spectrometer and their settings for normal data taking. Also included are the first order TRANSPORT matrix elements described in Chapter II. The matrix labeled "TRANSFORM 1" corresponds to the matrix R_1 described in Chapter II, and the matrix labeled "TRANSFORM 2" corresponds to the matrix R_2 . The numbers in the fifth rows and columns in these matrices describe the beam bunch length and are not relevant to our analysis.

- 125, 1972, unpublished;
L.J. Levinson et al., Bull. Am. Phys. Soc. 20, 593 (1975).
14. D.S. Ayres et al., Phys. Rev. D15, 3105 (1977).
 15. J.I. Friedman, private communication.
 16. F.E. Taylor et al., Phys. Rev. D14, 1217 (1976).
 17. D. Cutts et al., Phys. Rev. Lett. 40, 141 (1978).
 18. R.P. Feynman, Phys. Rev. Lett. 23, 1415 (1969).
 19. J. Banacke et al., Phys. Rev. 188, 2159 (1969).
 20. B. Andersson, G. Gustafson, and C. Peterson, presented at the Bielefeld Meeting, 5-8 September, 1977, University of Lund, Sweden, preprint LU TP77-19;
B. Andersson, G. Gustafson, and C. Peterson, Physics Letters 59B, 221 (1977);
B. Andersson, G. Gustafson and C. Peterson, University of Lund, Sweden, preprint LU TP 77-13.
 21. K.P. Das and R. Hwa, Physics Letters 58B, 459 (1977).
 22. J. Whitmore et al., Phys. Rev. D16, 3137 (1977).
 23. B. Andersson, private communication.
 24. M. Holder et al., Physics Letters 59B, 377 (1977);
R. Oderico, CERN TH-2360.
 25. X. Huang, private communication.
 26. H. Miettinen, as cited by Duke and Taylor in reference 27.
 27. D.W. Duke and F.E. Taylor, FERMILAB-PUB-77/95-TNY
 28. W. Heing, S.B. thesis, Massachusetts Institute of Technology, (1976), unpublished.

29. G.R. Farrar, Nucl. Phys. B77, 429 (1974).
30. S.J. Brodsky and J.F. Gunion, SLAC-PUB-1839 (1977).
31. R. Blankenbecler and S.J. Brodsky, Phys. Rev. D10, 2973 (1974);
J.F. Gunion, Phys. Rev. D10, 242 (1974);
G.R. Farrar, Nucl. Phys. B77, 429 (1974).

ACKNOWLEDGEMENTS

Many people have contributed to the successful execution and analysis of this experiment. I would like to thank all members of the E118 collaboration and their technical staffs for their part in this endeavor.

I would like to thank the Fermilab people who have made running the experiment an easier task to bear. Drs. Peter Garbincius and John Elias provided much of the on-site guidance for the early stages of the experiment. I would also like to thank the Meson Laboratory staff for all their help. I appreciate Travis Minto's technical support.

Professor R.E. Lanou of Brown University shared many shifts with me. I would like to thank him for his valuable insights and interesting discussions. I would like to thank Tom Lyons of MIT for always being there to solve any problem whatsoever and for his splendid target assembly.

I would like to express my appreciation to my fellow graduate students, W. Aitkenhead and L. Votta, for sharing the labors in this experiment. I want especially to thank W. Aitkenhead for his work during the setup of the experiment and for his share of the cross section analysis.

The contributions of Professors Don Barton and George Brandenburg were of great help. Drs. Bruce Nelson and Robin Verdier helped me to understand the online computer system. I am particularly indebted to Dr. Verdier for his help and

and guidance through much of the analysis work. I would also like to thank Ms. Deena Dubin for her splendid effort in writing all of the plotting programs and several analysis routines and for her help with many crossword puzzles. I am grateful to Roger Strong for his technical assistance. Professors Henry Kendall and Lawrence Rosenson provided valuable help throughout all phases of the experiment.

I am especially grateful to my thesis advisor, Professor Jerome Friedman who provided me with help and encouragement throughout my graduate career.

Financial support from the MIT Physics Department and from the Laboratory for Nuclear Science made this endeavor possible.

I would also like to thank Ms. Sally Anand for her typing of this thesis.

BIOGRAPHICAL NOTE

The author [REDACTED]

[REDACTED]
[REDACTED]
[REDACTED] He entered M.I.T. in September, 1967, and was admitted to the graduate school in the Electrical Engineering Department in September, 1971. In February, 1973 he was awarded an Electrical Engineer's degree, an S.M. degree in Electrical Engineering and S.B. degrees in Physics, Mathematics and Electrical Engineering. He was admitted to the graduate school in the Physics Department in February, 1973 and has been associated with the Kendall - Friedman - Rosenson group since 1974.